**Measurement and Control of Exciton Spin In Organic Light Emitting Devices**

by

Michael Segal

Submitted to the Department of Electrical Engineering and Computer Science

in partial fulfillment of the requirements for the degree of

Doctor of Philosophy

at the

MASSACHUSETTS INSTITUTE OF TECHNOLOGY

September 2007



Author.....
Department of Electrical Engineering and Computer Science
September 1, 2007

Certified by.....
Marc A. Baldo
Associate Professor
Thesis Supervisor

Accepted by.....
Arthur C. Smith
Chairman, Department Committee on Graduate Students

**Table of Contents**

**Measurement and Control of Exciton Spin In Organic Light Emitting Devices**

by Michael Segal

Submitted to the Department of Electrical Engineering and Computer Science
on August 31, 2007
in partial fulfillment of the requirements for the degree of
Doctor of Philosophy

## Abstract

Organic semiconductors are a promising new material set for electronic and optoelectronic devices. Their properties can be precisely controlled through chemistry, and they are well-suited for large-area, flexible, and low-cost devices. Optical emission and absorption in these materials is mediated by strongly-bound electron-hole pairs called "excitons". While the function of many organic electronic devices depends on excitons, exciton formation is incompletely understood.

This thesis presents a general rate model for exciton formation, and studies formation through three different experimental approaches, in the context of the rate model. First, a novel method for measuring exciton spin statistics is described and implemented. This method avoids several drawbacks common to existing methods, and shows completely randomized exciton spin statistics in two archetypal organic semiconductors: one that is a small molecule, and another that is a polymer. Second, optically-detected magnetic resonance effects in organic semiconductors are shown to be unrelated to exciton formation processes, contrary to the current understanding. A quenching-based model is developed and shown to completely describe the data.

Both of these experimental results suggest an absence of spin mixing of exciton precursor states. In the third section of this thesis, this lack of mixing is confirmed both experimentally and through calculation. It is then "turned on" through the introduction of spin-orbit coupling. An approximately three-fold increase in the fluorescent efficiency of an organic light emitting device results.

Thesis Supervisor: Marc Baldo
Title: Esther and Harold E. Edgerton Associate Professor of Electrical Engineering

## Acknowledgements

First thanks to my supervisor, Marc Baldo, for his enthusiasm and leadership, and for serving as an example of how to choose scientific work and get it finished. Other faculty have also contributed much to this work: Zoltan Soos and Steven Forrest at Princeton, Joseph Shinar at Iowa State, and Troy Van Voorhis at MIT are all co-authors on publications. Vladimir Bulovic served on my RQE and thesis committees, and always had an enthusiastic hello ready for me. His lab and his students hosted me for the months before we had our own equipment. Thanks especially to Seth Coe and Conor Madigan, who built their own setup and taught me how to use it. Finally, Professor Fred Trofimenkoff at the University of Calgary, for taking me under his wing and helping me get to MIT.

To my student collaborators: here's to many an hour in the lab, scratching our heads. Madhusudan Singh and Kelley Rivoire and the countless OLED variations; Moon Ky Lee and the nights in a dark lab with a big magnet among the Iowa cornfields; Rupa Das, Patrick Kiley and a collection of proteins, packaged and tortured but alive; Kaveh Milaninia for teaching me most everything about how to work in a fab; Jiye Lee and our collection of frequency responses; Carlijn Mulder and X-OLEDs; and Evgueni Nesterov who helped me make pretty liquid crystal switches. Thank you also to my group, for doing everything that a group does, and without which this thesis would have been impossible: Mihai Bora, Kemal Celebi, Mike Currie, Shlomy Goffri, Tim Heidel, Priya Jadhav, Rajay Kumar, Benjie Limketkai, Jon Mapel, and Luke Theogarajan.

# Chapter 1. Introduction

## 1.1 Organic Semiconductors

This thesis is concerned with organic light emitting devices, which represent one of the most mature and commercially successful applications of organic semiconductors. Organic semiconductors are carbon-based molecular solids held together by weak van der Waals intermolecular forces. About 90% of all known compounds[1] are organic, spanning a large range of complexities (Fig. 1.1), from tens of atoms per molecule (referred to as "small molecule" organic semiconductors), to molecules thousands of times heavier, consisting of repeating units ("polymers"), to biological molecules whose structure encodes information and includes mechanical and electrical machinery (such as the photosynthetic reaction center complex).

The arguments for the use of organic semiconductors in electronics are:

(1) The properties of an organic solid are determined by the properties of the molecules composing it, and intramolecular forces. The strength of the bonds between molecules ($< 10^{-2}$ eV) is several orders of magnitude less than that of covalent intermolecular bonds such as those found in silicon. As a result, the properties of organic films are set primarily by the properties of the individual molecules of which they are composed. This is in contrast to inorganic semiconductors in which electronic states are delocalized over many atoms and therefore sensitive to large-scale structure.

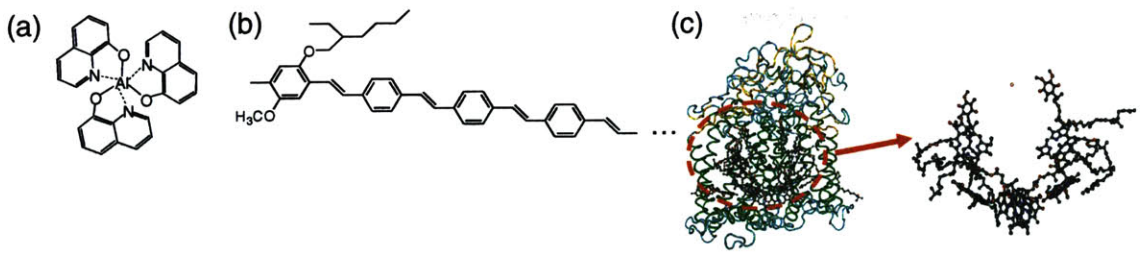


Fig. 1.1– Three examples of organic semiconductors. (a) tris(8-hydroxyquinoline) aluminum $Alq_3$, a 'small molecular' organic semiconductor, (b) poly[2-methoxy-5-(2-ethylhexyloxy)-1,4-phenylenevinylene] (MEH-PPV), a polymeric organic semiconductor and (c) a photosynthetic reaction center (right) is held inside a protein matrix (left) to Angstrom precision.

As a result, optical and electrical properties of organic semiconductors can be designed with great precision through chemistry. Examples include:

- tuning the emission wavelength of a family of cyclometalated iridium complexes across the entire visible spectrum by varying the metal atom ligand conjugation length.[2]

- tuning the spin-mixing strength of a phosphor by replacing or removing its central metal atom.[3]

- tuning radiative efficiencies by altering steric bulk through the use of sidegroups.[4]

- tuning conductivity by electrochemical doping.[5]

Inorganic semiconductor crystals admit relatively few design methods by comparison, and these methods (such as doping and strain) often involve significant processing steps.

(2) Because the properties of an organic solid are set by its component molecules, it is relatively insensitive to the way it is put together. This greatly relaxes constraints on

fabrication procedures and device geometries relative to inorganic semiconductor devices. Fabrications techniques are various and generally low-cost, including thermal evaporation, vapor phase deposition, roll-to-roll contact printing, solution-based ink jet printing, and imprint lithography. Due to their insensitivity to variations in large-scale structure, and amenability to low-temperature processing, amorphous organic thin films are well-suited for flexible substrates. They are also well-suited for large-area devices which are prohibitively expensive for crystalline inorganic semiconductors. (This benefit of little long-range structure is, however, also being developed through various means for other material sets. For example, amorphous silicon devices have been grown on flexible substrates, as have devices that place rigid inorganic devices in a flexible matrix.) Finally, organic devices which involve a junction between dissimilar materials are unaffected by lattice matching issues which can be very important for analogous inorganic devices.

(3) Organic semiconductors are especially well suited for certain applications. Their first commercial application was in photocopiers and laser printers, for which they are suited due to their high resistivity and optical absorption strength. They are being investigated for use in chemical sensors because they bond weakly to analytes, allowing for multiple use, can have strongly non-linear reactions to analytes, allowing for gain, and can be designed to have high specificity through structural design. They are also efficient emitters, which has led to their use in the light emitting devices which are the subject of this thesis. Certain organic molecules exhibit multiple stable conformations, which may be used to store information or act as a switch. Also, because excited states in organic semiconductors are highly localized, there are

large energy barriers to spin decoherence and decoherence times are long compared to inorganic semiconductors.[6]

These advantages come with significant challenges:

(1) The weak intramolecular bonding which can be used to advantage, also greatly reduces carrier mobilities relative to crystalline semiconductors. Mobilities are generally less than 10 $cm^2$ / Vs at room temperature[7] compared to $10^3$ $cm^2$ / Vs for GaAs. As a result, organic semiconductors are incorporated into devices as very thin films, across which large electric fields can be created using low voltages. In addition, the amorphous nature of these thin films leads to a large energetic disorder and high charge trap densities. The presence of disorder and traps makes the development of future applications, such as spintronics and quantum computing, more challenging.

(2) Organic semiconductors are prone to degradation. They are readily oxidized or reduced to form different chemical species, most commonly with atmospheric oxygen and moisture. This effect is exacerbated by high space charge populations. Even with perfect encapsulation, however, 'intrinsic' degradation effects can lead to short device lifetimes.[8] Furthermore, weak intramolecular bonding can cause significant structural changes over time, often activated by the presence of charge or simply by Joule heating. Amorphous layers may polymerize or crystallize. Finally, thermal evaporation of metal contacts onto soft organic layers can damage those layers.

Applications of organic semiconductors include transistors, photovoltaics, and light-emitting devices, which will be considered separately in the next section. For each application, the use of an organic semiconductor active element brings the potential for low-cost fabrication, and flexible large-area substrates. Competing technologies often use amorphous or polycrystalline inorganic semiconductors, which can be used for large-area applications, but usually require high-temperature processing, and substrates that are rigid at room temperature. Recently, though, flexible Si-based electronics have been demonstrated.[9]

Figures 1.2 and 1.3 show two archetypal organic semiconductor devices. Figure 1.2 shows the current-voltage characteristic of an all-polymer transistor, printed entirely with an inkjet printer, including interconnections. This kind of device has the potential to produce low-cost and relatively low-speed switches, useful for identification tags or display backplanes. Figure 1.3 shows the structure of an organic photovoltaic that converts sunlight to electricity at a power conversion efficiency of 2.5%.

## 1.2 Organic LEDs

Organic light emitting devices (OLEDs) are the application of organic semiconductors closest to being a mature technology. OLEDs compete in two broad technology categories: information display, and white lighting (ie, information-less display). In the category of white lighting, OLEDs compete with incandescent bulbs, fluorescent lights, and inorganic LEDs (ILEDs). Incandescents are inefficient, at about a 5% power efficiency, or 15 lm / W. Furthermore, they are in the process of being banned in the EU and certain states. OLEDs will be one of a variety of technologies competing to replace incandescents.

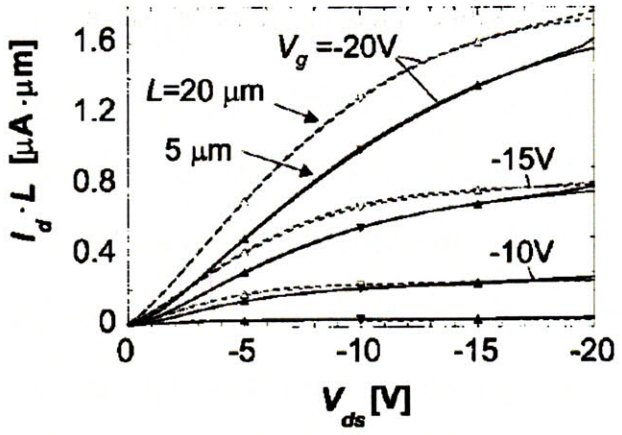


Fig. 1.2 – Characteristics of an inkjet-printed all-polymer transistor, from Ref. [10]. The vertical axis is current multiplied by channel length. Droplets fall onto a surface patterned with hydrophobic strips, allowing channel lengths of 5 μm. Mobilities of 0.02 $cm^2$ / V-s and on-off ratios of $10^5$ were measured.

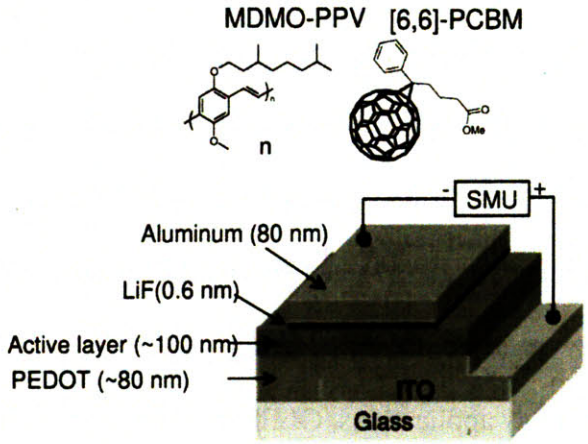


Fig. 1.3 – An organic photovoltaic cell achieving a power conversion efficiency of 2.5% under an illumination of AM1.5. The active layer consists of a blend of the two polymers shown. It is found that the morphology of the blend has a dramatic impact on the cell efficiency.[11] Morphology was also found to be critical in other cells, for example, in CuPC:PTCBI blends.[12]

The energy impact resulting from a complete replacement of incandescent bulbs would be significant. In 2001, 22% of the US electricity budget, and 8% of the total energy budget, went to white lighting at an annual cost of $50 billion and 130 millions tons of $CO_2$, representing 7% of all US carbon emissions. The portion of this expenditure represented by incandescents is modest – about 10% - but the replacement of all incandescents by, for example, OLEDs would represent at least a 1% savings of the US electricity budget, given the recent demonstration of a 65 lm / W white OLED. The turnover in the lumen market is also high, at about 33% / year,[13] making the market amenable to new technologies. Table 1.1 breaks down white light usage by the Color Rendering Index, or CRI, which is a measure of the quality of the light. An incandescent's CRI is 100, the maximum value possible.

Residential lighting tends to be higher CRI. Consumer resistance to low-CRI fluorescents may make OLEDs competitive due to their potentially high CRI. In addition to high efficiencies and high CRI, OLEDs are amenable to large-area formats, which ILEDs and fluorescents can serve, but generally only through arraying under an optically dispersive element. The outstanding issue for white light applications is lifetime. To the author's knowledge, the sole white light OLED product on the market has a half-life of 10,000 hours and an area approximately the size of a cell phone display.

For information display applications, OLEDs compete primarily with LCDs. Since OLEDs do not require a backlight, they can in principle be more power efficient, though LCDs are backlit by very efficient fluorescent tubes or ILEDs. Also, since they are a thin film technology, they are more appropriate for portable devices. The potential for flexible substrates opens the possibility of applications like roll-up electronic newspapers that are difficult for LCDs. OLEDs are also Lambertian emitters. Since the light emission occurs from

| | Residential | Commercial | Industrial | Other |
|---|---|---|---|---|
| Low CRI | 9 | 3097 | 2016 | 2119 |
| Medium CRI | 1095 | 13508 | 3833 | 59 |
| High CRI | 51 | 421 | 70 | 66 |
| Very High CRI | 1875 | 913 | 27 | 81 |
| Total | 3030 | 17939 | 5946 | 2325 |

Table 1.1 – Lumen-hour output by Sector and CRI for the year 2000 (Teralumen-hours/ year).[13]

a collection of randomly oriented dipoles, it is perfectly scattered and can be seen from any viewing angle. This

is in contrast to LCD displays, which suffer from image degradation at large angles. Finally, OLEDs are potentially cheap to manufacture. Low-temperature processing and a tolerance for defects drive manufacturing prices lower. However, other manufacturing challenges, such as the difficulty of constructing a current-driving transistor backplane array, compensating for color-dependent degradation, encapsulation, and low yield have meant OLEDs do not yet compete on cost with standard displays, but rather are a premium product. Table 1.2 compares the performance of these two technologies.

Some examples of the current state of OLED technology are shown in Fig. 1.4(a). While applications are restricted to low lifetimes and areas, the 2005 market size was nevertheless a substantial $620 million, representing a volume growth of 65% over 2004 (DisplayBank). Figure 1.4(b) shows some potential future OLED products which, if

| | Organic low molecular | Organic High Molecular | LCD CGS | LCD Low-Temp polysilicon | LCD Amorphous | LCD LCD STN | LCD LCD FS |
|---|---|---|---|---|---|---|---|
| brightness | Good 100 | Good 120 | Very Good 150 | Very Good 150 | Very Good 150 | Good 100 | Very Good 150 |
| contrast | Very Good 500:1 | Very Good 500:1 | Good 300:1 | Good 300:1 | Good 300:1 | Average 30:1 | Good 150:1 |
| high-definition | Good QVGA | Average QCIF | Very Good VGA | Very Good VGA | Average QCIF | Poor | Very Good QCIF |
| ppi | 180 | 130 | 200-300 | 200-300 | 200 | 180 | 150 |
| Color Reproducibility (%) | Good 60-70 | Uncertain | Average 30-40 | Average 30-40 | Average 30-40 | Poor 20-30 | Very Good 90-100 |
| Response Speed (ms) | Very Good 0.01 | Very Good 0.01 | Good 20-25 | Good 20-25 | Good 20-25 | Poor 100-200 | Good 135 |
| Thickness (mm) | Very Good 1.5-2.0 | Very Good 1.5-2.0 | Good 3.0-3.5 | Good 3.0-3.5 | Good 4.0-5.0 | Poor 3.5-5.0 | Good 3.0-4.0 |
| Power Consumption (mW) | Average (270) | Very Good 150 | Average 250 | Average 250 | Good 180 | Good 180 | Good 180 |
| Life (hr) | Average 8000 | Poor 1000 | Very Good 50,000 | Very Good 50,000 | Very Good 50,000 | Very Good 50,000 | Very Good 50,000 |

Table 1.2 – Comparison of OLED and LCD specifications for 2" displays. OLEDs have superior contrast, color reproduction, thickness, and response time, but low lifetimes. Source: Mizuno Securities Equity Research.

successful, will represent a substantial expansion of both the number of markets addressed by OLEDs, and the penetration of each market.

Larger-area information display products will require novel patterning techniques. This is because the metallic shadow masks used for small displays do not scale well to sizes beyond 15". Patterning technologies appropriate for inorganic semiconductor devices involve photoresists, strippers, and baking steps that are generally incompatible with relatively fragile

(a)

(b)

Fig. 1.4 - (a) Some past and present OLED products, from left to right: car audio, MP3 players, cell phones and cell phone backlights. The current OLED ~$2b / yr OLED market is composed entirely of low-lifetime small-area displays, mostly in portable electronics in which power consumption, weight and bulk are important (credit: Creative, BenQ, Konica, Pioneer). (b) Potential OLED products, from left to right: flat screen television, large-area white lighting, and rollable display.

organic semiconductors. Techniques being pursued include inkjet printing and laser induced thermal imaging.

Another outstanding issue is lifetime. As described in Table 2.2, the lifetime of a blue-emitting phosphor at a brightness comparable to that of a modern LCD TV is in the thousands of hours, far below commercial feasibility. Lifetime and efficiency are closely related, since lifetime scales as a negative power of the brightness, $B^{-\alpha}$, where $\alpha$ is typically 1.5 – 2.[14] Another way of saying that OLEDs have low lifetimes, then, is to say that they have low brightness. This in general means that an OLED white lighting application, for example, will

be dim, and therefore require a large area to produce the required amount of light. Techniques being pursued to address the lifetime issue include the synthesis of new materials, as well as encapsulation, by glass, metal, atomic layer deposition,[15] and polymers.[16] Clearly a direct path to longer lifetimes is efficiency improvement. The two most dramatic improvements in OLED efficiency have resulted from the advent of the heterostructure OLED, and of metal-containing phosphors (section 2.8). This thesis presents an alternative to the use of phosphors, potentially helping address the lifetime (efficiency) problem. The efficiency improvement described in this thesis results from the fact that, despite being a relatively mature technology with considerable market penetration, basic aspects of OLED function remain poorly understood and uncontrolled. This thesis focuses on one such aspect of OLED function: exciton spin.

# Chapter 2. OLED Physics

Maximizing $\eta_{EQE}^{I}$ requires understanding how excitons are formed, and in particular, how exciton spin is important. This chapter describes how the charges in an organic semiconductor are spatially localized and have quantized energy levels; how in an OLED they come together to form excitons and other bound states; the energetics of these states; the importance of the spin of these states to OLED efficiency; and how this spin can change.

## 2.1 Charge Localization

Unlike in crystalline semiconductors, charge in organic semiconductors is localized on single molecules, or on single polymer strands in the case of polymeric materials. To see this, consider the probability $P$ that a charge on one molecule is able to move to another molecule a distance $r$ or less away[17]:

$$P(r) \propto \frac{\beta(r)N(r)}{W}, \tag{2.1}$$

where $\beta$ is the interaction strength between the two molecules, $N \propto r^3$ is the number of molecules to which the charge can move, and $W$ is the energy width of the density of states of the molecules in the film. $P$ is inversely proportional to $W$ because only energy-conserving transport is considered. P.W. Anderson showed[18] that $P$ is small, and charges are localized, if two conditions are met: first, that $\beta$ falls with $r$ faster than $N$ grows with $r$, which is true in general for molecular interactions, for which $\beta \propto \exp(-\alpha r)$; and second, that the average value of $\beta$ is small compared to a parameter of order $W$. In other words, as the variation in the

energies of the molecules increases, the transport probability decreases, and localization increases. This type of disorder is termed *diagonal disorder*. In addition, *off-diagonal* disorder, or randomness in $\beta(r_{ij})$ for two molecules *i* and *j*, can also lead to localization. Both types of disorder are found in organic semiconductors.[17]

When we consider conduction through organic semiconductors, then, instead of thinking of a single free-space charge, or of a delocalized electron wave, we think about charges localized on molecules. These charges attract opposite charges, causing a polarization cloud, and are called polarons. Positive and negative polarons are called electrons and holes in this thesis. These are markedly different than the electrons and holes in inorganic semiconductors.

## 2.2 Electronic Energy Levels

To describe excitons, we first need the idea of molecular orbitals as a good representation of the electronic state of an entire molecule. A simple representation for the electronic state of a molecule is key to this thesis. In principle the exact calculation of the electronic energy levels of a molecule with *i* electrons with locations $\{\mathbf{r}_i\}=\{x_i\mathbf{i}+y_i\mathbf{j}+z_i\mathbf{k}\}$ and *I* nuclei with locations $\{\mathbf{R}_i\}=\{X_i\mathbf{i}+Y_i\mathbf{j}+Z_i\mathbf{k}\}$ would require a solution of the time-independent Schrödinger equation for the wavefunction $\Psi^n$,

$$H\Psi^n(\{\mathbf{r}_i\},\{\mathbf{R}_i\})=E^n\Psi^n(\{\mathbf{r}_i\},\{\mathbf{R}_i\}), \tag{2.2}$$

where the total Hamiltonian is[19,20]

$$H=\left[-\frac{\hbar^2}{2m_e}\sum_i\left(\frac{\partial^2}{\partial x_i^2}+\frac{\partial^2}{\partial y_i^2}+\frac{\partial^2}{\partial z_i^2}\right)-\frac{\hbar^2}{2}\sum_I\frac{1}{M_I}\left(\frac{\partial^2}{\partial X_I^2}+\frac{\partial^2}{\partial Y_I^2}+\frac{\partial^2}{\partial Z_I^2}\right)+\left(\sum_{i,j}^{i>j}\frac{1}{r_{ij}}-\sum_{i,I}\frac{Z_I}{r_{iI}}+\sum_{I,J}^{I>J}\frac{Z_IZ_J}{r_{IJ}}\right)\right] \tag{2.3}$$

Here $M_I$ is the mass of nucleus $I$, $r_{ij}$ is the distance between electrons $i$ and $j$, and $r_{iI}$ is the distance between electron $i$ and nucleus $I$. An exact solution to equations (2.2) and (2.3) for an organic molecule with tens of atoms is an intractable problem.

The problem becomes simpler if the total wavefunction $\Psi^n$ is split into an electronic component $\varphi$ which depends on both electronic and nuclear positions, and a nuclear component $\chi$ which is independent of electronic position, so that $\Psi^n = \chi(\{R_i\})\varphi(\{r_i\},\{R_i\})$. This is known as the Born-Oppenheimer approximation and is justified by the large difference in electronic and nuclear mass, so that electrons respond almost instantly to changes in nuclear coordinates and effectively see a static nuclear potential.[19] Written in one dimension for clarity, the full Schrödinger equation using the Hamiltonian of Eq. (2.3) becomes

$$H\varphi\chi = -\frac{\hbar^2}{2m_e}\sum_i \frac{d^2\varphi}{dx_i^2}\chi + \left(\sum_{i,j}^{i>j}\frac{1}{r_{ij}} - \sum_{i,I}\frac{Z_I}{r_{iI}} + \sum_{I,J}^{I>J}\frac{Z_I Z_J}{r_{IJ}}\right)\varphi\chi \qquad (2.4)$$

under the Born-Oppenheimer approximation, where the nuclear masses $M_I$ are taken to be much larger than the electronic masses $m_e$, so that the $\frac{1}{M_I}\frac{\partial^2}{\partial X_I^2}$ term is dropped. The nuclear wavefunction $\chi$ then cancels out, and the electronic wavefunction satisfies[17,19]

$$H\varphi = E_e\varphi = -\frac{\hbar^2}{2m_e}\sum_i \frac{d^2\varphi}{dx_i^2} + \left(\sum_{i,j}^{i>j}\frac{1}{r_{ij}} - \sum_{i,I}\frac{Z_I}{r_{iI}} + \sum_{I,J}^{I>J}\frac{Z_I Z_J}{r_{IJ}}\right)\varphi. \qquad (2.5)$$

Similarly, the nuclear wavefunction satisfies

$$H\chi = -\frac{\hbar^2}{2}\sum_I \frac{1}{M_I}\frac{d^2\chi}{dX_I^2} + E_e\chi. \qquad (2.6)$$

The electronic ground state of a molecule can therefore be calculated by solving for the optimal nuclear configuration using classical rules of valency, solving for $E_e$, and then

searching for the minimum $E_e$ that obtains through small deviations in nuclear coordinates. The nuclear configuration of a molecule becomes a *parameter* of the electronic Hamiltonian.[19]

The problem of solving for the electronic wavefunctions of many-electron molecules remains intractable, however, even under the Born-Oppenheimer approximation. An additional approximation is required before these can be solved for: the "independent-electron approximation".[20,21] Under this approximation, electron-electron interaction terms in the electron Hamiltonian are dropped, causing the energy of each electron to be independent of the energy of every other electron:

$$H^{(0)}\varphi^{(0)} = E_e^{(0)}\varphi^{(0)} = -\frac{\hbar^2}{2m_e}\sum_i \frac{d^2\varphi^{(0)}}{dx_i^2} + \left(\sum_{i,I}\frac{Z_I}{r_{iI}} + \sum_{I,J}^{I>J}\frac{Z_I Z_J}{r_{IJ}}\right)\varphi^{(0)} = \sum_{i=1}^{N} H_{e,i}^{(0)}\varphi^{(0)}. \quad (2.7)$$

Since the independent-electron wavefunction, $\varphi^{(0)}$, is independent of the summation index, the electronic Hamiltonian can be considered as a sum of independent electron Hamiltonians $H_{e,i}^{(0)}$. Therefore the electronic wavefunction becomes a product of one-electron wavefunctions called "molecular orbitals":

$$\varphi^{(0)} = \prod_{i=1}^{N}\varphi_i^{(0)}. \quad (2.8)$$

It is under this approximation that this thesis will define molecular orbitals in organic semiconductors. The electronic energy levels of a molecule will thus be a set of one-electron or molecular orbital energy levels. The independent electron approximation allows the lowest energy state of a molecule to be simply constructed, by placing electrons into the lowest available energy orbitals until all of the electrons are accounted for. All molecules that will be considered here have an even number of electrons $N$, occupying the lowest-energy $N/2$

orbitals. Note that a restricted form of electron-electron interactions will be re-introduced in this thesis, in the form of spin-dependent perturbations to orbital energies. These interactions will take into account only the two "frontier" or outermost electrons in the molecule.

## 2.3 Excitons

Fig. 2.1 shows the ground state and first excited state electronic configurations of a molecule.[19] An 'exciton' is any excited molecular electronic state. We usually focus on the lowest-energy exciton, which results when one electron occupies the highest occupied molecular orbital (HOMO) and another the lowest unoccupied molecular orbital (LUMO). We also focus on "Frenkel" excitons, or excitons localized on one molecule, as opposed to "Wannier" excitons, which are delocalized over many molecules or atoms, and are encountered in inorganic materials. An exciton can be created optically, in which case absorption of a photon promotes an electron from the HOMO to the LUMO, or electrically, in which case charges injected from distant contacts drift onto the same molecule. The resulting excited state is the same, with the possible exception of its spin state, as explained below. In each case the HOMO loses negative charge, or equivalently, it gains positive charge. This positive charge in the HOMO is referred to as a hole. The electron in the LUMO experiences a Coulombic attraction to the hole of strength sufficient to bind the two charges together. Organic semiconductors distinguish themselves from inorganic semiconductors by the strength of this binding – typically on the order of 1 eV. The strength of this binding allows us to consider the electron and hole as a 'quasi-particle', whose properties are preserved as it diffuses through the material and interacts with other particles and quasi-particles. The large

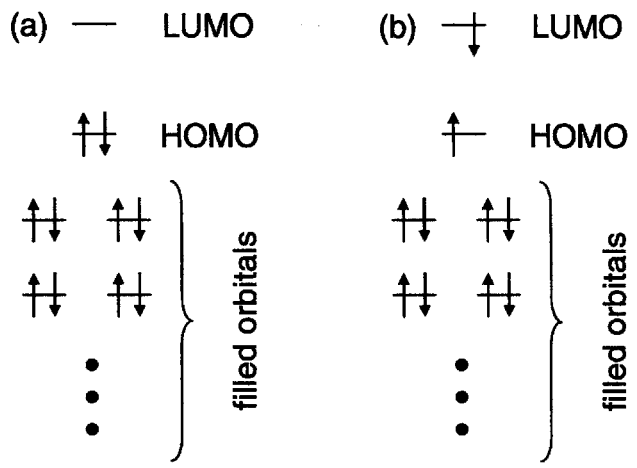


Fig. 2.1 – The energy levels of electrons in a molecule are solved under the Born-Oppenheimer and independent electron approximations. (a) The ground state of a molecule results from placing one spin-up and one spin-down electron into the lowest-energy orbital available, until all electrons are accounted for. (b) The lowest-energy excited state, or 'exciton', of a molecule. If the exciton is created optically, the two frontier electrons have the same spin configuration (singlet) as they did in the ground state in (a). If the exciton is created electrically, they may take any spin configuration (singlet or triplet).

binding energy is a direct result of the localized nature of the charges in organic semiconductors, which causes electrons and holes to interact strongly.[1,19]

This thesis is concerned with exciton spin. To introduce spin from first principles requires consideration of the relativistic Schrödinger equation. Instead, we introduce it in an ad-hoc fashion by multiplying the spatial part of the electronic wavefunction $\varphi$ by a spin wavefunction $\sigma$, which can have value $\uparrow$ or $\downarrow$. The simplest incorporation of spin would be to define a spin-containing orbital wavefunction $\psi$ by multiplying $\varphi$ of Eq. (2.8) by the spin wavefunction:

$$\psi = \prod_{i=1}^{N} \varphi_i^{(0)} \sigma_i \,. \tag{2.9}$$

This wavefunction, however, can not satisfy the Pauli exclusion principle. This principal states the total wavefunction (spin and spatial components together) of a collection of fermions must be antisymmetric under the exchange operation. The exchange operation swaps the overall wavefunction of the *n*th and *m*th Fermion. A consequence of the exclusion principle is that a wavefunction composed of two electrons, each with identical spin and spatial wavefunctions, must be identical to the negative of itself, in other words, it must be zero. A trivial example of Eq. (2.9) which does not satisfy the Pauli exclusion principle is $\psi = \varphi_1^{(0)} \sigma_1 \varphi_2^{(0)} \sigma_2$.[19,20]

The Pauli exclusion principle can be satisfied by wavefunctions which are linear combinations of the wavefunction shown in Eq. (2.9). One way to construct these linear combinations is through the use of a Slater determinant. The general form of a Slater determinant for a wavefunction containing $N$ electrons in their lowest energy state is

$$\psi(1,2,\ldots N) = \left(\frac{1}{N!}\right)^{1/2} \begin{vmatrix} \varphi_1(1)\left|\uparrow(1)\right\rangle & \varphi_1(1)\left|\downarrow(1)\right\rangle & \cdots & \varphi_{N/2}(1)\left|\uparrow(1)\right\rangle & \varphi_{N/2}(1)\left|\downarrow(1)\right\rangle \\ \varphi_1(2)\left|\uparrow(2)\right\rangle & \varphi_1(1)\left|\downarrow(1)\right\rangle & \cdots & \varphi_{N/2}(2)\left|\uparrow(2)\right\rangle & \varphi_{N/2}(2)\left|\downarrow(2)\right\rangle \\ \vdots & \vdots & \cdots & \vdots & \vdots \\ \varphi_1(N)\left|\uparrow(N)\right\rangle & \varphi_1(N)\left|\downarrow(N)\right\rangle & \cdots & \varphi_{N/2}(N)\left|\uparrow(N)\right\rangle & \varphi_{N/2}(N)\left|\downarrow(N)\right\rangle \end{vmatrix} \tag{2.10}$$

or, in shorthand notation,[19,20]

$$\psi = \left\| \varphi_1\left|\uparrow\right\rangle \;\; \varphi_1\left|\downarrow\right\rangle \;\; \cdots \;\; \varphi_{N/2}\left|\uparrow\right\rangle \;\; \varphi_{N/2}\left|\downarrow\right\rangle \right\|. \tag{2.11}$$

Here, $\varphi_n(m)\left|\uparrow(m)\right\rangle$ indicates the *m*th electron in the *n*th orbital, with spatial wavefunction $\varphi_n$ and spin $\uparrow$. The Slater determinant encodes the Pauli exclusion principle: placing three or

more electrons into the same orbital will cause two or more columns of the matrix to be identical, and the determinant to be zero; and, swapping any two electrons corresponds to swapping two columns, which changes the sign of the determinant.

An exciton is a bound state of just the two frontier orbital electrons. It can therefore have four possible spin states, because its component charges can each be up-spin ($\uparrow$) or down-spin ($\downarrow$). The four Slater determinant wavefunctions for an exciton are

$$\begin{aligned}
\psi^{\uparrow\uparrow} &= \left\| \varphi_1|\uparrow\rangle \;\; \varphi_1|\downarrow\rangle \;\; \cdots \;\; \varphi_{N/2}|\uparrow\rangle \;\; \varphi_{N/2+1}|\uparrow\rangle \right\| \\
\psi^{\downarrow\downarrow} &= \left\| \varphi_1|\uparrow\rangle \;\; \varphi_1|\downarrow\rangle \;\; \cdots \;\; \varphi_{N/2}|\downarrow\rangle \;\; \varphi_{N/2+1}|\downarrow\rangle \right\| \\
\psi^{\uparrow\downarrow} &= \left\| \varphi_1|\uparrow\rangle \;\; \varphi_1|\downarrow\rangle \;\; \cdots \;\; \varphi_{N/2}|\uparrow\rangle \;\; \varphi_{N/2+1}|\downarrow\rangle \right\| \\
\psi^{\downarrow\uparrow} &= \left\| \varphi_1|\uparrow\rangle \;\; \varphi_1|\downarrow\rangle \;\; \cdots \;\; \varphi_{N/2}|\downarrow\rangle \;\; \varphi_{N/2+1}|\uparrow\rangle \right\|
\end{aligned} \tag{2.12}$$

These wavefunctions are also not, however, spin eigenfunctions of the total spin operator. This can be seen by expressing the electronic wavefunction as a linear combination of these eigenfunctions,

$$\psi = c_1\psi^{\uparrow\uparrow} + c_2\psi^{\downarrow\downarrow} + c_3\psi^{\uparrow\downarrow} + c_4\psi^{\downarrow\uparrow} \tag{2.13}$$

and solving for the coefficients using the variational principle, in which the coefficients are varied and a minimum in the energy is found.[20]

A more intuitive way of seeing this is to consider how the angular momenta of the component charges of the exciton combine. Define $j$ to be the total angular momentum of a system composed of two spins $j_1$ and $j_2$. Then $j$ commutes with $j_1$ and $j_2$, but not with any of the $x$, $y$ or $z$ projections of $j_1$ or $j_2$. This means that it is not possible to specify both $j$ and any of these projections. Therefore there are two possible descriptions of the composite system. The uncoupled description

$$\left|j_1 m_{j1}; j_2 m_{j2}\right\rangle$$

specifies the total spin of each electron, and the $z$-projection quantum numbers $m_{j1}$ and $m_{j2}$ of each electron, but does not specify the relative orientations of the individual spins, nor the total spin of the composite system. The coupled description

$$\left|j_1 j_2; j m_j\right\rangle$$

does not specify $m_{j1}$ or $m_{j2}$, but does specify the total spin $j$ and its $z$-projection quantum number $m_j$. The individual wavefunctions in Eq. (2.12) are expressed in the uncoupled picture since the relative orientations of the component spins are specified. The coupled state can be expressed as a sum over uncoupled states as

$$\left|j_1 j_2; j m_j\right\rangle = \sum_{m_{j1}, m_{j2}} C_{m_{j1}, m_{j2}} \left|j_1 m_{j1}; j_2 m_{j2}\right\rangle, \tag{2.14}$$

where $C_{m_{j1}, m_{j2}}$ are called vector coupling coefficients.[19]

For the case of an exciton, treated as a two-electron system, the allowed list of composite spin values $j$ are given by the Clebsch-Gordan series,

$$j = j_1 + j_2, j_1 + j_2 - 1, \ldots, \left|j_1 - j_2\right|. \tag{2.15}$$

Therefore $j$ can have value 0 or 1. Using a shorthand for the composite state in the coupled picture, with the $j_1 j_2$ label dropped ($\left|j_1 j_2; j m_j\right\rangle \equiv \left|1, m_j\right\rangle$) we can say that the composite state $\left|1,+1\right\rangle$ must be composed of two up spins, $\left|\uparrow\uparrow\right\rangle$. Note that $\left|\uparrow\uparrow\right\rangle$ is the spin wavefunction alone. Similarly, the composite state $\left|1,-1\right\rangle$ must be composed of two down spins, $\left|\downarrow\downarrow\right\rangle$. The state $\left|1,0\right\rangle$ can be expressed as the resulting of applying the lowering operator $S_-$ on $\left|1,+1\right\rangle$, which gives

$$S_-|1,+1\rangle = \sqrt{2}\hbar|1,0\rangle. \tag{2.16}$$

Alternatively,

$$S_-|1,+1\rangle = (s_{1-} + s_{2-})|\uparrow\uparrow\rangle|\uparrow\uparrow\rangle = \hbar\left(|\uparrow\downarrow\rangle|\downarrow\uparrow\rangle + |\downarrow\uparrow\rangle|\uparrow\downarrow\rangle\right), \tag{2.17}$$

where $s_{1-}$ and $s_{2-}$ are the lowering operators for the component spins. Comparing Eqs. (2.16) and (2.17) gives $|1,0\rangle = \frac{1}{\sqrt{2}}\left[|\uparrow\downarrow\rangle|\downarrow\uparrow\rangle + |\downarrow\uparrow\rangle|\uparrow\downarrow\rangle\right]$. The only state remaining to be specified is $|0,0\rangle$ which must be consist of one or both of the states $|\uparrow\downarrow\rangle$ and $|\downarrow\uparrow\rangle$. Because every pair of spin states must be orthogonal to each other, $|0,0\rangle = \frac{1}{\sqrt{2}}\left[|\uparrow\downarrow\rangle|\downarrow\uparrow\rangle - |\downarrow\uparrow\rangle|\uparrow\downarrow\rangle\right]$ by comparison with $|1,0\rangle$. In summary, the spin states of the composite system consist of one state with total spin 0 ('singlet') and three states with total spin 1 ('triplets')[19]:

$$\begin{aligned} |0,0\rangle &= \frac{1}{\sqrt{2}}\left[|\uparrow\downarrow\rangle|\downarrow\uparrow\rangle - |\downarrow\uparrow\rangle|\uparrow\downarrow\rangle\right] \text{ (singlet)} \\ \left.\begin{aligned} |1,+1\rangle &= |\uparrow\uparrow\rangle \\ |1,0\rangle &= \frac{1}{\sqrt{2}}\left[|\uparrow\downarrow\rangle|\downarrow\uparrow\rangle + |\downarrow\uparrow\rangle|\uparrow\downarrow\rangle\right] \\ |1,-1\rangle &= |\downarrow\downarrow\rangle \end{aligned}\right\} &\text{(triplet)} \end{aligned} \tag{2.18}$$

These are the singlet and triplet spin wavefunctions. The corresponding total (spin and spatial) wavefunctions, using Eq. (2.12), are

$$\begin{aligned} \Psi_S &= \frac{1}{\sqrt{2}}\left[\psi^{\uparrow\downarrow} - \psi^{\downarrow\uparrow}\right] \\ \Psi_T &= \begin{cases} \psi^{\uparrow\uparrow} \\ \psi^{\downarrow\downarrow} \\ \frac{1}{\sqrt{2}}\left[\psi^{\uparrow\downarrow} + \psi^{\downarrow\uparrow}\right] \end{cases} \end{aligned} \tag{2.19}$$

The vector coupling coefficients for a two-electron system are listed in Table 2.1.

The coupling of individual spins into a composite system can also be considered pictorially. Fig. 2.2 shows a vector picture of the various exciton singlet and triplet states, under the coupled picture. The total spin $j$ is specified, as are the total spins of the component charges, but the $x$ and $y$ projections of the component spins cannot be known. These individual spins are therefore drawn as pointing along some unknown direction on the surface of a cone.

The classical interpretation of the cones in Fig. 2.2 is to consider them as describing spin precession in the presence of an external magnetic field pointing along the $z$-axis. Caution must be used with a classical vector picture of spin, however. While a vector can point in any direction, spin is quantized in the $z$ direction. Therefore, the individual spin vectors cannot add to give an arbitrary $z$-component. In addition, any classical object will return to its original configuration after undergoing at 360° rotation. A spin requires a 720° rotation to return to its original orientation.

The total spin of the interacting system is either $j = 0$ or $j = 1$. In the $j = 0$ case, the two electrons cancel each other's spin angular momentum exactly. In the $j = 1$ case, they sum maximally. For a singlet state to become a triplet state, therefore, spin angular momentum must be added. Similarly, spin angular momentum must be taken away for a singlet exciton to become a triplet exciton. The rate of spin angular momentum transfer to or from excitons and their precursor states in organic semiconductors, relative to the rates of exciton formation and recombination, is an open question addressed by this thesis. The conversion of singlet excitons to triplet excitons is usually called "intersystem crossing" or ISC.

| $m_{j1}$ | $m_{j2}$ | $\|1,+1\rangle$ | $\|1,0\rangle$ | $\|0,0\rangle$ | $\|1,-1\rangle$ |
|---|---|---|---|---|---|
| $+\frac{1}{2}$ | $+\frac{1}{2}$ | 1 | 0 | 0 | 0 |
| $+\frac{1}{2}$ | $-\frac{1}{2}$ | 0 | $\frac{1}{\sqrt{2}}$ | $\frac{1}{\sqrt{2}}$ | 0 |
| $-\frac{1}{2}$ | $+\frac{1}{2}$ | 0 | $\frac{1}{\sqrt{2}}$ | $-\frac{1}{\sqrt{2}}$ | 0 |
| $-\frac{1}{2}$ | $-\frac{1}{2}$ | 0 | 0 | 0 | 1 |

Table 2.1. Vector coupling coefficients for a two-electron system. The coefficients relate the projections of the spins of the individual electrons ($m_{j1}$ and $m_{j2}$), which are specified in the uncoupled picture, to the total spin of the system, which is specified in the coupled picture. From Ref. [19].

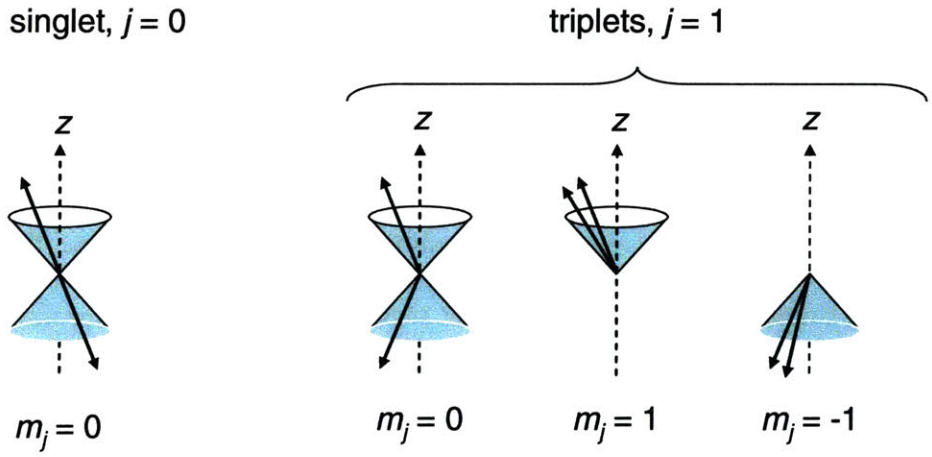


Fig. 2.2 – The singlet and triplet spin states of a bound electron-hole pair. The coupled picture is used, so that the total system spin $j$ is known, but the individual electron spin projections $m_{j1}$ and $m_{j2}$ are not. As a result, the individual spins are described as lying somewhere on a cone.

Another important feature of singlet and triplet states is their symmetry. Symmetry considerations place constraints on the allowable spin transitions, independent of angular momentum conservation. The singlet spin wavefunction $\varphi$ is antisymmetric under the particle exchange operator $P$, which swaps the wavefunctions of the two component electrons: $PS = P\frac{1}{\sqrt{2}}\left[|\uparrow\downarrow\rangle|\downarrow\uparrow\rangle - |\downarrow\uparrow\rangle|\uparrow\downarrow\rangle\right] = \frac{1}{\sqrt{2}}\left[|\downarrow\uparrow\rangle|\uparrow\downarrow\rangle - |\uparrow\downarrow\rangle|\downarrow\uparrow\rangle\right] = -S$. The triplet spin wavefunction $T$, on the other hand, is symmetric under the particle exchange operator, $PT = T$. Since in each case the Pauli exclusion principle requires that the overall wavefunction must be antisymmetric under particle exchange, the S and T spatial wavefunctions must be symmetric and antisymmetric, respectively, under particle exchange. The most important consequence of this symmetry consideration is that singlet excitons are allowed to decay to the ground state (which is singlet for every molecule considered here), while triplet excitons are not. This is explained further in the next section.[19]

### 2.4 The Importance of the Singlet Fraction

Photon emission or absorption involves the dipole operator, which cannot change a singlet state to a triplet state or vice versa. To see this, consider the dipole moment for the transition between a singlet state $S$ and a triplet state $T$:

$$\mu = -e\langle S|r_1 + r_2|T\rangle. \qquad (2.20)$$

The dipole moment cannot depend on the labeling of the electrons, so it cannot change sign if the electrons are exchanged. Since the dipole operator $r_1 + r_2$ is symmetric under the exchange operation, $\mu$ is non-zero only if the initial and final states are both $S$ or both $T$. In other words, photon emission (or absorption) cannot cause the spin state to change. The angular

momentum carried by an emitted photon therefore comes, not from the spin angular momentum, but from the orbital angular momentum of the electron that undergoes an energetic transition. The electron orbital is changed, for example, from $s$ to $p$.[17]

Furthermore, most stable organic semiconductors, including all of the ones commonly used in OLEDs and considered in this thesis, have filled frontier orbitals. Filled orbitals must be spatially symmetric under particle exchange and are therefore singlet in character. As a result, a triplet exciton is under normal circumstances forbidden from relaxing to the ground state through photon emission, and is dark, while singlet excitons are emissive. A result of this forbidden relaxation to the ground state is that triplet excitons have very long lifetimes (~ μs) compared to singlet excitons (~ ns), whose relaxation is allowed.

The forbidden nature of the relaxation process for excited states with triplet symmetry is the origin of the technological relevance of exciton spin and the motivation behind this thesis. Fundamentally, an OLED must attempt to produce an "optical" excitation (an excited state whose component spins are correlated) using electrically-injected charges with uncorrelated spins (Fig. 2.3). In the limit that every configuration of exciton (Eq. (2.19)) is formed with equal probability, 25% of excitons will be singlet, and 75% will be triplet and wasted. There are only two solutions: (1) remove the restriction on the decay of triplet excitons, which is the route taken by phosphorescent OLEDs (described in Section 2.8); or (2) cause the OLED to manufacture more singlet excitons, the possibility of which is demonstrated by this thesis.

The importance of spin to light emission is unique to OLEDs. That is because, in an organic semiconductor, an exciton with a well-defined spin symmetry mediates between the injection of charge, and the emission of a photon. While most solid-state lighting technology

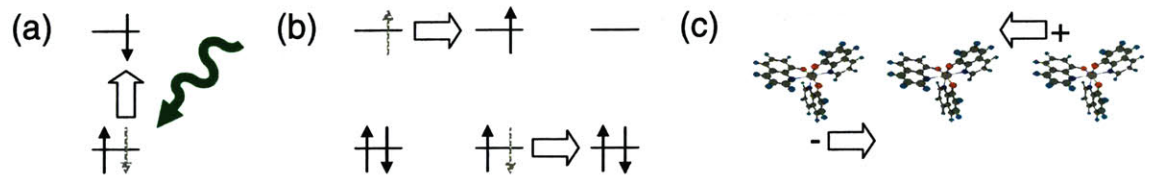


Fig. 2.3 – Optical and electrical exciton formation. An OLED must create an "optical" (singlet) exciton, but do so electrically. Large arrows indicate charge motion. (a) Optical formation. A photon excites an electron from the HOMO to the LUMO. The spin state of the two electrons is unchanged, and is always singlet for the materials considered in this thesis. (b) Electrical formation. An electron is pulled from the HOMO to a neighboring molecule, and an electron from another neighboring molecule is pushed into the LUMO. The spin state of the resulting exciton can be singlet or triplet. (c) An equivalent picture to (b). An electron is pushed from the left, and the removal of an electron from the HOMO is equivalent to a hole being pushed from the right.

is based on recombining charges, exciton binding energies in inorganic semiconductors are less than the thermal energy, making the exciton irrelevant to device function. Organic semiconductors distinguish themselves by their large exciton binding energies, greater than the thermal energy. Furthermore, due to the strongly localized nature of charges in organic semiconductors, there is consider orbital overlap and large exchange effects, causing energy splitting between different spin states (section 2.7). This reduces the likelihood of the mixing of spin states. The question of the degree of mixing is addressed in detail by this thesis.

### 2.5 Charge Transfer States

The positive and negative charges which are brought together to form an exciton under electrical pumping form a bound state when they are separated by less than a distance $r_c$ such

that $k_BT = k_Cq^2/r_c$, where $k_B$ is Boltzmann's constant, $T$ is temperature, $k_C$ is the electrostatic constant, and $q$ is the electronic charge.[22] This gives an $r_C$ of approximately 600 Å, or about 60 molecules apart. Electrical screening will reduce this distance, though the low dielectric constant of organic molecules makes screening a small correction. These bound states are known as "charge transfer" or CT states.[1] Since CT states consist of an electron and a hole, like an exciton, they may be singlet or triplet (Fig. 2.4). The importance of CT states results from the possibility that they are exchange-split (section 2.7). If they are, then singlet and triplet CT states have different energies, affecting the fraction of excitons which are ultimately formed in the singlet configuration.

### 2.6 Mixing Processes: Spin-Orbit Coupling

Spin-orbit coupling is a coupling between the magnetic field caused by the orbit of an electron around its nucleus, and the magnetic field caused by the spin of the electron. An electron orbiting around an atomic nucleus with radius $r$ and speed $v$ produces a current

$$I = \frac{-ev}{2\pi r}$$

and a magnetic dipole moment, whose $z$-component is

$$m_z = I\pi r^2 = -\frac{e}{2m_e} l_z ,$$

where $m_e$ is the electron mass, $e$ is the electron charge, and $l_z$ is the $z$-component of the orbital angular momentum of the electron. This magnetic dipole moment interacts with the magnetic moment **m** associated with the electron's spin angular moment **s**,

$$\mathbf{m} = 2\gamma_e \mathbf{s} ,$$

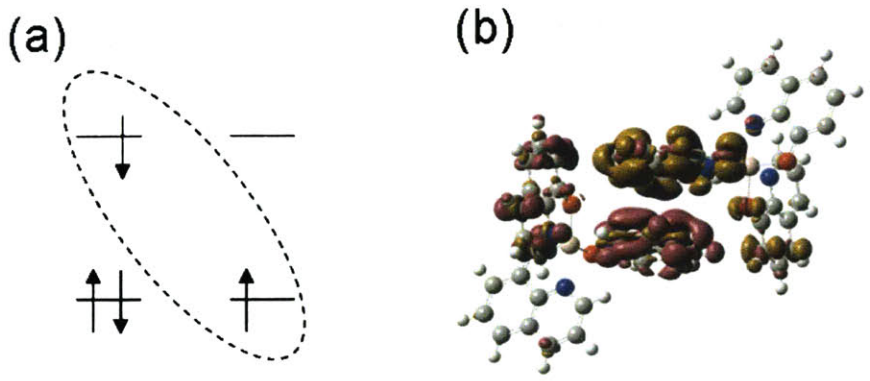


Fig. 2.4 Charge transfer states. (a) Under electrical excitation, a bound state is formed when the positive and negative charges which will form the exciton are on adjacent molecules. This is called a charge transfer, or CT state. The CT state may take the same spin symmetries as the exciton. Its component charges are indicated by the dashed oval. (b) A DFT calculation of positive (purple) and negative (gold) charge density in a CT state on two adjacent $Alq_3$ molecules. From Ref. [3].

where $\gamma_e$ is the gyromagnetic ratio of the electron. The corresponding spin-orbit Hamiltonian is[19]

$$H_{SO} = -\frac{e}{2m_e^2c^2r}\frac{d\phi}{dr}\mathbf{l}\cdot\mathbf{s}$$

where $\phi$ is the isotropic potential that the electron experiences. An electron in an exciton feels a hydrogenic potential, for which $H_{SO}$ varies as $Z^4$ where $Z$ is the atomic number. The energy of the spin-orbit interaction thus increases rapidly as the weight of the atom increases.

The spin-orbit Hamiltonian for a two-electron system is the sum of the individual interactions[17]

$$
\begin{aligned}
H_{SO} &= \xi_1 \mathbf{l}_1 \bullet \mathbf{s}_1 + \xi_2 \mathbf{l}_2 \bullet \mathbf{s}_2 \\
&= \frac{1}{2}(\xi_1 \mathbf{l}_1 + \xi_2 \mathbf{l}_2) \bullet (\mathbf{s}_1 + \mathbf{s}_2) + \frac{1}{2}(\xi_1 \mathbf{l}_1 - \xi_2 \mathbf{l}_2) \bullet (\mathbf{s}_1 - \mathbf{s}_2)
\end{aligned} \tag{2.21}
$$

where $\xi$ is the spin-orbit coupling constant. The operator $\mathbf{s}_1 + \mathbf{s}_2$ is symmetric under particle exchange. Since the transition moment between singlet and triplet states $\langle S|\mathbf{s}_1 + \mathbf{s}_2|T\rangle$ cannot depend on labeling, and gains a negative sign under particle exchange, it must be zero. The operator $\mathbf{s}_1 - \mathbf{s}_2$, on the other hand, is odd under particle exchange and is able to mix spins. Another way of considering this is to note that $\mathbf{s}_1 + \mathbf{s}_2$ commutes with the total spin operator $S^2$ and $\mathbf{s}_1 - \mathbf{s}_2$ does not. By Ehrenfest's theorem, if an operator commutes with the total spin operator, then the spin state cannot be changed by that operator.

The operator $\mathbf{s}_1 - \mathbf{s}_2$, then, is able to mix spins. It mixes a singlet exciton $|0,0\rangle$ into a triplet exciton with $m_j = 0$, ie, the state $|1,0\rangle$:

$$
\begin{aligned}
(s_{1z} - s_{2z})|0,0\rangle &= (s_{1z} - s_{2z})\frac{1}{\sqrt{2}}\{\uparrow(1)\downarrow(2) - \downarrow(1)\uparrow(2)\} \\
&= \frac{\hbar}{\sqrt{2}}\{\uparrow(1)\downarrow(2) + \downarrow(1)\uparrow(2)\} \\
&= \frac{\hbar}{\sqrt{2}}|1,0\rangle.
\end{aligned} \tag{2.22}
$$

Similarly, it mixes the triplet exciton $|1,0\rangle$ into the singlet exciton $|0,0\rangle$.

Spin-orbit coupling is pictured classically in Fig. 2.5. The electron spin axis precesses around the orbital magnetic field axis. In the case that the electron and hole that comprise the exciton experience different strengths of magnetic field, they will precess at different rates. Then, the spins of each charge precess with respect to each other at a rate proportional to this difference in magnetic field strength. During one complete revolution of the first spin with

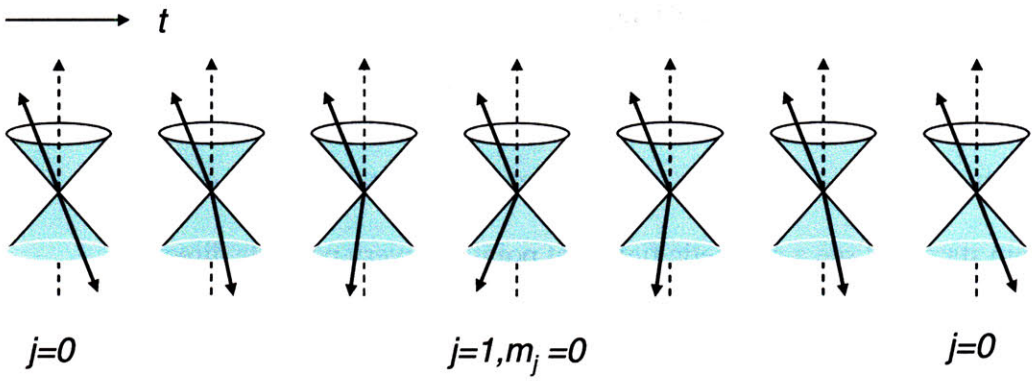


Fig. 2.5 – A classical model of spin dephasing. The component charges of an exciton or CT state experience slightly different magnetic field strengths, and precess at different rates about the $z$-axis. As a result, they dephase over time. A singlet state ($j = 0$) becomes a triplet state with $m_j = 0$, which in turn returns to a singlet state. In the case of spin-orbit coupling, the precession axis tumbles rapidly, allowing for a transition to any spin state.

respect to the second a singlet configuration is achieved once (when spins are aligned and sum to zero), and a triplet configuration with spin projection equal to zero ($T^0$) is achieved once, (when the z-components of the spin anti-align). Therefore spin-orbit coupling mixes $S_0$ and $T_0$.[23] Notice that the requirement for a gradient in field strength in this classical picture, is also present in the quantum picture: in Eq. (2.21), the spin mixing operator $\mathbf{s}_1 - \mathbf{s}_2$ is multiplied by $(\xi_1 \mathbf{l}_1 - \xi_2 \mathbf{l}_2)$.

The mixing process can also be considered intuitively from the perspective of the definition of the various singlet and triplet states in Eq. (2.18). Since a coupling between the orbital magnetic field and the spin of an electron can only cause the electron to precess, and cannot flip its spin, it is only able to introduce a phase change. The only states which differ by phase alone are $S_0$ and $T_0$. In other words, the operator $\mathbf{s}_1 - \mathbf{s}_2$ can not change the spin state of

$|1,1\rangle$ or $|1,-1\rangle$ (Eq. (2.22)). Note, however, that despite this fact, spin-orbit coupling effectively mixes all four possible spin states. This is because the rate at which orbital angular momentum tumbles (~ $10^{15}$ $s^{-1}$) is much faster than the rate of spin conversion, so that any given spin state will see a magnetic field that points in every possible direction.

An understanding of the dependence of the spin mixing rate on energy levels is important for this thesis. To develop this understanding, we use a time-dependent perturbation approach to describing mixing, following Griffiths.[24] We take unmixed singlet and triplet states to be eigenstates of an unperturbed Hamiltonian $H_0$ that form a complete set, so that any wavefunction can be expressed as a linear combination of $\Psi_S$ and $\Psi_T$. Then a mixing interaction is taken to be a perturbation $H_{MIX}$ to $H_0$, creating a perturbed wavefunction $\Psi'$ which can be expressed as[24]

$$\Psi' = c_S(t)\Psi_S e^{-iE_S t/\hbar} + c_T(t)\Psi_T e^{-iE_T t/\hbar}, \tag{2.23}$$

where $E_S$ and $E_T$ are the singlet and triplet energies, and $c_S$ and $c_T$ are coefficients weighting the two unperturbed wavefunctions. The probability of a transition from singlet to triplet state is then given by

$$P_{S\to T} = \rho(|E_S - E_T|)|c_T|^2, \tag{2.24}$$

where $\rho(E)$ is the phonon density of states at energy $E$ and

$$|c_T(t)|^2 \approx \frac{|E_{MIX}|^2 \sin^2(|E_S - E_T|t/2\hbar)}{|E_S - E_T|^2}, \tag{2.25}$$

with $E_{MIX} = \langle \Psi_S | H_{MIX} | \Psi_T \rangle$ the energy of the mixing interaction. A similar expression holds for $P_{T\to S}$. The transition probability is proportional to the phonon density of states because

phonons carry energy away from the transition event, or supply energy to it. It has been assumed here that the perturbation $H_{MIX}$ is small.

Eq. (2.25) shows that the strength of spin-orbit coupling is proportional to $E_{MIX}$ and inversely proportional to the energy difference between the mixed states. Therefore CT states are more susceptible to spin-orbit coupling than the excitons they form, because they are more delocalized, have less orbital overlap, and $|E_S - E_T|$ is smaller for them. In the limit that $|E_S - E_T| \approx 0$ for a CT state, a perturbative approach becomes inappropriate and Eq (2.25) does not hold. Eq. (2.25) also shows that the oscillation from $S$ to $T$ and back again is extremely rapid – for a typical excitonic $|E_T - E_S|$ of ~ 1 eV, the oscillation frequency is on the order of $10^{14}$ Hz. Since this is faster than other time scales in the system (with the notable exception of the change of direction of angular momentum), the states in a spin-mixed system can be seen as "hybrid" states, with triplets having some singlet character and vice versa. The degree of hybridization is given by $\left| E_{MIX} / E_S - E_T \right|^2$.

It is important to note that mixing can be considered to be "turned off" if $|E_S - E_T|$ is much larger than the energy of the spin-orbit interaction. If the mixing rate is sufficiently slow, then competing rates will overwhelm it, and the states are unlikely to be mixed. The size of the spin-orbit interaction for π-electrons is small,[25] generally less than 10 μeV,[26] and is expected to differ for excitons and CT states. When spin-orbit coupling rates are set high through the introduction of a heavy metal (section 2.8), a 4x quantum efficiency enhancement results. Triplets are given weak singlet character and begin to efficiently decay to the ground

state. Efficient mixing of singlet and triplet excitons is therefore clearly usually off. This thesis addresses the question of whether CT mixing is also usually off.

### Other Mixing Processes

In addition to spin-orbit coupling, the spin of an exciton can be mixed through the coupling of the spins of nearby electrons (electron-electron coupling), the coupling of the electron spin and nuclear magnetic moment (hyperfine coupling), and the coupling of the electron spin and the oscillating magnetic fields from neighboring molecules (spin-lattice coupling).[19] Hyperfine coupling in organic semiconductors is typically low because frontier charges are often in *p*-orbitals, which have zero probability density near the nucleus,[27] and because these charges are often localized on carbon atoms, which have no net nuclear spin. Spin-lattice interactions have been assumed to strongly mix CT states in polymers.[28-31] This thesis assumes that states of different spin multiplicity are easily mixed at room temperature if those states have the same energy, such as the three triplet states (Fig. 2.6).

## 2.7 Exchange effects

Electron-electron interaction has not been dealt with so far – in fact, it was explicitly dropped from the Hamiltonian in Eq. (2.7). Here it is re-introduced for the two frontier orbitals. Exchange effects are a class of electron-electron interaction that result from the spin angular momentum of the electron and have no classical analogue. They serve to lift the energy degeneracy of singlet and triplet states, and therefore can slow down or stop the mixing between those states. Two types of exchange interactions are considered here: *direct*

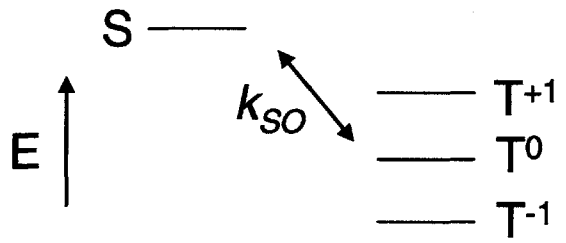


Fig. 2.6 – Spin-orbit coupling mixes singlet and triplet states with rate $k_{SO}$. Phosphorescent devices use this effect to achieve a ~4x efficiency enhancement. The three triplet states are approximately energy-degenerate in the absence of an external magnetic field (their splitting is exaggerated here), and can be assumed to be effectively mixed by interactions such as spin-lattice and spin-spin.

*exchange* and *kinetic exchange*. Both types of exchange result from the Pauli exclusion principle.

The energy of interaction between the electrons comprising a singlet state $S$, which is spatially symmetric under particle exchange is:[17]

$$\begin{aligned} E_+ &= \frac{e^2}{4\pi\varepsilon_0}\left\langle \psi_+ \left| \frac{1}{r_{12}} \right| \psi_+ \right\rangle \\ &= \frac{e^2}{8\pi\varepsilon_0}\left\langle a(1)b(2)+b(1)a(2) \left| \frac{1}{r_{12}} \right| a(1)b(2)+b(1)a(2) \right\rangle \\ &= J+K. \end{aligned} \tag{2.26}$$

For a triplet state $T$, which is spatially antisymmetric under particle exchange, the energy of interaction is:[17]

$$
\begin{aligned}
E_{-} &= \frac{e^2}{4\pi\varepsilon_0}\left\langle \psi_{-}\left|\frac{1}{r_{12}}\right|\psi_{-}\right\rangle \\
&= \frac{e^2}{8\pi\varepsilon_0}\left\langle a(1)b(2)-b(1)a(2)\left|\frac{1}{r_{12}}\right|a(1)b(2)-b(1)a(2)\right\rangle \\
&= J-K
\end{aligned}
\tag{2.27}
$$

where $J$ and $K$ are the Coulomb and exchange integrals respectively, defined as[17]

$$
J = \frac{e^2}{4\pi\varepsilon_0}\left\langle a(1)b(2)\left|\frac{1}{r_{12}}\right|a(1)b(2)\right\rangle \tag{2.28}
$$

and

$$
K = \frac{e^2}{4\pi\varepsilon_0}\left\langle a(1)b(2)\left|\frac{1}{r_{12}}\right|a(2)b(1)\right\rangle . \tag{2.29}
$$

From Eqs. (2.26) and (2.27), the singlet state is higher in energy than the triplet state by the direct exchange energy,

$$
\Delta E_{DE} = 2K . \tag{2.30}
$$

As $r_{12} \to 0$, $\psi_{-}$ becomes a very unlikely state, while $\psi_{+}$ actually has more probability density at $r_{12} = 0$.[19] Therefore the electrons in the $S$ state are on average further away from each other, minimizing the Coulombic stabilization of that state. As a result, T has *lower* energy than *S*, and *S* has *stronger* ionic character than *T*. This interaction is known as *direct exchange* (Fig. 2.7). The exchange splitting 2K between singlet and triplet excitons is on the order of 1.0 eV,[32] both in conjugated polymers and in small molecules.[17,19]

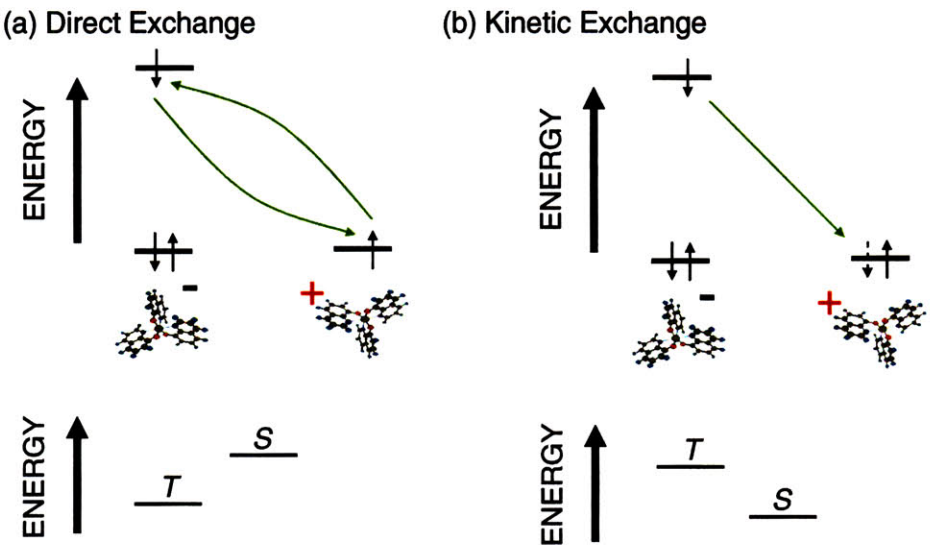


Fig. 2.7 – Direct and kinetic exchange for CT states. (a) When the electrons comprising the CT state are swapped, the overall (space times spin) CT wavefunction must gain a negative sign. This means that the spatial distribution of the charges, and the energy of the CT state, depends on the exchange symmetry of the spin state, which is different for singlets and triplets. Direct exchange lowers the energy of triplet states relative to singlet states. (b) The kinetic exchange interaction results from a "virtual recombination" of the electron in the LUMO with the ground state. Only singlet CT states can virtually recombine. As a result, kinetic exchange lowers the energy of singlet states with respect to triplet states.

*Kinetic exchange* in the context of an exciton or CT state is the virtual emission of the electron from the LUMO, followed by its virtual absorption by the HOMO level that contains a hole (Fig. 2.7).[33] In other words, the electron is delocalized, existing in a superposition of a higher-energy state (the LUMO) and a lower-energy state (the HOMO). This delocalization lowers the energy of the entire state relative to one in which the LUMO electron is restricted entirely to the LUMO. A HOMO occupied by a single electron can only "absorb" a second

electron if the two electrons are in the singlet spin configuration, since the ground state of the semiconductors considered here is singlet. Therefore kinetic exchange exists only for excited states in the singlet spin configuration, and lowers the energy of singlet states with respect to triplet states.[33]

Kinetic exchange causes the energy of a singlet excited state to be lowered with respect to the energy of a triplet excited state by[34]

$$\Delta E_{KE} \propto -\frac{b^2}{U}, \tag{2.31}$$

where $U$ is the energy difference between the LUMO and HOMO when each orbital is singly occupied, and $b$ is the overlap between these orbitals. The overlap is squared since the absorption of the electron by the HOMO is a virtual one, so that the electron effectively travels there and back to the LUMO.

Both direct exchange and kinetic exchange effects are proportional to the overlap of the orbitals of the states involved, and both therefore rapidly decrease in strength as the electron and hole are moved further away from each other. It is well known that singlet excitons are higher in energy than triplet excitons, so that for an electron and hole on the same molecule, $|\Delta E_{DE}| > |\Delta E_{KE}|$. It has been commonly assumed that for CT states, the same is true. It has also

been assumed that singlet and triplet CT states are different in energy by less than $kT$.[28-31] However, significant lifetime differences between singlet and triplet CT states have been measured for organic molecules in solution,[35] though to the author's knowledge, this has not been done in solid state. If the CT states are split, the singlet state may be lower than the triplet state, or vice versa. This is because it is uncertain whether kinetic exchange or direct

exchange will dominate. The decay with distance of $\Delta E_{DE}$ will differ from that of $\Delta E_{KE}$, since each term has a different dependence on the orbital overlap. Also, for CT states whose component charges are separated by large distances, kinetic exchange begins to fall as a power law in distance, since a charge may virtually hop from molecule to molecule. This will generally produce a kinetic exchange term that is large relative to the direct exchange term. Kinetic exchange is thus expected to dominate over direct exchange at large separation distances. The question of whether direct or kinetic exchange dominates CT states is addressed in Section 5.2 of this thesis.

## 2.8 OLED Efficiency, Phosphorescence and Sensitized Fluorescence

Having developed a language for discussing OLED light emission, we turn now to the actual device. The OLED external quantum efficiency is defined as[36]

$$\eta_{EQE} = \frac{N_{photon}}{I/q} = \eta_C \eta_{IQE}, \tag{2.32}$$

where $N_{photon}$ is the photon flux emitted from the device under stimulation by an electrical current $I$, and $q$ is the elementary charge, $\eta_C$ is the outcoupling efficiency, and $\eta_{IQE}$ is the internal quantum efficiency. The outcoupling efficiency is the fraction of emitted photons which reach the viewer, and are not absorbed or directed away from the viewer. The internal quantum efficiency is the efficiency with which injected charges are converted to photons at the molecular scale, and is the focus of this thesis.

The internal quantum efficiency can be broken up into several factors:[36]

$$\eta_{IQE} = \eta_R \left( \chi_T \eta_{PL,T} + \chi_S \eta_{PL,S} \right), \tag{2.33}$$

where the recombination efficiency, $\eta_R$, is the probability that an injected electron and hole will recombine to form an exciton; $\chi_T$ and $\chi_S$ are the triplet and singlet formation probabilities ($\chi_T + \chi_S = 1$); and $\eta_{PL,T}$ and $\eta_{PL,S}$ are the triplet and singlet emission quantum efficiencies. In general, emissive efficiency is given by[1]

$$\eta_{PL} = \frac{\sum_n k_R(n)}{\sum_n k_R(n) + \sum_m k_{NR}(m)}, \tag{2.34}$$

where $k_R(n)$ and $k_{NR}(m)$ are the *nth* and *mth* radiative and non-radiative rate respectively. Since triplets are forbidden from relaxing to the ground state through photon emission (section 2.4), triplet non-radiative recombination rates compete successfully with radiative recombination rates to drive triplet emission efficiency to zero. Therefore the external quantum efficiency is usually proportional to the singlet fraction $\chi_S$. In the limit of perfectly random exciton formation, this fraction is 0.25, so that 75% of injected charges are wasted.

The history of OLED external quantum efficiency is shown in Fig. 2.8. The progression can be assigned to changes in each of the factors of Eq. (2.33). In early OLEDs, very thick layers of organic materials were used.[37] While the external quantum efficiencies resulting were reasonable (about 5%), these devices required voltages on the order of 100 V and produced very

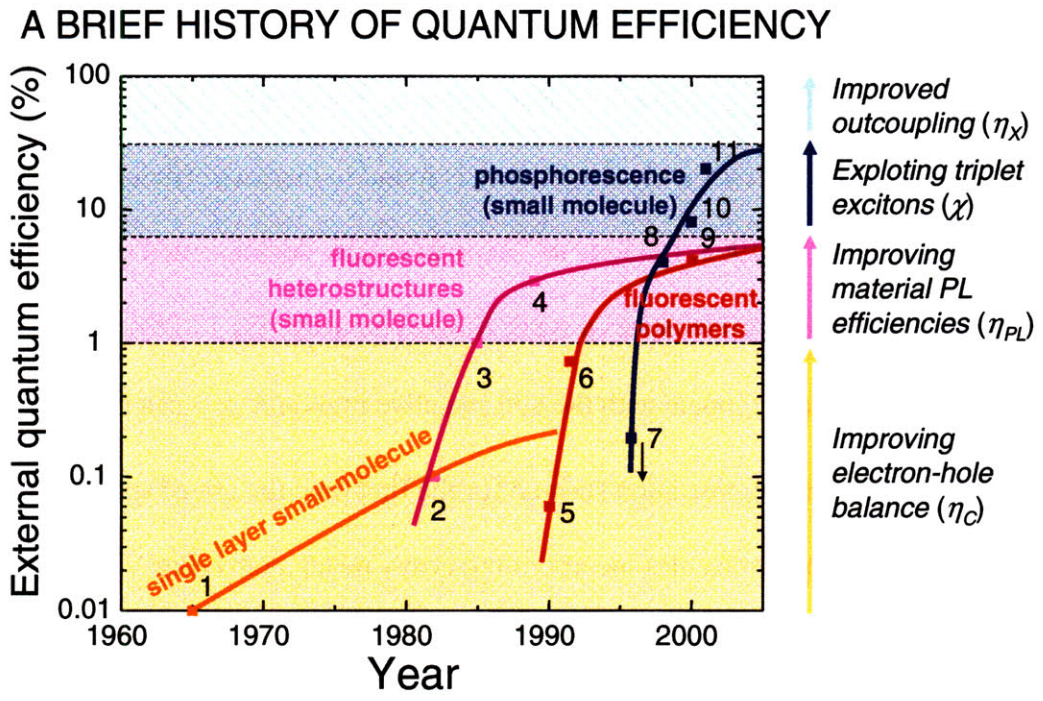


Fig. 2.8 – A history of OLED efficiency. Credit: Marc Baldo. Reference points: **1.** Helfrich & Schneider, PRL, 14, 229 (1965), **2.** Vincett, et al. Thin Solid Films, 94, 171 (1982), **3.** Tang & VanSlyke, APL, 11, 913 (1987), **4.** Tang, VanSlyke & Chen, JAP, 65, 3610, (1989), **5.** Burroughes, et al. Nature, 347, 539, (1990), **6.** Brown, et al. APL, 61, 2793, (1992), **7.** Hoshino & Suzuki. APL, 69, 224 (1996), **8.** Baldo, et al, Nature, 395, 151, (1998), **9.** Friend, et al. Nature, 397, 121, (1999), **10.** Baldo, et al, APL, 75, 4, (1999), **11.** Adachi, et al, JAP, 90, 5048, (2001)

low power efficiencies. To reduce the operating voltages, thin layers of organics were used, but $\eta_R$ dropped precipitously for thin films because much of the injected charge simply exited the device without meeting an oppositely-charged partner and recombining. As a result, the external quantum efficiency fell to < 0.1%.[38] In 1987, Tang and Vanslyke[39] introduced a heterostructure OLED consisting of thin hole transporting and electron transporting layers

with low minority carrier mobilities, forcing $\eta_R \sim 1$ (Fig 2.9). The external quantum efficiency rose back to 1%. Recombination efficiency is now generally assumed to be ~1, although the use of hole or electron blocking layers is found to increase efficiencies even in heterostructure devices.[40] In 1998, Baldo *et al*[36] experimentally demonstrated that spin-orbit coupling can be used to give triplet states a weak singlet character (Eq. (2.25)), so that an enhanced radiative rate can compete with the non-radiative rates and $\phi_{L,T}$ can be set to approximately unity. The demonstration showed for the first time the use of specially-designed "phosphorescent" molecules incorporating heavy metal atoms (Fig. 2.10). Excitons are formed directly on these phosphors, or transferred to them. In the case that the exciton is triplet, it can emit efficiently once on the dye due to its non-zero overlap with the singlet ground state. In the case that the exciton is singlet, it is quickly mixed by spin-orbit coupling to the lower-energy triplet state before emitting. As a result, virtually *all* excitons result in emission. This produces phosphorescent OLEDs with EQE's around 14% (from Universal Display Corporation's website). Phosphorescent emission is also used in an alternative scheme, sensitized fluorescence, to send excited states to a fluorescent guest (Fig. 2.10).

The subject of this thesis is the measurement and control of exciton spin. Given that phosphorescent OLEDs already allow all excitons to emit, why worry about exciton spin at all? First, exciton formation is at the core of OLED function and is important scientifically. In addition, the question has technological relevance. This can be appreciated by considering table 2.2, which shows the lifetimes and efficiencies of blue, red and green phosphors available from Universal Display Corporation, the leading supplier of phosphorescent materials.

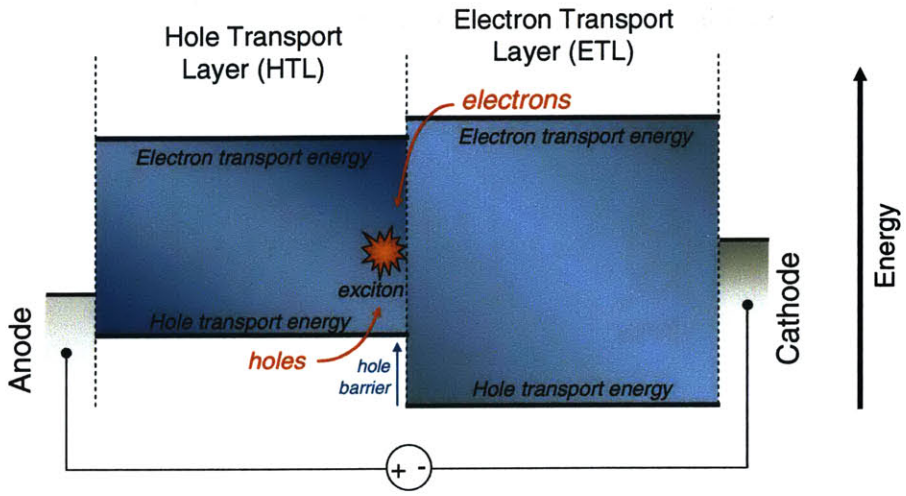


Fig. 2.9 – A heterostructure OLED. Electrons and holes are injected from opposing contacts into electron and hole transport layers. They accumulate at the interface between the two layers, encouraging the formation of electron-hole bound states called 'excitons'. Exciton decay then leads to photon emission. All light emission from OLEDs is therefore mediated by exciton formation.

While red and green phosphorescent emission is efficient and long-lived, blue phosphorescence currently lags behind. At a standard display brightness of 500 cd/m$^2$ (the brightness of a modern LCD panel) blue phosphorescence is predicted to last 3100 hours using a scaling equation,[14] below what is usually taken as the minimum for commercial feasibility (10,000 hours). By comparison, running a device for 12 hours a day for 10 years would take 44,000 hours. White lighting applications will require similarly high brightnesses.

In addition, while the UDC red and green phosphors are well-saturated, blue is not. Color saturation is usually considered on the *International Commission on Illumination* (CIE) color gamut shown in Fig. 2.11. Each color is represented by an $x$ and $y$ coordinate. Mixing two colors can produce any color on the line joining those colors in the gamut; mixing three

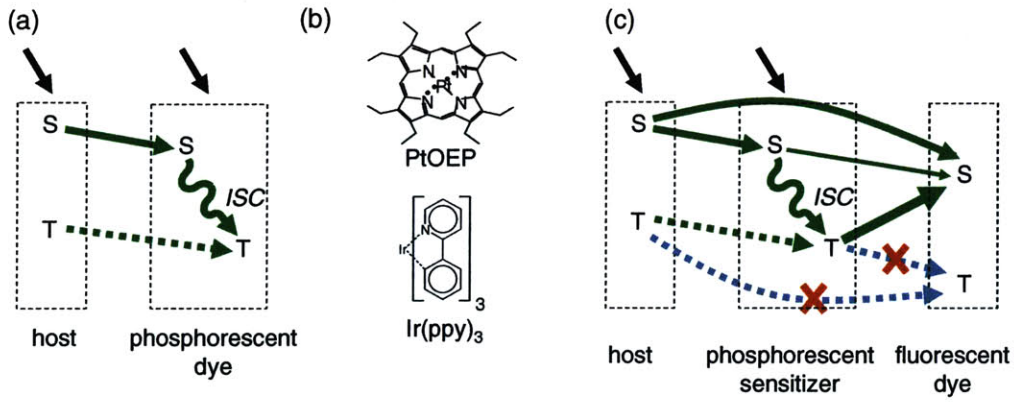


Fig. 2.10 – Two schemes for addressing the singlet fraction limitation. (a) Phosphorescence. A phosphorescent dye, containing a heavy atom, is doped into a host. Excitons formed on both the host and guest transfer to the triplet state of the dye, which is responsible for light emission. (b) Two phosphorescent dyes: Pt(II) octaethylporphine (PtOEP) and Tris(2-phenylpyridine) iridium (III) ($Ir(ppy)_3$). The heavy metal in these dyes is responsible for creating high spin-orbit coupling strengths. (c) Sensitized fluorescence, from Ref. [41].A phosphorescent dye and a fluorescent dye are doped into a host. Emission occurs from the fluorescent dopant singlet state, which gathers both singlet and triplet excited states from both the host and the phosphorescent dye. Both phosphorescence and sensitized fluorescence require an emissive phosphor. Black arrows indicate direct exciton formation.

colors can produce any color in the triangle those colors form. The color gamut created with UDC's phosphors is illustrated with a solid line. If the UDC blue is replaced by the blue fluorophore PMC,[42] the dashed-line gamut results. To see the importance of this difference on a real-world display, Fig. 2.12 shows the default Windows XP background image, using UDC's phosphors, and again using UDC's red and green phosphors, plus the blue fluorophore

| color | CIE coordinates | EQE (%) | Lifetime to 50% (000's hrs) | Initial Luminance (cd/m^2) | Calculated Lifetime from 500 cd/m^2 in. lum. (000's hrs) |
|---|---|---|---|---|---|
| red | (0.68,0.32) | 14 | 320 | 500 | 320 |
| green | (0.33,0.63) | 10 | 40 | 1000 | 149 |
| blue | (0.16,0.29) | 11 | 17.5 | 200 | 3.1 |

Table 2.2. Universal Display Corporation's red, green and blue phosphors. The right-most column is a calculation of the expected lifetime from an initial luminance of 500 cd/m$^2$, the maximum brightness of a new Sony 42" LCD panel. The calculation uses a power-law dependence of lifetime $L$ on brightness $B$, $L \propto B^{-\alpha}$ (ref [14]) where $\alpha$ is a decay constant calculated from UDC's data. Running a device for 12 hours a day for 10 years translates into 44,000 hours.

PMC.[42] Current industry practice is to use phosphorescent red, but fluorescent green and blue. It should be noted that a microcavity together with a highly-scattering substrate can sharply increase the saturation of emission from an OLED.[43] This represents a solution for the blue phosphorescence saturation problem. This thesis presents an alternative approach to creating blue emission that is both saturated and efficient:: namely, to increase the efficiency of an already saturated blue *fluorophore*, by increasing the fraction of excitons which form as singlets.

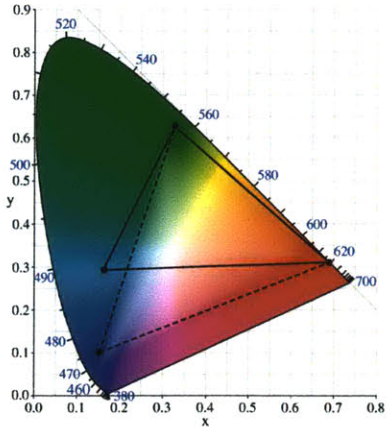


Fig. 2.11 – (a) The *International Commission on Illumination* (CIE) chart defines colors by an $(x,y)$ coordinate pair (from Wikimedia). A 3-color display is capable of producing colors inside a triangle with vertices defined by those colors. The solid triangle uses commercially available phosphors (from Universal Display Corporation). The dashed triangle uses UDC's red and green phosphors, and the blue fluorophore PMC.

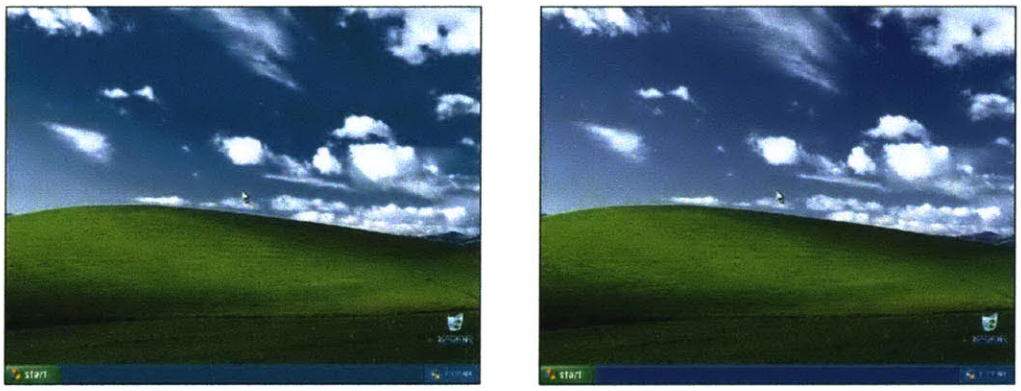

Fig. 2.12 – The Windows XP background produced using (a) UDC's red, green and blue phosphors and (b) UDC's red and green phosphors, together with the blue fluorophore PMC.[42] The images were produced by locating each original pixel on the CIE chart of Fig. 2.11, then moving the pixel to the closest color possible for the set of dyes used.

## 2.9 Frozen and Degenerate?

Fig. 2.13 shows a general rate diagram for exciton formation, taking into consideration the singlet and triplet formation channels and mixing between them. At this point this is the most general rate model that we can write down. We define two channels of formation and allow mixing between the channels at each step.

The three requirements for singlet and triplet states to be effectively mixed are:

1. A mixing interaction, capable of changing the symmetry and momentum of a state, is present;

2. $|E_S - E_T|$ is small relative to the energy of the mixing interaction, $E_{MIX}$ (Eq. (2.35)); and

3. There is a sufficient phonon density of states available at the energy $|E_S - E_T|$.

As discussed above, the excited states can be considered to be in a spin angular momentum bath (provided by spin-lattice, spin-orbit and spin-spin interactions) which satisfies condition 1. The four-times increase in efficiency observed from phosphorescent OLEDs indicates that condition 3 is usually satisfied. The question is simply when condition 2 is satisfied. The energy of the *S*-*T* splitting increases as the charges come together (Eqs. (2.29), (2.30) and (2.31)). In fact, because the exchange interaction varies with the orbital overlap of the two charges, which falls exponentially with distance, then if mixing ever turns off, it can be defined to do so at a certain integer $m$ - 1. In other words, the case of a gradual weakening of mixing rates is not considered: instead, mixing is taken to be fully "on" at $m$ and "off" at $m$ - 1. Note that since the typical mixing interaction strength in an organic semiconductor is on the order of 10 μeV << $k_BT$ at room temperature,[26] the mixing rate of singlet into triplet states is

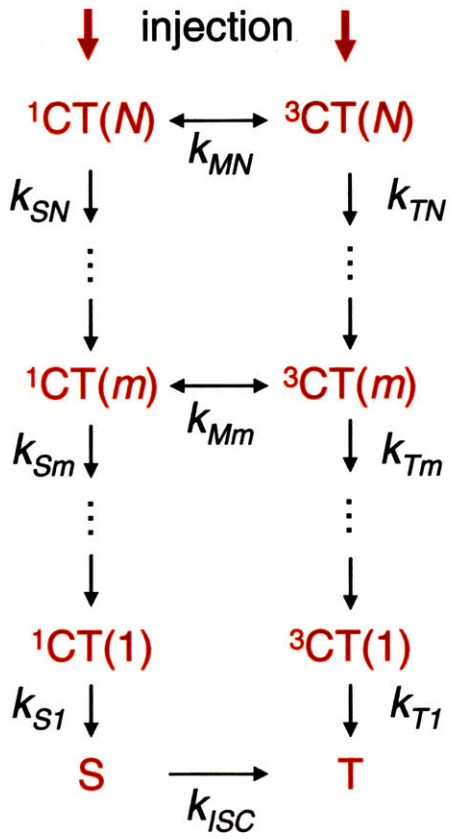


Fig. 2.13 – A rate diagram for electrical formation of singlet excitons S and triplet excitons T. Three kinds of states are involved: mixed CT states, unmixed CT states, and excitons. Charges are injected from contacts and are initially $N$ molecules apart. Because charges in organic semiconductors are localized, the distance between the charges changes discretely as they hop towards each other. For $n$th nearest neighbors, a charge pair in a singlet configuration $^1$CT($n$) may hop closer together to make $^1$CT($n$-1) with rate $k_{Sn}$ , or may change its spin symmetry to form a triplet charge pair $^3$CT($n$) with rate $k_{Mn}$. Similarly, $^3$CT($n$) may keep its spin symmetry and form $^3$CT($n$-1) at rate $k_{Tn}$ or change its spin symmetry to form $^1$CT($n$). The energy difference between $^1$CT($n$) and $^3$CT($n$) grows as $n$ decreases, due to exchange interactions (section 2.7). Mixing turns off when this energy difference is much greater than the mixing interaction energy $E_{MIX}$. Because the exchange interaction strength grows exponentially with each hop, mixing is taken to turn "off" at some separation $m$, rather than to gradually decrease. Whether mixing ever turns off in the typical organic semiconductor is addressed in Chapters 3-5. For the typical organic semiconductor $E_{MIX} \approx 10$ μeV, which is less than $k_BT$, even at cryogenic temperatures. Therefore, for $E_{MIX}$ greater than the exchange splitting, singlets mix into triplets as quickly as triplets into singlets. For mixing interaction energies on the order of $k_BT$, mixing rates for $n > m$ are turned on, and may be asymmetrical, favoring the lower energy state, singlet or triplet, as the case may be. The mixing process between singlet and triplet *excitons* favors triplet exciton formation, since the triplet exciton is lower in energy. In the absence of spin-orbit coupling, $k_{ISC}$ is low.

taken to be equal to the reverse rate, of triplet into singlet states. This is because the energy splitting required for an asymmetrical mixing rate must be comparable to $k_BT$, and such a large splitting would turn off mixing altogether. This assumption will not hold for mixing interaction strengths on the order of $k_BT$.

For $n \geq m$, then, the rate of singlet into triplet mixing equals the rate of triplet into single mixing, and is labeled $k_{Mn}$ for $n^{th}$ nearest neighbor CT states. In this regime states are equally mixed among three triplet and one singlet state. For $n < m$, singlet and triplet states become significantly energy split, and mixing is off. The fraction of excitons which form as singlets is given by the rates of the last-mixed CT state:

$$\chi_S = \frac{k_{Sm}}{k_{Sm} + 3k_{Tm}}. \qquad (2.36).$$

Fig. 2.14 shows a continuous version of this picture. When the distance separating an electron and hole is large, they do not interact. As the electron and hole approach each other, they begin to stabilize each other. At a distance $r_C$ the electron and hole become bound, and at a distance $r_K$, exchange effects become sufficient to turn off mixing. Thus CT($m$) in Fig. 2.13 has an electron-hole separation distance of $r_K$. If kinetic exchange dominates direct exchange, then the singlet energy is lower at $r = r_K$; otherwise, the triplet energy is lower. Finally, excitons are formed, with the triplet exciton energy lower.

At the most general level, the question this thesis addresses is whether CT mixing ever turns off. If it does, then $m > 1$. Which case is true depends both on the strength of the mixing interaction and on the energy by which CT states are split. While it has been assumed that mixing is always "on",[29-31] a direct measurement of either of these parameters has not, as far

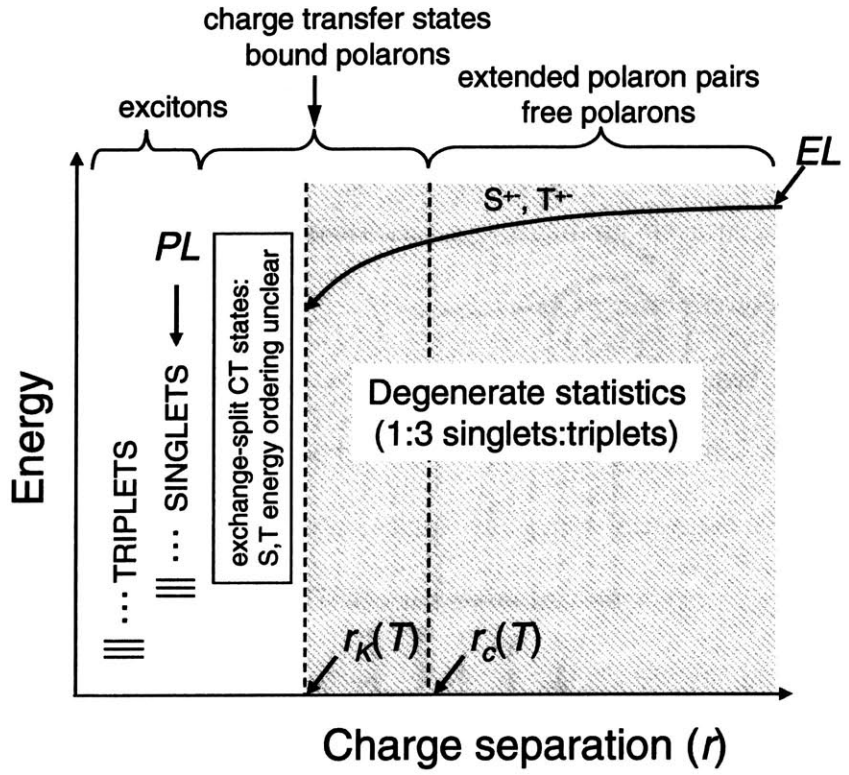


Fig. 2.14 – A continuous version of the exciton formation picture in Fig. 2.13. In electroluminescence (EL), injected electrons and holes stabilize each other as they move together. They become bound at a separation distance $r_C$, and are sufficiently exchange-split to turn mixing off at a distance $r_K$. CT states separated by $r_K$ are CT($m$) in Fig. 2.13. Finally, when the electron and hole occupy a single molecule, they form an exciton. Triplet excitons have lower energy than singlet excitons due to the direct exchange interaction (Fig. 2.7). The energetic ordering for CT states is unclear. In photoluminescence, singlet excitons are created directly (Fig. 2.3). Adapted from Ref. [22].

as the author knows, previously been done for small molecular organics in the solid state. This thesis provides evidence that $1 < m < 5$ in the prototypical small-molecular organic

semiconductor, $Alq_3$, and that $m > 1$ for the CT state formed between two red fluorophores (DCM1 and DCM2), and the electron transporting material BCP.

These questions have been explored to some degree in the literature. CT mixing rates in polymers have been investigated through electric field induced delayed fluorescence. In this scheme, a sample is optically pumped, and an electric field is applied to pull excitons apart into geminate (spin-correlated) CT states. The charges are allowed to recombine when the field is later turned off. Figure 2.15 shows the result of such an experiment performed on a phosphorescent polymer. Because the light emission with charge recombination (when the field is turned off) is significantly larger in the singlet channel than in the triplet channel, it is argued that no significant $S \rightarrow T$ mixing occurs over the duration of the 3 μs – long field pulse.[44] In the language of Fig. 2.13, it is suggested that $k_{MI} < 0.3\ \mu s^{-1}$, or slower than the expected $k_{SI}$ and $k_{TI}$ rates. In addition, thermally stimulated luminescence measurements find an energy splitting of 3 – 6 meV between the singlet and triplet CT states of another conjugated polymer,[45] considerably larger than the expected energy of the mixing interaction, suggesting that mixing is off in this system as well.

However, the interpretation of the delayed fluorescence measurement has been contested on the grounds that the fluorescent emission increase normalized to the total device fluorescence cannot be simply compared to the equivalent phosphorescent measure. This is because it is expected that triplet population densities will be much higher than singlet densities.[46] Instead, the delayed fluorescence can be interpreted as the result of triplet-triplet annihilation (TTA), rather than geminate pair recombination. Indeed, the dynamics of delayed fluorescence recovery are consistent with TTA,[46] as is the fact that the decay constants of the singlet and triplet channels are nearly identical. Furthermore, this kind of measurement has

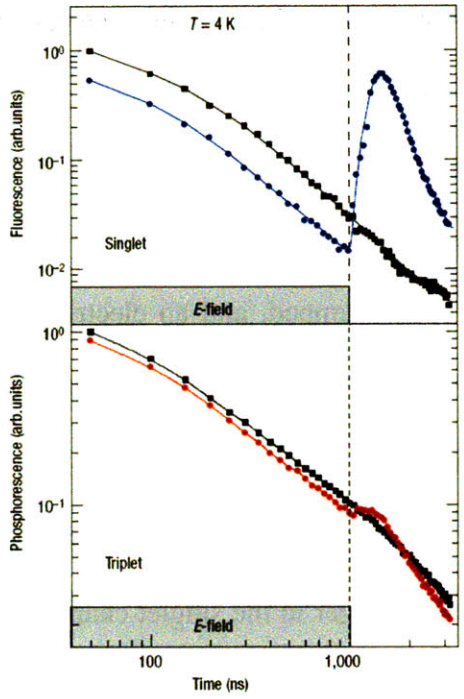


Fig. 2.15 – Data from an electric field induced delayed fluorescence measurement on a phosphorescent polymer by Reufer *et al.*[44] On turning off the field, a large fluorescent and small phosphorescent burst are observed. Black lines indicate PL dynamics in the absence of a field. The authors argue that the electric field breaks singlet excitons into singlet CT states, which recombine as singlets after the field is turned off, indicating that mixing has not occurred. Rothe *et al* contest this interpretation, pointing out that a large triplet population will be present, lowering the relative size of the phosphorescent burst.

not been performed on small molecules, to the knowledge of the author. Therefore the question of the CT state mixing rates remains an open one.

A related question is what are the values of $k_{S1}$ and $k_{T1}$. If they are identical, then it is likely that $k_{Sn}$ and $k_{Tn}$ are identical as well, since the singlet and triplet states are most distinguished from one another in the exciton state. Then the question of mixing would be

irrelevant, with $\chi_S = 0.25$ regardless of mixing rates. The relative values of the rates $k_{SI}$ and $k_{TI}$ have been considered extensively in the literature for polymers. The singlet formation rate has been argued to exceed the triplet formation rate ($k_{SI} > k_{TI}$) as a result of the low energy difference between the singlet CT state and the singlet exciton, relative to the corresponding energy difference for triplet states.[47,48.,49] In addition, the spatially smaller singlet exciton has more ionic character than the more diffuse triplet exciton, giving it stronger ionic character and a stronger wavefunction overlap with its CT state precursor.[31]

Attention to the relative values of $k_{SI}$ and $k_{TI}$ has been motivated by measurements of singlet fractions in polymers which greatly exceed the 25% degenerate limit. At the same time, small molecules have been measured to satisfy this limit.[50] Therefore, the reasons given above for why high singlet fractions may result, have been taken as unique to polymers. For example, it has been argued that $k_{SI} > k_{TI}$ in polymers, but not small molecules, because of the more delocalized nature of excitons and CT states in polymers. However, this thesis argues that, even in small molecules, $k_{SI}$ and $k_{TI}$ are markedly different, and that the observation of degenerate statistics in small molecules is in fact the result of low mixing rates between CT(1) states (Section 5.3). Given the very large exchange splitting typical of the tightly-confined excitons in small molecules (0.7 eV in $Alq_3$, from ref. [51]), it cannot be too much of a surprise that $k_{SI}$ and $k_{TI}$ are different in small molecules as well as polymers.

# Chapter 3. Measuring Excitonic singlet-triplet ratios

## 3.1. Introduction

As described in the introduction, the fraction of excitons which form as singlets represents a basic efficiency limit for OLEDs, and is also an important manifestation of the dynamics of exciton formation.[28,50,52-55]. The ability to correctly measure the fraction $\chi_S$ of excitons which form as singlets is therefore an important one. Phosphorescent molecular organic light emitting devices (OLEDs) exhibit efficiencies approximately four times that of molecular OLEDs that fluoresce from singlets alone, consistent with the spin-degeneracy limit.[56] But other experiments suggest that exciton statistics in *polymeric* semiconductors may favor luminescent singlets over non-emissive triplet excitons.[28,52-55] If so, fluorescent polymers may possess intrinsically higher electroluminescent efficiencies than fluorescent small molecules, although to date this difference has not been consistently observed.

It is apparent, therefore, that an accurate determination of the singlet-to-triplet ratio is essential to understanding the physical mechanisms leading to electroluminescence in organic thin films. Yet while many authors have reported this formation ratio, there remains disagreement as to its value, particularly in technologically interesting luminescent polymeric semiconductors. Several previous studies of exciton formation have been based on a comparison of the electroluminescent (EL) and photoluminescent (PL) efficiencies of a particular material.[50,52-54] In this chapter, a simple technique is described that avoids many systematic errors that may arise in comparative measurements. As a demonstration, the two

archetypal luminescent compounds, tris(8-hydroxyquinoline) aluminum ($Alq_3$) and poly[2-methoxy-5-(2-ethylhexyloxy)-1,4-phenylenevinylene] (MEH-PPV), are analyzed and found to possess singlet fractions of (20±1)% and (20±4)%, respectively. Results are confirmed using a sensitive synchronous detection scheme.

Section 3.2 describes the theory of reverse bias measurements of PL efficiencies, and Sec. 3.3 describes the experimental details of the measurement of singlet fractions. Section 3.4 presents the measured PL efficiencies for $Alq_3$ and MEH-PPV OLEDs. In Sec. 3.5 the singlet fractions are determined for $Alq_3$ and MEH-PPV, and a model for EL-specific losses is proposed to place an upper bound on the singlet ratio in these materials. The detection of degraded materials is discussed in Sec. 3.6, different measurement techniques are compared in Sec. 3.7, and possible material dependencies in the singlet fraction are discussed in the conclusion, Sec. 3.8.

## 3.2. Theory of Reverse Bias Measurement of PL Efficiency

### 3.2.1 Introduction

Fig. 3.1 depicts the states relevant for describing the reverse bias measurement technique. Optical excitation generates high-energy singlet excitons, S*, that may relax to the lowest excited singlet exciton, S, with rate $k_{S*}$; S* can also cross over to an excited

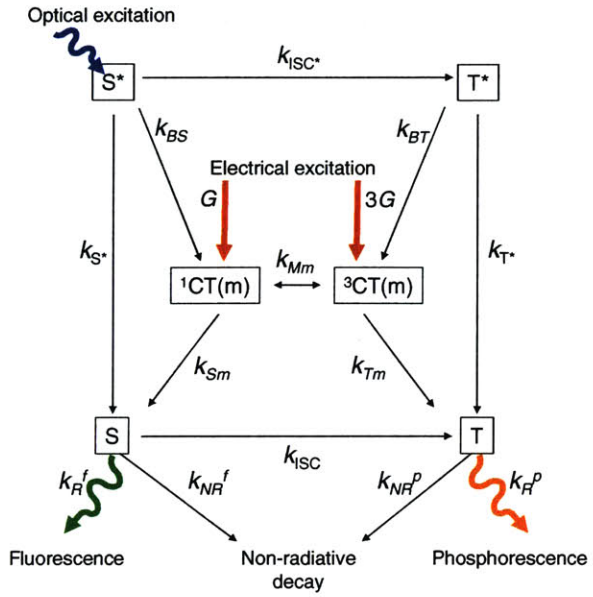


Figure 3.1 – Optical versus electrical exciton formation. Singlet and triplet CT states with $n < m$ (Fig. 2.13(a)) relax into singlet and triplet excitons, respectively, and are not shown. CT states with $n >$ m are degenerate and re-mixed at the $m$th stage, and are not shown.

triplet exciton, T*, with rate $k_{ISC*}$ or charge-separate to a lower-energy CT state with rate $k_{BS}$. Similarly, the excited triplet can charge separate with rate $k_{BT}$ or decay to a relaxed triplet with rate $k_{T*}$. The rates $k_{Sm}$ and $k_{Tm}$ are the formation rates of singlet and triplet excitons, respectively, from *degenerate* CT states, *ie*, the last mixed CT state, CT($m$) (Fig. 2.13(a)). Electrical excitation then proceeds through polaron pairs and CT states that ultimately collapse to excitons (Fig. 2.13). The CT states considered in Fig. 3.1 have $n = m$ (Fig. 2.13(a)), or equivalently, $r = r_K$ (Fig. 2.14). CT states with $r < r_K$ are assumed to relax directly to their respective singlet and triplet excitons and are not explicitly shown. The formation rates for singlet and triplet excitons from *nondegenerate* CT states ($n < m$), with no effective mixing, will have no effect on the ratio of singlet to triplet excitons formed. Similarly, CT($n$)

states with $n > m$ ($r > r_K$) are re-mixed at $n = m$ and are not considered. The rates $k_{Sm}$ and $k_{Tm}$ are central to interpreting recent studies of polymer emission.[28,52-55]

Once the singlet and triplet states are split at $r < r_K$, mixing effectively ceases under small perturbations, so that there is no mixing rate between singlet and triplet states. However, intersystem crossing from S to T at lower energy is possible for excitons with rate $k_{ISC}$, respectively. Although typically small, $k_{ISC}$ may be significantly enhanced in the presence of heavy atoms such as Pt or Ir, which greatly increase the strength of spin-orbit coupling, and hence the population of triplet excitons. Intersystem crossing from high-energy S* to T* may proceed at different rates than from the lowest S to T. Indeed, high-energy photoexcitation of anthracene has been observed to result in a singlet-to-triplet ratio of 1:1, while low-energy photoexcitation results in a 1:3 ratio.[57]

Exciton formation statistics determine the external quantum efficiency of electroluminescence in an OLED, $\eta_{EL}$:[53]

$$\eta_{EL} = \chi_S \gamma \eta_C \eta_{PL} \tag{3.1}$$

where the fraction of excitons formed as singlets is $\chi_S$, $\eta_{PL}$ is the intrinsic PL efficiency, the light output coupling fraction, $\eta_C$, is the fraction of emitted photons captured by the detector, and $\gamma \leq 1$ measures losses present in EL but not in PL.[53]

The product $\eta_C \eta_{PL}$ is determined by optically exciting the luminescent organic film within an OLED placed under reverse electrical bias. The electric field dissociates some excitons into charges,[1,58,59] reducing the PL and generating photocurrent, thereby providing an accurate measurement of the number of excitons dissociated. As shown below, the ratio of the change in PL to the photocurrent gives $\eta_C \eta_{PL}$. Because this technique also allows for the

measurement of $\eta_{EL}$ in the same experimental geometry used to measure $\eta_{PL}$ by applying forward bias to the luminescent film and injecting charges, it is not necessary to explicitly measure $\eta_C$, avoiding uncertainties commonly associated with this measurement. In addition, this technique can act as a probe for CT states; and, because the PL efficiency is obtained by a comparison of $\Delta PL$ to $I_{ph}$, the strength of absorption of pump light by the organic material does not affect the result.

The PL power ($P_{PL}$) emitted by the optically excited film is given by:

$$P_{PL} = \eta_C h\nu \frac{k_R}{k_R + k_{NR} + k_Q} \phi \tag{3.2}$$

where $\phi$ is the photon flux from the excitation source absorbed within the film, $k_R$ is the radiative exciton recombination rate, $k_{NR}$ is the non-radiative decay rate, $k_Q$ is the rate of electric field-induced exciton quenching, $h$ is Planck's constant, and $\nu$ is the frequency of the radiated photons. For weak field-induced quenching (i.e. $k_Q \ll (k_R + k_{NR})$), the drop in PL may be expressed in terms of the PL efficiency in the absence of an applied field, i.e. $\eta_{PL} = k_R/(k_R + k_{NR})$, to obtain:

$$\Delta P_{PL} = P_{PL}(k_Q) - P_{PL}(k_Q = 0) \approx -h\nu\eta_C\eta_{PL} \frac{k_Q}{k_R + k_{NR}} \phi \tag{3.3}$$

In all devices used in this study, the field-induced PL quenching satisfies $k_Q \ll (k_R + k_{NR})$. The photocurrent resulting from field-induced dissociation of excitons is:

$$I_{ph} = q \frac{k_Q}{k_R + k_{NR} + k_Q} \phi \tag{3.4}$$

where $q$ is the electronic charge. Assuming that $k_Q \ll (k_R + k_{NR})$, Eqns. (3.3) and (3.4) give:

$$\eta_C \eta_{PL} = -\frac{q}{h\nu}\frac{\Delta P_{PL}}{I_{ph}} \tag{3.5}$$

Since the EL power, $P_{EL}$, at an injected current, $I_{inj}$, is given by $P_{EL} = qI_{inj}h\nu\eta_{EL}$, and using Eq. (3.1), we can write:

$$\chi_S \gamma = \frac{\eta_{EL}}{\eta_C \eta_{PL}} = \frac{P_{EL}}{I_{inj}} \Big/ \frac{-\Delta P_{PL}}{I_{ph}} \tag{3.6}$$

Thus, spin statistics are obtained from $\eta_{EL}$ and the ratio of differential photoluminescence, $\Delta P_{PL}$, to photocurrent, $I_{ph}$. Simultaneous measurements of current and differential photoluminescence are readily performed in most OLEDs under steady state reverse bias.

### 3.2.2 Synchronous measurement

Field-induced dissociation of excitons in small molecular weight and polymeric materials typically requires the application of large (>$10^6$ V/cm) electric fields. However, application of large these fields may cause significant charge injection and leakage current in the OLED under study. The reverse bias current thus has two components that must be detected separately, photocurrent, $I_{ph}$ and leakage current, $I_{leak}$. In addition, fluctuations in optical pump intensity may introduce noise into measurements of $\Delta P_{PL}$. Accurate determination of photoluminescent efficiencies requires the detection of the photocurrent component of the total current induced by photoexcitation and reverse bias. The two-tone synchronous measurement technique (Fig. 3.3(b)), isolates the small signal photocurrent component, $i_{ph}$, from leakage current, $i_{leak}$, by locking the total current signal to the optical chopping frequency. In addition, it detects only that portion of $\Delta P_{PL}$ due to electric field modulation. The reverse bias and optical pump intensity are modulated at angular frequencies

$\omega_B$ and $\omega_L$, respectively, and $I_{ph}$ and $\Delta P_{PL}$ are detected at $\omega_L$ and $\omega_B$, respectively. Synchronous detection is employed here to confirm results taken with unmodulated (DC) excitations, and is essential for measuring devices where leakage current may exceed photocurrent, such as for the MEH-PPV OLEDs in this study. Synchronous detection may also be used as a stand alone technique.

The theory of synchronous detection of photoluminescent efficiency is now described. The total small signal current, $i$, is

$$i = i_{ph}(\omega_L, \omega_B) + i_{leak}(\omega_B), \tag{3.7}$$

where $\omega_L$ and $\omega_B$ are the modulation angular frequencies of the photoexcitation and voltage bias, respectively. Since the leakage current is independent of optical excitation, detecting the component of the current at angular frequency $\omega_L$ isolates the photocurrent, i.e.,

$$\frac{1}{T}\int_T i \cos \omega_L t dt = i_{ph} \tag{3.8}$$

where, $T$ is the integration period, $T > 1/\omega_B$, $1/\omega_L$. The photocurrent, $i_{ph}$, is:

$$i_{ph} = \frac{1}{T}\int_T S(\omega_L t) f\left(V(t)\right) \cos \omega_L t dt \tag{3.9}$$

Here, $S(\omega_L t)$ [C/s] is the charge generation rate, assuming complete dissociation of all excitons; it is determined by the photoexcitation intensity and is chopped at angular frequency, $\omega_L$. Also, $f(V)$ is the electric field-induced dissociation probability of an exciton at an applied bias $V$. The voltage bias, and consequently the leakage current, is modulated at angular frequency, $\omega_B$. When $\omega_B \neq \omega_L$,

$$i_{ph} = \frac{\overline{f\left(V(t)\right)}}{T}\int_T S(\omega_L t) \cos \omega_L t dt \,. \tag{3.10}$$

The differential photoluminescence signal also contains two components, $\Delta P_d$, the decrease in luminescence due to exciton dissociation, and $\Delta P_{ex}$, due to random variations in the photoexcitation intensity. Furthermore, $\Delta P_{ex}$ causes random variations, $\delta S$, in the charge generation rate. Assuming that the average photoexcitation intensity is constant, detecting the component of the total photoluminescence, $\Delta P$, at angular frequency $\omega_B$ isolates the differential luminescence due to exciton dissociation, i.e.,

$$\frac{1}{T}\int_T \Delta P \cos\omega_B t dt = \Delta P_d . \tag{3.11}$$

Specifically,

$$\begin{aligned}\Delta P_d &= \frac{1}{T}\int_T \eta_C \eta_{PL} \frac{h\nu}{q}\left[S(\omega_L t) + \delta S(t)\right] f(V(t)) \cos\omega_B t dt \\ &= \eta_C \eta_{PL} \frac{h\nu}{q} \frac{\overline{S(\omega_L t)}}{T} \int_T f(V(t)) \cos\omega_B t dt\end{aligned} . \tag{3.12}$$

Thus PL efficiencies measured using synchronous detection must be multiplied by the synchronous detection factor $g$:

$$\eta_C \eta_{PL} = g\left(\frac{q}{h\nu}\right)\frac{\Delta P_d}{i_{ph}}, \tag{3.13}$$

where $g$ is given by:

$$g = \frac{\int_T S(\omega_L t)\cos\omega_L t dt}{\overline{S(\omega_L t)}} \frac{\overline{f(V(t))}}{\int_T f(V(t))\cos\omega_B t dt} . \tag{3.14}$$

In our experiment, $S$ may be approximated by a square wave with 50% duty cycle. Consequently,

$$\frac{\frac{1}{T}\int_T S(\omega_L t)\cos\omega_L t\,dt}{\overline{S(\omega_L t)}} = \frac{2}{\pi}. \tag{3.15}$$

The function $f$ is approximated by an $N$-th order polynomial,

$$f(V) = \sum_{n=1}^{N} a_n V^n \tag{3.16}$$

with coefficients $a_n$. Using the identity $\int_0^{\pi} \cos^{2n} x\,dx = \frac{(2n)!\pi}{2^{2n}(n!)^2}$ gives:

$$g = \frac{2}{\pi}\left( \frac{\sum_{n=1}^{N} a_n V^n \frac{(2n)!}{2^{2n}[n!]^2}}{2\sum_{n=1}^{N} a_n V^n \frac{(2n+2)!}{2^{2n+2}[(n+1)!]^2} - 1} \right). \tag{3.17}$$

Thus, exact determination of the detection factor, $g$, and hence the out-coupled PL efficiency, $\eta_C\eta_{PL}$, requires the form of the nonlinear function $f(V)$. Ideally, the polynomial coefficients, $a_n$, should be obtained from a Taylor series expansion of experimental measurements of $f$. In Fig. 3.7 below, we show $g$ obtained from experimental data. However, examination of Eq. (3.17) demonstrates the presence of some limits. If $f$ is linearly related to applied voltage, then:

$$g = \frac{2}{\pi}. \tag{3.18}$$

This limit holds in $Alq_3$ above a threshold in the applied electric field. If $f$ is a nonlinear function such that $a_n \neq 0$ for large $n$, then

$$\lim_{V\to\infty} g = \frac{2}{\pi}. \tag{3.19}$$

In general,

$$g = \frac{1}{\pi}(3 \pm 1), \tag{3.20}$$

giving, in the worst case, a 33% error in the determination of $\eta_C \eta_{PL}$.

### 3.2.3 Detection of degradation

We note that charge generation during optical excitation may lead to underestimates of the PL efficiency and corresponding overestimates of $\chi_S$. Exciton dissociation is enhanced when the film is excited at energies significantly above the absorption edge,[60] and consequently, in this work, the optical pump wavelength is selected as close as possible to the HOMO-LUMO gap. Because CT states can also be dissociated into photocurrent under reverse bias, the reverse bias technique may be a sensitive probe for charge generation, providing an inherent guard against underestimating PL efficiency. Indeed, lower, non-linear, $\Delta P_{PL}/I_{ph}$ slopes were measured when higher-energy optical pumps were used.[61] Since knowledge of the outcoupling efficiency is not required in our method, the reverse bias technique offers advantages over conventional, absolute measurements of PL efficiency in determinations of the singlet-triplet formation statistics.

The ability of the reverse bias technique to detect a non-unity branching ratio can be described as follows. From Fig. 3.1, the ideal PL efficiency $\eta_{PL}$ is given by

$$\eta_{PL} = k_R^f \Big/ \left(k_R^f + k_{NR}^f\right). \tag{3.21}$$

The ideal PL efficiency is the upper limit of the EL efficiency and of the measured PL efficiency,

$$\eta_{PL}^{\text{measured}} = b_0 \eta_{PL}, \tag{3.22}$$

where the branching ratio in the absence of an applied electric field $b_0 \leq 1$ is a measure of the efficiency of formation of the relaxed singlet state from the excited singlet state.[60] From Fig. 3.1(a), the branching ratio is[22]

$$b_0 = \frac{\chi_S k_{BS} + k_{S*}}{k_{S*} + k_{BS}}, \tag{3.23}$$

where $\chi_S$ is the fraction of CT states which relax into singlet excitons.

The reverse bias establishes an electric field that dissociates CT states and some singlet excitons into free charge pairs. In contrast with forward bias, where charges are confined by the heterostructure, in reverse bias the charge is swept out of the OLED as photocurrent. Figure 3.2 presents a model for exciton formation and dissociation after optical excitation under reverse bias. The probability of dissociation of a CT state under strong reverse bias is assumed to be unity, and the rate $k_{BS}$ now describes the dissociation of excited singlet states into free charge pairs.[53] The dissociation rate of relaxed singlet excitons under reverse bias is $k_{QS}$. Both the rates $k_{QS}$ and $k_{BS}$ will be dependent on electric field strength.

The photocurrent, $I_{ph}$, from dissociated excitons and CT states under reverse bias can be expressed in terms of the branching ratio as

$$I_{ph} = q\phi\left(b_F \eta_{QS} + 1 - b_F\right), \tag{3.24}$$

where $\phi$ is the incident photon flux, $q$ is the electron charge, $\eta_{QS}$ is the probability of dissociation of a relaxed singlet exciton under reverse bias, and $b_F$ is the branching ratio under a reverse bias electric field. From Fig. 3.2, $\eta_{QS} = k_{QS}/\left(k_R^f + k_{NR}^f + k_{QS}\right)$, and

$$b_F = k_{S*}/\left(k_{S*} + k_{BS}\right). \tag{3.25}$$

The change in PL under application of a reverse bias electric field is then

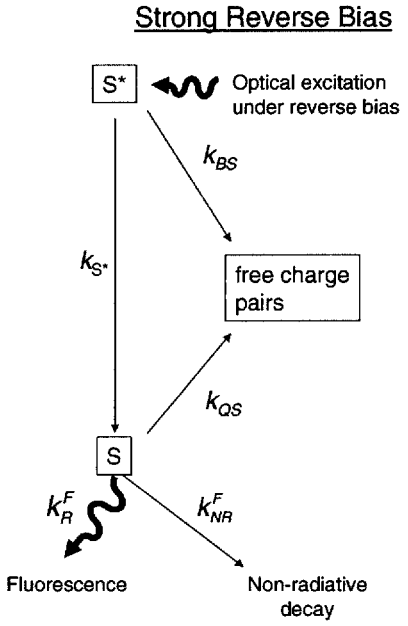


Figure 3.2 –A rate model of exciton formation in the presence of a reverse bias electric field. CT states are assumed to dissociate to charge with unity probability.

$$\Delta PL = PL_0 - PL_F = -h\nu\phi\eta_C\eta_{PL}\left[b_0 - b_F + b_F\eta_{QS}\right], \tag{3.26}$$

where $\eta_C$ is the output coupling efficiency and $h\nu$ is the photon energy. The observed quantity in reverse bias measurements of the PL efficiency is $\Delta PL/I_{ph}$, which is, from Eqns. (3.24) and (3.26),

$$\frac{\Delta PL}{I_{ph}} = -\frac{h\nu}{q}\eta_C\eta_{PL}\left(\frac{b_0 - b_F + b_F\eta_{QS}}{b_F\eta_{QS} + (1 - b_F)}\right). \tag{3.27}$$

The quantity $q/h\nu\left(-\Delta P_{PL}/I_{ph}\right)$ therefore underestimates the out-coupled PL efficiency unless $b_0 = b_F = 1$.

If a CT formation pathway exists (*i.e.* $S^* \rightarrow CT$), the rate of CT formation is expected to increase with electric field, with a corresponding decrease in the branching ratio.

Conversely, an electric-field-independent branching ratio implies there is no pathway $S^* \rightarrow CT$ and hence $b_0 \approx 1$. This is the basis for the capability of the reverse bias technique to detect the presence of CT states. Equation (3.27) shows that an electric field dependence of the branching ratio, $b_F$, must cause an electric field dependence in the measured quantity $\Delta PL/I_{ph}$ and a non-linear reverse bias characteristic. A reverse bias characteristic which is measured to be linear, therefore, requires $b_F$ to be independent of electric field, so that that $b_0 \sim b_F \sim 1$, and, from Eq. (3.27),

$$\eta_C \eta_{PL} = q/h\nu\left(-\Delta P_{PL}/I_{ph}\right). \tag{3.28}$$

This limit applies to many polymers excited at their absorption edge. The data presented below on MEH-PPV spin statistics is in this limit.

Note that a non-linear reverse bias characteristic $\Delta PL/I_{ph}$ does not itself require $b_0 < 1$. A reverse bias characteristic that is only non-linear at high pump energies, however, strongly suggests the formation of CT states and $b_0 < 1$. Such a characteristic is presented in Fig. 3.13, discussed in Section 3.6.

## 3.3. Experimental Technique

To compare the EL and PL efficiencies in small molecular weight and polymeric materials, two types of OLEDs were fabricated. Polymeric OLEDs used an emissive and hole-transporting layer (HTL) layer of the polymer MEH-PPV,[62] and small molecular weight materials were studied using an emissive layer of $Alq_3$. All devices were fabricated on cleaned and UV-ozone treated glass substrates precoated with an indium tin oxide (ITO) anode with a sheet resistance of ~ 20 Ω/sq. To enhance hole injection from the anode, all devices used a

thin layer of poly(3,4-ethylenedioxythiophene):poly(4-styrenesulphonate) (PEDOT:PSS). This layer was prepared by spin coating onto the ITO substrate followed by baking at T ~ 120 °C for at least 30 minutes in an oxygen-free environment. The polymer OLEDs had an approximately 300-Å-thick layer of MEH-PPV spun cast onto the PEDOT:PSS layer from 3:7 tetrahydrofuran-toluene solvent, and baked in an oxygen-free environment at T ~ 115 °C for at least 10 hours. The $Alq_3$ OLEDs had a 500-Å-thick HTL composed of *N,N'*-diphenyl-*N,N'*-bis(3-methylphenyl)-[1,1'-biphenyl]-4,4'-diamine (TPD) deposited onto the PEDOT:PSS layer, followed by a 200-Å-thick light-emitting layer of $Alq_3$. The TPD and $Alq_3$ layers were deposited by high-vacuum ($10^{-6}$ Torr) thermal evaporation, as were all layers comprised of small molecules. Both types of devices contained an electron transport layer (ETL) of 2,9-dimethyl-4,7-diphenyl-1,10-phenanthroline (BCP), chosen because of its transparency to the optical pump beams at $\lambda = 405$ nm and at $\lambda = 532$ nm, and its efficient hole and exciton-blocking capability.[50] The thickness of the BCP layer was 500 Å in $Alq_3$ devices, and for reasons described in Sec. IV, 150 Å in the MEH-PPV devices. A shadow mask with 1 mm-diameter openings was used to define the cathode in all devices. The cathodes consisted of a layer of approximately 60:1 Mg:Ag followed by a Ag cap to protect against oxidation. $Alq_3$ devices had a 1000 Å-thick Mg:Ag layer and a 200 Å-thick Ag cap, whereas MEH-PPV devices had a 500 Å-thick Mg:Ag layer followed by a 500 Å-thick Ag cap.

The experimental setups for the DC and synchronous PL efficiency measurements are shown in Figs. 3.3(a) and 3.3(b), respectively. Two diode lasers were employed as optical sources, one with wavelength $\lambda = 405$ nm and another at $\lambda = 532$ nm. The lasers had continuous maximum output powers of 3.4 mW and 25 mW, respectively. A lens was used to

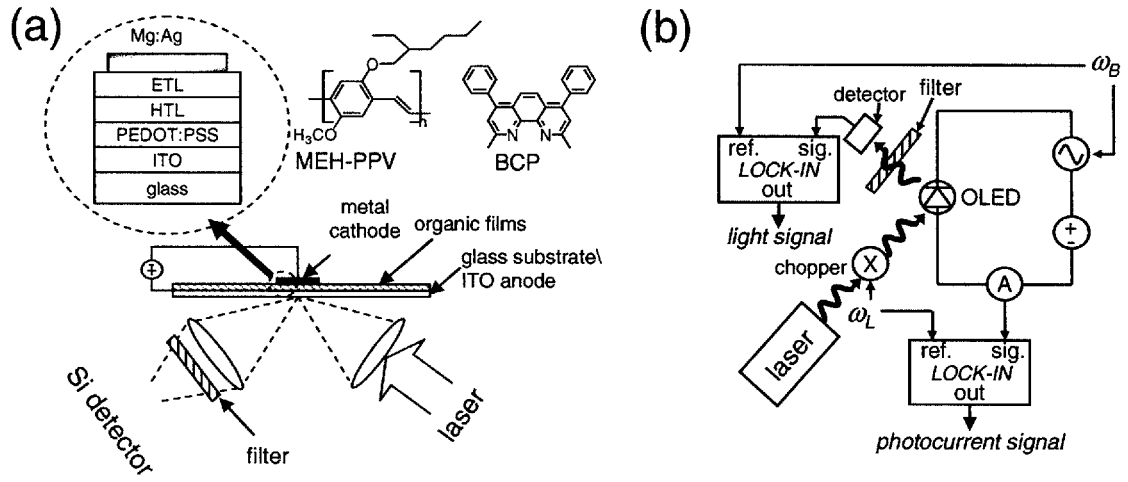


Figure 3.3 - (a) The experimental setup of the DC PL efficiency measurement. PL from an optically-excited OLED is focused onto a calibrated silicon detector. An optical filter is used to remove the pump light from the collected light. The OLED is placed under a varying reverse bias that partially quenches the PL. The out-coupled PL efficiency is obtained by comparing the change in PL ($\Delta P_{PL}$) to the photocurrent. Inset. A cross section of the OLEDs: charges and excitons within the organic layer under test are confined by a heterostructure employing bathocuproine (BCP) as the electron transport (ETL) and hole blocking layer. The semiconducting polymer MEH-PPV was used as a hole transport layer (HTL). (b) The experimental setup of the synchronous PL efficiency measurement. Here the photocurrent and out-coupled PL are detected by locking the photocurrent to the optical chopping frequency, and the PL to the modulation frequency of the reverse bias voltage. This scheme rejects leakage current, optical pump fluctuation and detected light noise.

focus the pump laser to an approximately 1-mm diameter spot, aligned with the OLED cathode. Fluorescence was collected by a second lens, and was optically filtered to remove the

pump wavelength before being focused onto a silicon detector. The collection optics were calibrated by comparing the EL efficiency in this geometry to that measured by placing the OLED directly onto the surface of a large-area silicon detector.[56] Although this did not affect measurement of the singlet fraction, measurement of the total light emitted in the forward direction enables calculation of the out-coupling efficiency, $\eta_C$. In the two-tone synchronous measurement setup shown in Fig. 3.3(b), the laser light was mechanically chopped at angular frequency $\omega_L = 2\pi \cdot 390$ rad/s, yielding an approximately 50% duty cycle square wave. The reverse bias was modulated sinusoidally at angular frequency $\omega_B = 2\pi \cdot 510$ rad/s. Photocurrent and differential PL were detected using two lock-in amplifiers. Each measurement at a specific reverse bias voltage was averaged for 30s. Except for low temperature measurements, which were performed under vacuum, all devices were measured in air.

## 3.4. Photoluminescence Efficiency Measurements

Figure 3.4(a) shows the reverse bias photocurrent, $I_{ph}$, and the magnitude of the electric field-induced change in PL, $\Delta P_{PL}$, in an $Alq_3$-OLED measured using the DC technique. All $Alq_3$ devices were excited at $\lambda = 405$ nm, the edge of the absorption band of $Alq_3$. The resultant out-coupled PL efficiency is shown in Fig. 3.4(b). A weighted sum of several measurements yields $\eta_C \eta_{PL} = (5.9 \pm 0.1)\%$ for $Alq_3$ in Eq. (3.28). At zero reverse bias, the devices exhibit weak photovoltaic action leading to a slight offset in the photocurrent that does not affect the PL efficiency measurement. The PL efficiency of $Alq_3$ has been previously measured to be $\eta_{PL} = (27 \pm 5)\%$,[63,64] yielding an out-coupling fraction of $\eta_C = (24 \pm 4)\%$.

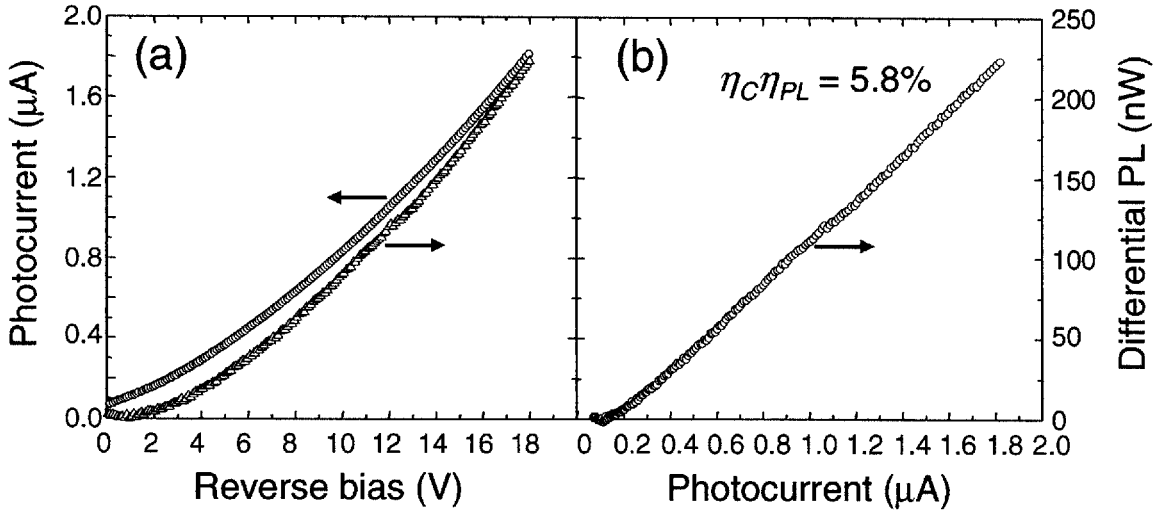


Figure 3.4 – (a) Magnitude of change in PL, $\Delta P_{PL}$, and the corresponding photocurrent, $I_{ph}$, in Alq3 as a function of reverse bias. (b) The relation between $\Delta P_{PL}$ and $I_{ph}$, given by Eq. (3.5), gives the out-coupled PL efficiency, $\eta_C\eta_{PL}$.

Due to weak microcavity effects, $\eta_C$ is expected to be dependent on the position of the luminescent region within the device structure.[65] The PL efficiency of $Alq_3$ measured using the DC technique was confirmed with a synchronous measurement.

Similarly, DC measurements of $I_{ph}$ and $\Delta P_{PL}$ in MEH-PPV are shown in Fig. 3.5(a) for optical excitation at the absorption edge of MEH-PPV, at $\lambda = 532$ nm. The resultant out-coupled PL efficiency is shown in Fig. 3.5(b). Using Eq. (3.5), the slope of the linear regime at small $I_{ph}$ yields $\eta_C\eta_{PL} = (4.8\pm0.1)\%$ for MEH-PPV. The PL efficiency of MEH-PPV was previously measured[66] to be $\eta_{PL} = 10-15\%$, yielding an out-coupling fraction of $\eta_C = 31 - 49\%$.

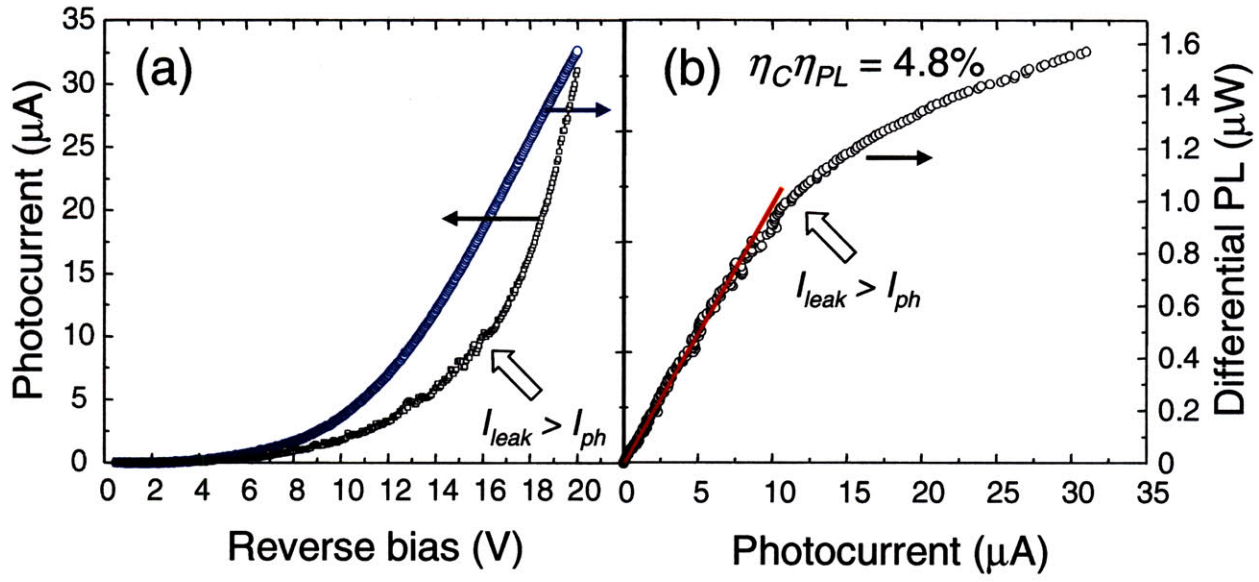


Figure 3.5 - (a) Magnitude of change in PL, $\Delta P_{PL}$, and the corresponding photocurrent $I_{ph}$ in MEH-PPV as a function of reverse bias. The "kink" in the photocurrent at $V \sim 16$V corresponds to the voltage at which leakage current begins to dominate photocurrent. (b) The relation between $\Delta P_{PL}$ and $I_{ph}$, given by Eq. (3.5), gives the out-coupled PL efficiency, $\eta_C\eta_{PL}$.

We note that this is consistent with reports that solution processing of polymers may preferentially align radiative dipoles within the polymeric chains parallel to the reflective cathode, enhancing the out-coupling fraction relative to that of randomly oriented vacuum-deposited small molecular weight materials.[53]

The kink in the photocurrent characteristic in Fig. 3.5(a) (marked by the arrow) denotes the boundary between regions of markedly different noise behavior, and corresponds to the photocurrent at which the PL characteristic in Fig. 3.5(b) becomes non-linear. These effects are interpreted to be the result of the reverse bias current being dominated by $I_{ph}$ below

the kink, and $I_{leak}$ above it. Reverse bias leakage currents in MEH-PPV OLEDs were often comparable to photocurrents and were unstable and inconsistent in repeated measurements. Consequently, synchronous detection was required to confirm MEH-PPV PL efficiencies measured using the DC technique.

Synchronous measurements of $I_{ph}$ and $\Delta P_{PL}$, are shown in Fig. 3.6(a) for MEH-PPV, again for an excitation wavelength of $\lambda = 532$ nm. The out-coupled PL efficiency is $\eta_C \eta_{PL} = (4.8 \pm 0.2)\%$, in agreement with the DC result; see Fig. 3.5(b). Data points and error bars (both vertical and horizontal) represent the mean and standard deviation, respectively, of data collected at each reverse bias voltage. The linearity of the characteristic of Fig. 3.6(b) is especially notable, since both DC and synchronous measurements employ reverse bias voltages of up to 20V. Thus, the synchronous technique provides strong evidence that the discontinuity in slope observed in the DC PL measurement of Fig. 3.5(b) is due to leakage current. The calculation of the *g*-factor (Eq. (3.17)) by fitting to the DC and synchronous data for MEH-PPV is shown in Fig. 3.7.

Synchronous detection showed a negligible dependence on bias frequency. The phase of the $\Delta P_{PL}$ signal with respect to the voltage modulation changes rapidly at low photocurrent, from approximately -180° to zero degrees. At low reverse bias then, $\Delta P_{PL}$ is *positive*, becoming negative at higher voltages. The increase in PL for low reverse bias is due to a reduction in singlet-polaron annihilation as photogenerated charge is detrapped by the electric field. At sufficiently high reverse bias, these charges are rapidly removed, and the increase in PL is overwhelmed by the electric field-induced dissociation of excitons.

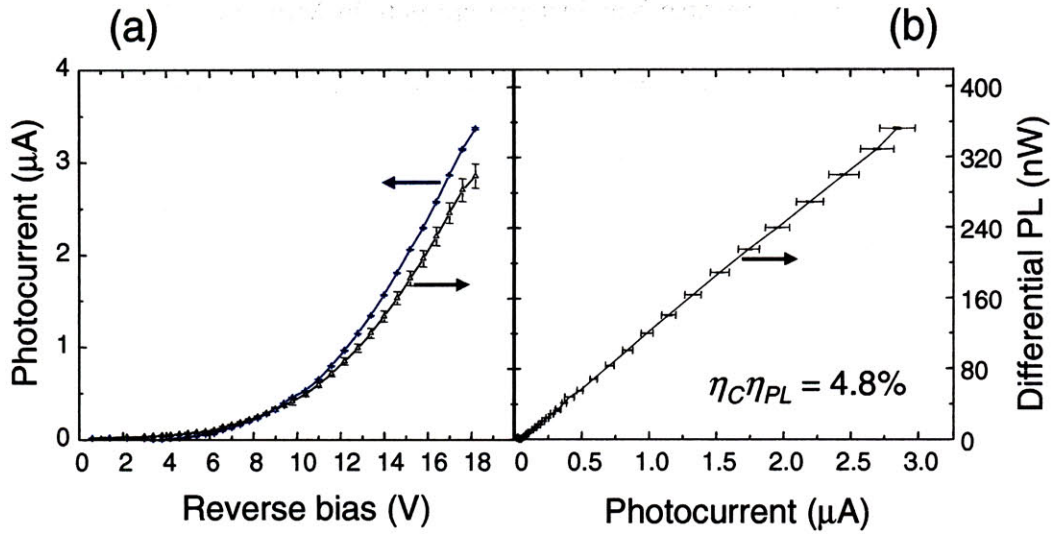


Figure 3.6 - (a) Synchronously-detected $\Delta P_{PL}$ magnitude and the corresponding photocurrent $I_{ph}$ in MEH-PPV as a function of reverse bias. (b) The relationship between $\Delta P_{PL}$ and $I_{ph}$, in Eq. (3.5), gives the synchronously-detected out-coupled PL efficiency, .

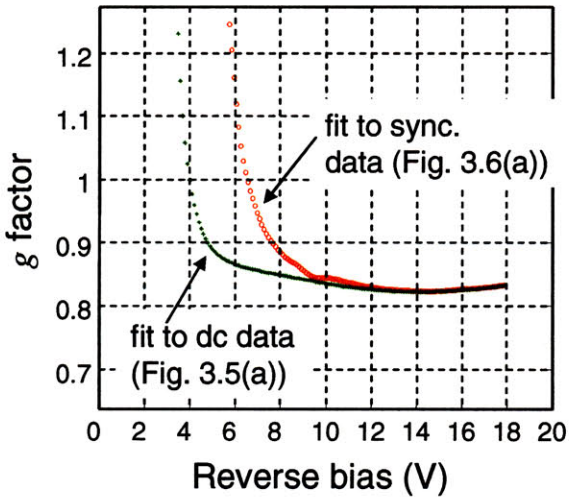


Figure 3.7 - Numerical evaluations of Eq. (3.14), using fits to experimental data for the electric field-induced dissociation probability, *f*. These curves are used to determine the synchronous detection factor, *g*, in MEH-PPV. It is observed that both DC and synchronously-detected measurements of *f* yield the same values of *g* at large values of reverse bias. A value of $g = 0.82 \pm 0.03$ is then calculated from data in Figs. 3.5(a) and 3.6(a).

The effect of detrapping at low electric fields is more pronounced in the optical pump intensity dependence data shown in Fig. 3.8. There is no observed dependence in the slope of $\Delta P_{PL}$ versus $I_{ph}$ above the zero-crossing, consistent with $\eta_{PL}$ independent of pump intensity. But the zero-crossing is observed to shift in proportion to the pump intensity, confirming that increases in $\Delta P_{PL}$ at low bias (and hence low current) are due to reductions in the density of photogenerated charge.

Reverse bias measurements of the PL efficiency require complete collection of the photocurrent from dissociated excitons. Thus, the OLED structure must be tailored to facilitate charge extraction. It was observed that the reverse bias $\Delta P_{PL}$ versus $I_{ph}$ characteristics of MEH-PPV were non-linear when thick films of BCP ( $d > 150$ Å ) were used, most probably due to an energy barrier to electron transport across the MEH-PPV/BCP interface.[67,68] It has been proposed that thin BCP layers, although observed to efficiently block hole transport, assist in the extraction of electrons due to gap states in the material formed during deposition of the cathode that penetrate as far as ~ 200Å from the cathode interface.[69] Indeed, highly efficient photovoltaic devices have been fabricated by using this method of charge extraction from the relatively deep lowest unoccupied molecular orbital of $C_{60}$ at 4.6 eV.[69] With a 150Å-thick BCP ETL, the yield of useful MEH-PPV devices (i.e. devices with linear reverse bias characteristics) is close to 100%.

Accurate measurements of the PL efficiency also require that the technique be immune to the effects of geminate and non-geminate recombination involving charge from dissociated excitons, which may limit the extraction of photocurrent. The electric-field dependence of exciton dissociation under reverse bias is broadly consistent with the Onsager model.[1,58,59]

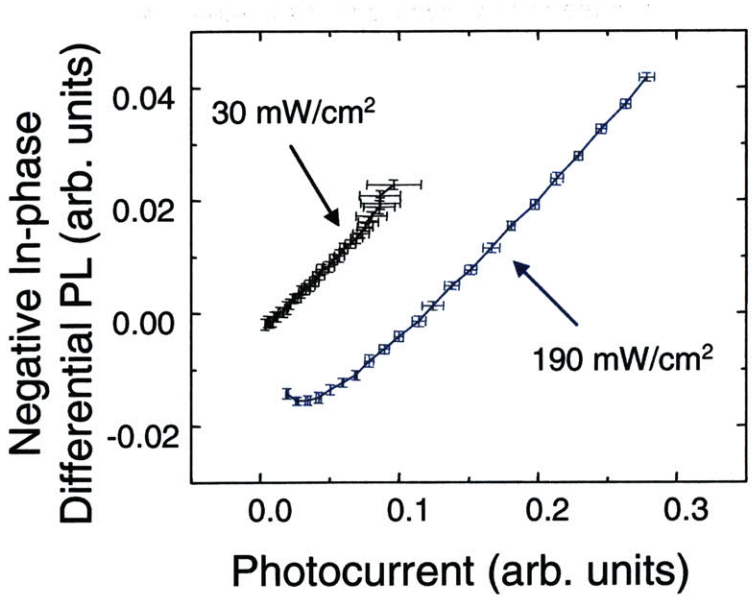


Figure 3.8 - The synchronously-detected PL efficiency of Alq3 is approximately independent of the optical pump intensity. The offset in $\Delta P_{PL}$ is due to increased charge generation within the film introduced by the higher intensity optical pump. To make clear the initial increase in $\Delta P_{PL}$, the component of $\Delta P_{PL}$ in phase with the reverse bias modulation is plotted here.

However, due to the large electrostatic forces between geminate charges immediately following exciton dissociation, many geminate charge carriers will recombine before they can be extracted.[1] Use of the reverse bias technique requires that charges from singlet excitons dissociated by the applied electric field do not subsequently form non-emissive triplet excited states. The absence of an electric field dependence of PL efficiency in reverse bias measurements demonstrates that geminate recombination occurs at times shorter than the spin dephasing time. The reverse bias technique is also observed to be unaffected by non-geminate recombination. Given a typical carrier mobility of $> 10^{-5}$ cm$^2$/Vs, the density of minority carriers under reverse bias in both $Alq_3$ and MEH-PPV is small, $n < 10^{15}$ cm$^{-3}$. Low charge

carrier densities, and the high electric fields required to dissociate excitons and separate the resulting geminate charges, reduce the probability of non-geminate recombination, which increases with $n^2$. But most significantly, synchronous measurements demonstrate that the reverse bias PL efficiency is independent of leakage currents that frequently exceed 10 mA/cm$^2$, confirming the absence of non-geminate recombination in these devices.

## 3.5. Electroluminescence Efficiency Measurements and Singlet Fractions

The EL quantum efficiencies of the $Alq_3$ and MEH-PPV OLEDs are shown in Fig. 3.9. When divided by the outcoupled PL efficiency, the EL efficiencies give an upper-bound estimate for the singlet fraction $\chi_S\gamma$ from Eq. (3.6) $\chi_S\gamma = (18.0\pm0.3)\%$ for $Alq_3$ and $\chi_S\gamma = (17.0\pm0.7)\%$ for MEH-PPV. The EL-specific loss, $\gamma$, is thus required to obtain the singlet fraction, $\chi_S$. We summarize several loss mechanisms and present a model for losses due to traps in both systems. EL-specific losses may be due to:

(a) Electron and hole currents may be unbalanced. This is considered unlikely in heterostructure devices because the currents are forcibly equalized using blocking layers such as BCP.[50] Figure 3.9 shows the current versus voltage (*I-V*) characteristics of both $Alq_3$ and MEH-PPV devices compared to a device consisting of only an 800Å-thick BCP transport layer, sandwiched between PEDOT:PSS and a Mg:Ag cathode. Since BCP effectively blocks hole injection,[50] the similarity of the slopes of each of the characteristics for $V > 3$V demonstrates that charge transport in each device is limited by electron injection.[70] At the onset of exciton formation in $Alq_3$ and MEH-PPV, the OLEDs deviate from the BCP electron-only characteristic and demonstrate recombination-limited *I-V* characteristics, a clear indication of near unity charge balance in both heterostructure OLEDs.

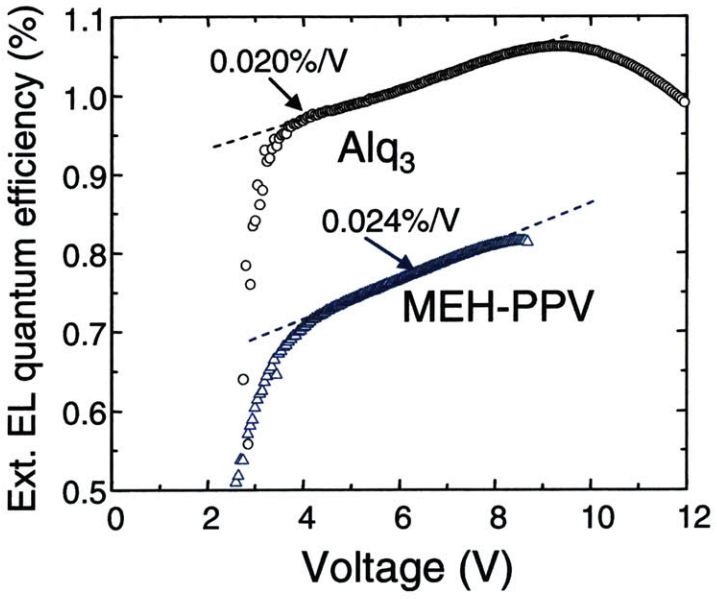


Figure 3.9 - The electroluminescent (EL) quantum efficiencies of an $Alq_3$ and an MEH-PPV OLEDs as functions of voltage, peaking at 1.06% and 0.81% respectively. The linear dependence of the EL efficiency on voltage is consistent with the charge trap model described in Eq. (3.30).

(b) Microcavity effects[65,71] may affect PL and EL differently if the EL recombination zone is significantly narrower than the luminescent layer thickness. However, charges are confined within thin luminescent layers in this experiment, and hence microcavity effects are not expected to influence the results. To confirm this, devices were also fabricated with 250Å-thick BCP layers, but no significant change in the singlet fraction, $\chi_S$, was observed.

(c) There may be significant polaron or field-induced quenching of singlet excitons, causing the EL quantum efficiency to decrease with increasing current density. The effects of such high-density phenomena may be minimized by extrapolating the quantum efficiency to its limit at low current.[36,72]

(d) EL-specific losses may occur if electroluminescent excitons form preferentially at certain molecular sites such as charge traps.[50,73] There is no preference for exciton formation at these sites under photoexcitation. The luminescent efficiency of trap sites may be much lower than the average efficiency of excited molecules in the bulk film, especially if the traps are due to contamination. This process may result in an EL quantum efficiency, $\eta_{EL}$, that increases with applied voltage, $V$, and with temperature, $T$, since the traps can be saturated with charge, and charge detrapping is thermally activated. As evidence of the presence of low-luminescent-efficiency traps, it is noted that $\eta_{EL}$ in guest-host films does not increase with $V$ when the guest molecules act as *emissive* traps.[36,74,75] Instead, luminescent efficiencies of guest-host films typically decrease monotonically with increasing $V$ due to exciton quenching by charges, while the efficiencies of neat luminescent materials usually peak with increasing excitation strength.[36,76]

Examination of the voltage and temperature dependencies of the EL efficiencies in Figs. 3.8 and 3.10, respectively, confirms the presence of EL-specific losses in both $Alq_3$- and MEH-PPV-based OLEDs, i.e. $\gamma < 1$. We propose a simple model for traps that determines $\gamma$ by extrapolating $\eta_{EL}$ to its high current density limit. To explain the voltage and temperature dependencies of EL efficiency, we assume that each injected charge is either trapped, in which case it luminesces with quantum efficiency $\eta_t$, or it remains mobile and ultimately forms an exciton that luminesces with quantum efficiency $\eta_f$. We further assume that $\eta_f > \eta_t$. From simple Fermi statistics, the probability of charge trapping is taken to be proportional to the fraction of trap sites remaining unfilled at

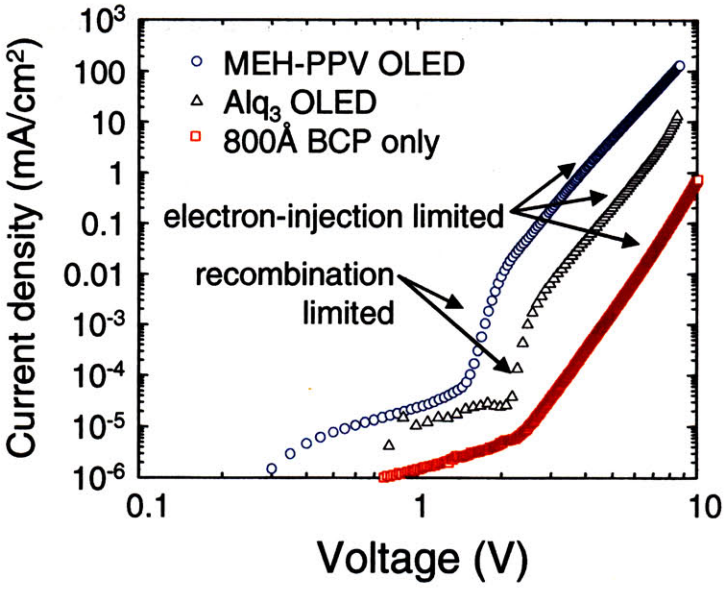


Figure 3.10 - The current-voltage (I-V) characteristics of an MEH-PPV and an Alq3 OLED compared to electron-only transport in an 800Å-thick film of BCP. At high biases, all devices are limited by electron injection into the BCP, but at voltages below the onset of exciton formation in the OLEDs, the current density drops sharply, demonstrating that the OLED heterostructure forces unity charge balance in electroluminescence.

voltage $V$, i.e. ( 1 - $V/V_{sat}$), where $V_{sat}$ is defined as the voltage at which all the trap sites are saturated with space charge. Thus, $\eta_{EL}$ is given by:

$$\eta_{EL} = \eta_f \frac{V}{V_{sat}} + \eta_t \left(1 - \frac{V}{V_{sat}}\right), \qquad V < V_{sat}$$
$$\eta_{EL} = \eta_f, \qquad V > V_{sat}. \tag{3.29}$$

At $V_{sat}$, EL specific losses due to traps vanish and $\gamma = 1$, $\eta = \eta_f$. If $V_{sat}$ is known, the linear dependence of $\eta_{EL}$ on $V$ can be extrapolated to determine $\eta_f$, the EL efficiency in the absence of EL specific losses, and hence the singlet fraction, $\chi_S$.

A worst-case value for $V_{sat}$ can be calculated by recognizing that if a single trap site is present inside the radius of diffusion of an optically-excited exciton, the exciton would diffuse to that trap site, eliminating any possible difference between EL and PL. This places an upper bound on trap density. The maximum area charge density necessary to fill all trap sites in the recombination zone is then:

$$\sigma_{\max} = t_{lum} \Big/ \frac{4\pi}{3} L_D^{\,3} \tag{3.30}$$

where $t_{lum}$ is the thickness of the luminescent layer and $L_D$ is the exciton diffusion length. Then using Q = CV gives the worst-case value of:

$$V_{sat} = q\sigma_{\max} \Big/ \varepsilon \left( t_{BCP} + \frac{t_{lum}}{2} \right) \tag{3.31}$$

where $t_{BCP}$ is the thickness of the BCP layer and ε is the average of the dielectric constants of BCP and the luminescent material. Using $L_D$ = 40 Å (typical for Förster transfer)[77] and the slopes $d\eta_{EL}/dV$ calculated in Fig. 3.9 in Eq. (7), we find the worst-case $V_{sat}$ = 27 V for $Alq_3$ and 20 V for MEH-PPV, corresponding to maximum values for $\eta_f$ of 1.4% and 1.1%, respectively. This yields minimum values for γ of 0.76 and 0.74, leading to a maximum value of $\chi_S = (24 \pm 0.4)\%$ for $Alq_3$ and $\chi_S = (23 \pm 1)\%$ for MEH-PPV.

A direct experimental estimate of $V_{sat}$ in $Alq_3$ can be obtained from Fig. 3.11 by extrapolating the EL efficiencies of $Alq_3$ to find the voltage at which the temperature dependence vanishes. The point at which the linear slopes of each temperature characteristic intersect in Fig. 3.11 is $V_{sat} = (15.1 \pm 1)$ V, which gives $\eta_f = 1.19\%$, and $\chi_S = (20 \pm 1)\%$ in $Alq_3$. The linearity of $\eta_{EL}$ with voltage, its temperature dependence, and the intersection at $V_{sat}$,

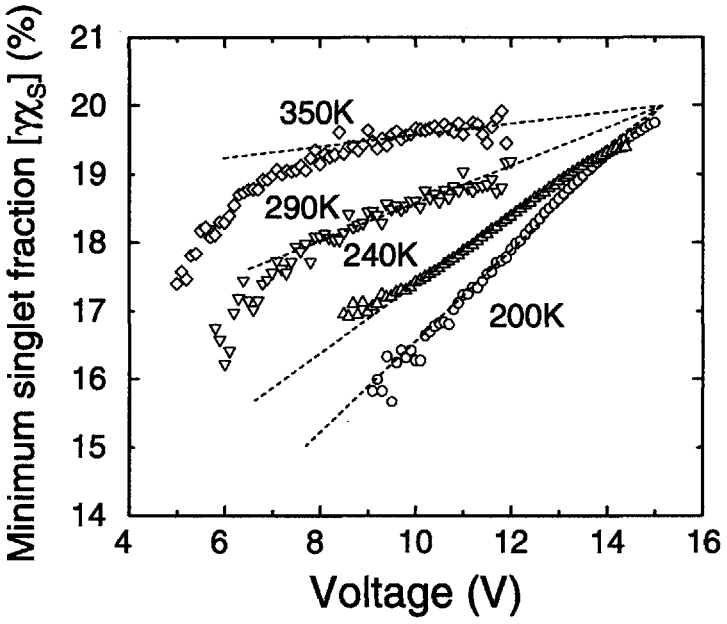


Figure 3.11 - The temperature dependence of the quantum efficiency of Alq3 shows a significant increase in the slope of efficiency versus voltage as temperature decreases. This is attributed to exciton formation in trap states, resulting in EL-specific losses. The point at which the linear extrapolations intersect is $V_{sat}$.

which is consistent with trap saturation, all strongly support the model of exciton formation described by Eq. (3.29).

Figure 3.11 shows that when measured at a sufficiently high current density such that $V$ approaches $V_{sat}$ ( i.e. $J = 100\,\mathrm{mA/cm^2}$ ), $\eta_{EL}$ approximately tracks $\eta_{PL}$ over a large temperature range, indicating that $d(\gamma\chi_S)/dT = 0$ and $\gamma \sim 1$ for both $Alq_3$ and MEH-PPV. The singlet fractions for $\gamma = 1$ are shown in the insets as functions of temperature.

Finally, it is noted that even in the worst case, EL specific losses contribute only a small correction to the measured value of the singlet fraction $\chi_S$, and in both $Alq_3$ and MEH-

PPV, $\chi_S \leq 25\%$. The best estimate for $\chi_S$ in $Alq_3$ uses $V_{sat}$ derived from Fig. 3.11, and is $\chi_S = (20\pm1)\%$. Similarly, the best estimate for $\chi_S$ in MEH-PPV lies between the measured and worst-case values, i.e. $\chi_S = (20\pm4)\%$.

## 3.6. CT state formation detection

Figure 3.12 shows the OLED device structure and two reverse bias characteristics measured in air using two different optical pumps on two different devices, immediately after each had been fabricated. One optical pump was a laser of intensity ~3 W/cm$^2$ tuned to the absorption edge of MEH-PPV at wavelength $\lambda$ = 532 nm, and the second was a laser with wavelength $\lambda$ = 405 nm and intensity ~0.4 W/cm$^2$. The two traces of the $\lambda$ = 405 nm characteristic represent an upwards sweep in voltage (solid line) followed by a downwards sweep (dashed line), and their similarity indicates that the nonlinearity of the $\lambda$ = 405 nm characteristic is not due to degradation of the OLED over the course of the measurement. The nonlinearity is also not a result of leakage current, since two-tone synchronous detection rejects any leakage current component in the detected photocurrent.[22] Applying Eq. (3.28), the out-coupled PL efficiency measured using the $\lambda$ = 405 nm pump is $\eta_C\eta_{PL} < 1.8\%$. On the other hand, the $\lambda$ = 532 nm characteristic is linear and produces an out-coupled PL efficiency of $\eta_C\eta_{PL} = 4.8\%$. The initial increase in PL when pumped at $\lambda$ = 405 nm results from the de-trapping of photo-generated charge by the reverse bias field. This reduces singlet-polaron annihilation[1] at low bias but this effect is overwhelmed by singlet exciton dissociation at higher bias.[22]

The pump wavelength dependence of the PL efficiency measurements in Fig. 3.13 is consistent with the detection of CT states by the reverse bias technique. The higher-energy

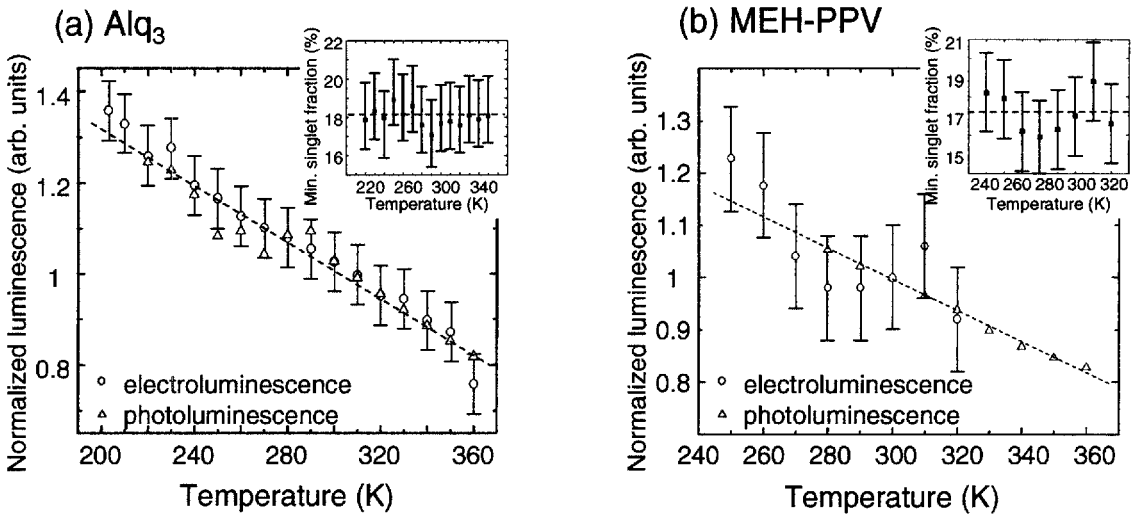


Figure 3.12 - (a) Photoluminescence (PL) and peak electroluminescence (EL) quantum efficiencies as functions of temperature in Alq3. (b) The PL and peak EL quantum efficiencies as functions of temperature in MEH-PPV. In both Alq3 and MEH-PPV, EL measured at large current densities ($J \approx 100$ mA/cm$^2$) tracks PL, demonstrating that the minimum singlet value is independent of temperature over the temperature range studied. Because $d(\gamma\chi_S)/dT \sim 0$, it is concluded that $\gamma \approx 1$. Insets: Inferred singlet fractions for Alq3 and MEH-PPV.

pump excites CT states via higher-energy singlet exciton states, S*, causing a non-linear characteristic and a reduced PL efficiency as discussed above. The lower-energy pump excites singlets close to the absorption edge of MEH-PPV, presumably below the energy of the CT manifold in MEH-PPV, reducing the likelihood of CT state formation. From Eq. (3.22), then, the $\lambda$ = 532 nm characteristic more accurately measures the ideal PL efficiency $\eta_{PL}$. The wavelength dependence of the data in Fig. 3.13 is also observed in photoexcitation spectra of degraded PPVs.[60]

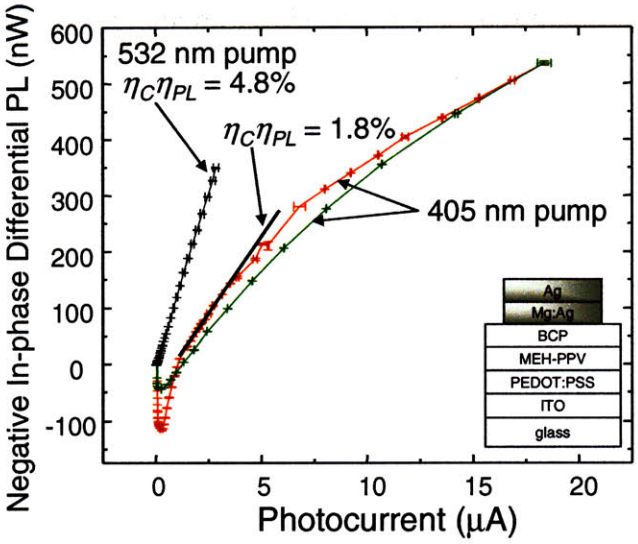


Figure 3.13 – Differential photoluminescence $\Delta PL$ versus photocurrent characteristics for MEH-PPV at two different pump wavelengths. The component of $-\Delta PL$ in phase with the reverse bias voltage modulation is plotted. The non-linearity and low efficiency of the $\lambda = 405$ nm characteristic are an indication of the formation of CT states, and are not due to degradation, as indicated by the similarity of the up (red) and down (green) sweeps. The $\lambda =$ 405 nm efficiency is taken from the slope of the data as shown.

## 3.7. Discussion

Table 1 summarizes six experimental studies, including this work, of $\chi_S$ in small molecular and polymeric organic materials. The methods employed vary – Cao, *et al.*,[52] and Kim, *et al.*,[53] both employ absolute measurements of EL and PL efficiencies, while Wilson, *et al.*,[54] and our work use relative comparisons. Four independent measurements find $\chi_S \leq 0.25$ in molecular organic materials, but in previous work, $\chi_S$ in conjugated polymers was generally found to exceed 0.25. In addition to the methods reported in Table 1, there are several

measurements of of $\chi_S$ that employ photoinduced absorption to calculate triplet densities.[78,79] Several of these measurements have also found $\chi_S > 0.25$.[79]

High values of $\chi_S$ can possibly be interpreted in terms of the photophysical rates of Fig. 3.1. Tandon *et al.*[31] review theoretical estimates of $k_{Sm}$ and $k_{Tm}$. They model these rates in polymers using parallel interacting chains and argue that electron correlations between delocalized states may account for $\chi_S > 0.25$.

The discrepancy between the present work and previous polymeric measurements that yield $\chi_S > 0.25$ demands attention. We now discuss these and the current measurements, together with the electron paramagnetic resonance (EPR) experiments of Wohlgenannt, *et al.*,[28,80] and Shinar, and coworkers.[81,82] While all measurements of $\chi_S > 0.25$ require $k_{Sm} > k_{Tm}$, EPR experiments may provide a more direct probe of these rates.

### 3.7.1 Measurements of $\chi_s$ in small molecular materials

To maximize the OLED efficiency, it is desirable to harness all injected charges, either by developing systems with $\chi_S \rightarrow 1$ or by also using phosphorescence from triplet states. Perhaps the first measurements of $\chi_S$ in an organic semiconductor used fluorescent and phosphorescent guest molecules to capture singlet and triplet excitons formed in an $Alq_3$ host.[36,50] The singlet ratio was estimated by identifying singlets by fluorescence and triplets by phosphorescence. Their ratio gave $\chi_S = (22\pm3)\%$ consistent with the current study.[50]

**Table 1. Summary of various measurements of $\chi_S$ using EL/PL comparisons.**

**(a) Small molecular weight materials**

**(i) Direct comparisons of EL to PL**

| Material | $\eta_c\eta_{PL}(\%)$ | $\eta_{EL}(\%)$ | $\gamma$ | $\chi_s$ | Ref. |
|---|---|---|---|---|---|
| $Alq_3$ [a)] | 5.8 | 1.06 | 0.91±0.05 | 0.20±0.01 | - |

**(ii) Phosphorescent techniques**

| Material | $\eta_{PL}^f/\eta_{PL}^p$ | $\eta_{EL}^f/\eta_{EL}^p$ | $\chi_s$ | Ref. |
|---|---|---|---|---|
| Pt-monomer[b)] | 4.8 | 1.0 | 0.22±0.01 | 54 |
| CBP [c)] | - | 0.22 | 0.22±0.02 | 41,74 |
| $Alq_3$ [d)] | 2.7 | 0.56 | 0.22±0.03 | 50 |

Notes:

a. This work.
b. The Pt-polymer in (b) and monomer are related. See Ref. [54] for chemical structures. The singlet fraction is determined from the ratios of fluorescent and phosphorescent efficiencies; see Eq. (3.32).
c. Only the more accurate measurement in Ref. [74] has been quoted; see text. Electroluminescent efficiencies are quoted at $J = 1$ mA/cm$^2$.
d. Fluorescent and phosphorescent efficiencies were obtained using fluorescent and phosphorescent guest molecules in an $Alq_3$ host.

**(b) Polymeric materials**

**(i) Direct comparisons of EL to PL**

| Material | $\eta_{PL}(\%)$ | $\eta_c\eta_{PL}(\%)$ | $\eta_{EL}(\%)$ | $\eta_{EL}/\eta_c(\%)$ | $\gamma$ | $\chi_s$ | Ref. |
|---|---|---|---|---|---|---|---|
| OC1C10-PPV[a)] | - | 8.5 | 4 | - | - | > 0.50 | [52] |
| MEH-PPV[b)] | - | 8.5 | 1.3 | - | - | > 0.15 | [52] |
| Green PPV[c)] | 33±3 | - | 6±0.5 | 23 | - | > 0.35-0.45 | [53] |
| Orange PPV[d)] | 9±1 | - | 1.8±0.2 | 5.6 | - | > 0.35-0.45 | [53] |
| MEH-PPV [e)] | - | 4.8 | 0.82 | - | 0.85±0.15 | 0.20±0.04 | - |

**(ii) Phosphorescent techniques**

| Material | $\eta_{PL}^f/\eta_{PL}^p$ | $\eta_{EL}^f/\eta_{EL}^p$ | $\chi_s$ | Ref. |
|---|---|---|---|---|
| Pt-polymer[f)] | 4.6 | 1.8 | 0.57±0.04 | [54] |

Notes:

a. OC1C10-PPV is [poly(2-(3,7-dimethyloctyloxy)-5-(2'methoxy-1,4-phenylene vinylene). It was blended with 20% (2-(4-biphenyl)-5-(4-tert-butylphenyl)1,3,4-oxidiazole (Bu-PBD).
b. MEH-PPV is poly[2-methoxy-5-(2-ethylhexyloxy)-1,4-phenylenevinylene]
c. 2-alkoxyphenyl-PPV-co-2,5-dialkoxy-PPV
d. 2,5-dialkoxy-PPV
e. This work.
f. The Pt-polymer and monomer in (a) are related. See Ref. [54] for chemical structures. The singlet fraction is determined from the ratios of fluorescent and phosphorescent efficiencies; see Eq. (3.32). The singlet fraction $\chi_S = 0.57\pm0.04$ is obtained by averaging the results at different temperatures, not simply the room temperature values of $\eta_{PL}^f/\eta_{PL}^p$ and $\eta_{EL}^f/\eta_{EL}^p$ given above.

Subsequent refinements used phosphor-sensitized fluorescence, a technique that employs a fluorescent guest material mixed into a host.[41] To harness triplet excitons formed in the host, an additional sensitizing phosphorescent species is added to transfer triplet excitons to the singlet state of the guest with nearly 100% efficiency.[41] Thus, only singlet excitons luminesce in the absence of the sensitizer, but both triplets and singlets are detected when the sensitizer is included.

Figure 3.13 shows the quantum efficiency as a function of current density for two OLEDs, one of which uses a sensitizer.[74] The host material is 4,4'-N,N'-dicarbazolyl-biphenyl (CBP), the fluorescent guest is DCM2, and the phosphorescent sensitizer is *fac* tris(2-phenylpyridine)iridium ($Ir(ppy)_3$). The spin fraction is calculated from the ratio of efficiencies with and without the sensitizer to be (22±2)%, independent of current density and electric field.[74] In both OLEDs, luminescence is emitted from the guest fluorescent molecule, thereby eliminating errors due to the differing radiative efficiencies in comparisons of fluorescence and phosphorescence.[36] The technique may, however, overestimate the singlet fraction if triplets form directly on the fluorescent guest rather than on the host or sensitizer. Thus, the most accurate measurements[74] employ very low concentrations (~0.2%) of the fluorescent dye and high concentrations (~8%) of the phosphorescent sensitizer. Excitons may also form predominantly on the small molecular weight phosphorescent sensitizer when it is present at 8% in a host material.[51] Uncertainties in the exciton formation site prevent application of the small molecular weight phosphor sensitization technique to polymers. Together with the results from this work, and from Wilson, *et al.* (discussed below), four independent measurements consistently find $0.20 < \chi_S < 0.22$ in small molecular weight materials.

### 3.7.2 Measurements of $\chi_s$ in polymeric materials comparing EL to PL

In contrast to small molecules, several measurements of conjugated polymers, using both absolute and relative techniques, find that $\chi_S > 0.25$. In their absolute measurements, Cao, *et al.*[52] studied EL and PL from the same luminescent polymer film, thereby reducing systematic errors. Kim, *et al.*[53] also compared EL and PL efficiencies, taking care to estimate microcavity effects within their EL devices so as to obtain a minimum value for $\chi_S$. In measurements of neat films of OC1C10 (Table 1) between temperatures of 290K and 360K, Cao, *et al.*[52] found $\gamma\chi_S \sim 0.25$. But in heterostructures with mixtures of OC1C10 and the electron-transporting small molecular weight material Bu-PBD, $\gamma\chi_S$ increased from 0.25 at room temperature to 0.5 at 360K. The observed temperature dependence may be the result of variations in the EL-specific loss, $\gamma$. However, our measurement of the temperature dependence of the EL efficiency of bilayer devices of MEH-PPV and the electron-transporting small molecular weight material BCP failed to repeat the effect; in fact the EL efficiency obtained here was found to have the opposite dependence on temperature from that of Cao.

In an alternate approach, Wilson and co-workers[54] use a Pt-containing polymer[83] and monomer with enhanced spin-orbit coupling that allows simultaneous measurement of fluorescence from singlets and phosphorescence from triplets. While efficient ISC leads to almost 100% conversion into triplets, the fluorescence and phosphorescence intensities are comparable since the phosphorescence is weak and nonradiative processes dominate. The total photoluminescent efficiency at room temperature is 1.1% for the monomer and 0.24% for the polymer.[84] The singlet fraction is then inferred by comparing the ratio of fluorescence

to phosphorescence in both EL and PL. The monomer and polymer moieties exhibit similar fluorescent and phosphorescent spectra, indicating that singlet and triplet excitons are confined to a single repeat unit along the chain. Differences in $\chi_S$ cannot therefore be attributed to delocalization that would typically accompany conjugation along the polymer backbone.[28,30,80,85]

Now, the ratio of fluorescence, $\Phi_f$, to phosphorescence, $\Phi_p$, in EL divided by PL, gives, in terms of the rates in Fig. 3.1,

$$\left(\Phi_f/\Phi_p\right)_{EL}\Big/\left(\Phi_f/\Phi_p\right)_{PL}=\frac{\chi_S}{b}\left(\frac{\eta_f}{\eta_p}\right)_{EL}\left(\frac{\eta_p}{\eta_f}\right)_{PL} \tag{3.32}$$

where the fluorescent and phosphorescent efficiencies are $\eta_f = k_r^f/(k_r^f + k_{nr}^f + k_{ISC})$ and $\eta_p = k_r^p/(k_r^p + k_{nr}^p)$, respectively. The branching ratio $b$ is:

$$b=\frac{\chi_S k_{BS}+k_{S*}}{k_{S*}+k_{BS}+k_{ISC*}} \tag{3.33}$$

where the mixing rate between singlet and triplet CT states is assumed to be high ($k_{SL}$ large).

By this method, Wilson, *et al.*,[54] find that $\chi_S = (57\pm4)\%$ in their polymer and $\chi_S = (22\pm1)\%$ for the monomer. It is assumed that $k_{ISC}$, $\eta_f$ and $\eta_p$ are the same in EL as they are in PL. It is also assumed that the branching ratio $b \sim 1$. When $b \sim 1$, S* $\rightarrow$ S occurs with unit efficiency, so that optical excitation even well above the band edge[84] leads exclusively to S. This is a key assumption since $\chi_S$ is proportional to $b$ (Eq. (3.32)). CT states, however, provide additional pathways for energy relaxation. For example, excitation 0.5 eV above the band edge leads to a lowered quantum yield for fluorescence in a polysilane, but not in crystalline anthracene.[86] The value of $b$, then, may in fact be substantially below unity in polymers,[60,87] influencing measurements of $\chi_S$. It is notable that similar experiments

employing phosphorescent iridium complexes grafted onto a polyfluorene backbone do not show $\chi_S > 0.25$.[88]

The possibility that the branching ratio is less than unity similarly affects the measurements by Cao *et. al.*[52] and Kim *et al.*[53] given that the measured PL efficiency is proportional to $b$, so that $b < 1$ would result in an overestimate of $\chi_S$. Measurements of $\chi_S$ that compare EL to PL efficiencies should therefore attempt to minimize or measure the rate of excited exciton dissociation into CT states. In this work, we minimize the effect of branching rates such as $k_{ISC*}$ and $k_{BS}$ by exciting the polymer at the edge of its absorption spectrum. In any case, our conclusion that $\chi_S < 25\%$ in MEH-PPV would not be changed by an underestimate of the PL efficiency.

One way to *ensure* correct accounting of the branching ratio in PL is to study polymers with high PL efficiencies, since, if $b\eta_f \rightarrow 1$, branching effects must be negligible. To date, measurements of $\chi_S > 25\%$ using comparisons of EL and PL have only been obtained in polymers with relatively low PL efficiencies as shown in Table 1. Due to their high PL efficiencies, polyfluorenes seem especially suited to accurate measurements of $\chi_S$.[89]

In summary, the relaxation pathways of CT and exciton states shown in Fig. 3.1 are complicated and poorly quantified in most polymers. There are significant unresolved contradictions in the published measurements of $\chi_S$ that presently prevent a firm determination of the singlet fraction in polymeric materials, even in the specific case of MEH-PPV. In addition to varying results for $\chi_S$, there are differences in the implied or reported temperature dependence[28,52,54] and electric field dependence[52,54,78] of $\chi_S$, and apparent differences between ELDMR and the interpretation of PADMR data. We have commented in

this section on assumptions and approximations in reports of $\chi_S > 0.25$. We noted in Sections IV and V some experimental considerations when measuring $\chi_S$ using the reverse bias technique, including a possible sensitivity to EL specific loss, which may be material dependent, and the requirement for efficient charge extraction, which also cannot be ensured in all cases.

### 3.7.3 CT state detection

Conventional measurements of PL efficiency require absolute determinations of absorption and fluorescence. Typically these measurements are performed consecutively in an integrating sphere.[66] However, many potentially interesting organic materials suffer from instabilities that may corrupt such PL measurements. Figure 3.14 shows the change in PL and absorption of a 300Å-thick MEH-PPV thin film with time as it is exposed to a pump laser with wavelength $\lambda$ = 405 nm and intensity ~ 0.4 W/cm$^2$ in an environment with less than 25 ppm oxygen. The film was spun onto a cleaned glass slide and baked at T = 115 °C for at least 10 hours. The film was never exposed to room air. It is seen in Fig. 3.15 that both PL *and* absorption decrease rapidly. The decrease in PL is not fully accounted for by the decrease in absorption, suggesting that it is at least partially due to an irreversible degradation process which is expected to create defect sites that enhance the rate of exciton dissociation into CT states.[60,80] Indeed, a chemical change in the photoexcited film leading to the formation of new energetic states is evidenced by the increase in absorption for $t < 1$ hour. Exposure of a second, identical, MEH-PPV thin film to a pump laser with wavelength $\lambda$ = 532 nm and intensity ~3 W/cm$^2$ produces similar rapid declines in PL and absorption. Optical micrographs of this second film demonstrate that the decrease in absorption is partly due to morphological

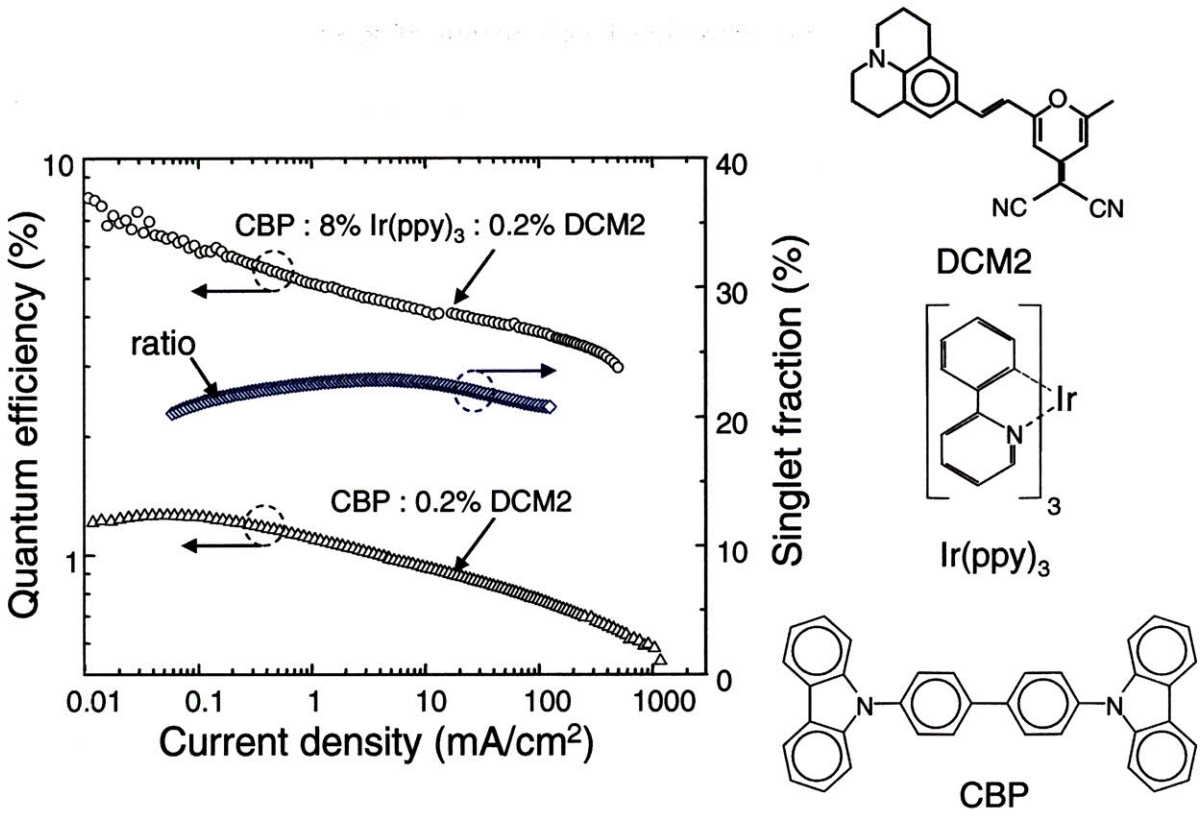


Figure 3.14 – The external quantum efficiencies of the fluorescent dye DCM2 with and without phosphorescent sensitization by tris-(2-phenylpyridine) iridium ($Ir(ppy)_3$). The host material is 4,4'-N,N'-dicarbazole-biphenyl (CBP). The chemical structures of the materials are shown in the inset. The ratio between sensitized and unsensitized emission gives $\chi_S = (22\pm2)\%$. Adapted from D'Andrade, *et al.* (Ref. [74]).

changes, including peeling of the thin polymer film. Conventional PL efficiency measurements must compensate for such possible changes with time of the absorption, fluorescence, and branching ratio, especially in circumstances where the organic material is necessarily fragile, for example in studies of very thin films of MEH-PPV.

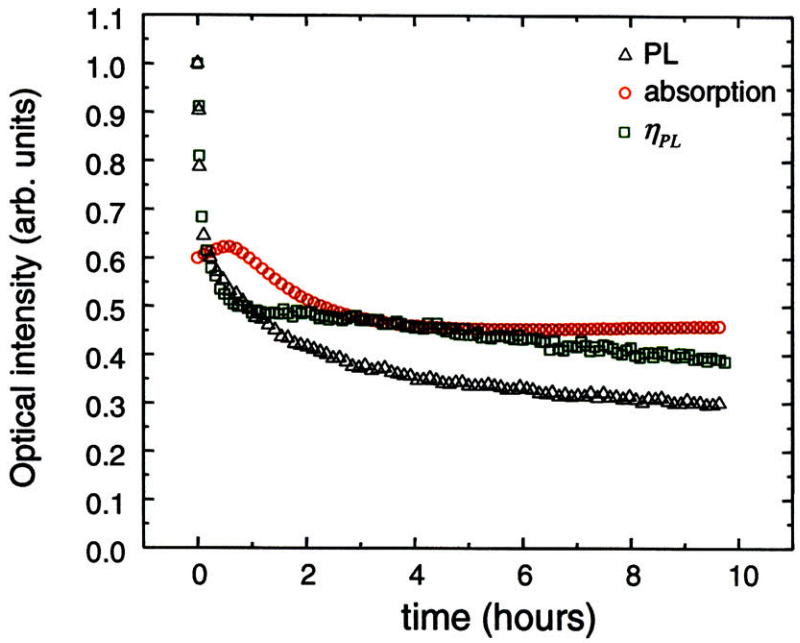


Figure 3.15 - Change in photoluminescence, absorption and PL efficiency of a thin film of MEH-PPV exposed to a pump laser with wavelength $\lambda = 405$ nm and intensity 0.4 W/cm$^2$ as a function of time. PL efficiency and fluorescence are normalized to 1.

These photophysical changes can be caused by morphological instabilities in the film or by chemical degradation, which may occur even in a low-oxygen environment, since impurities may be incorporated during film deposition. Thus, if the organic film can be incorporated into an OLED, the reverse bias technique may be preferred, both for its insensitivity to absorption strength, and its ability to detect branching ratios below unity. Indeed, linear reverse bias characteristics were measured over time scales of approximately half an hour on thin films of MEH-PPV incorporated into OLEDs, using the same $\lambda = 532$ nm optical pump that produced rapid declines in PL and absorption as discussed above.[22]

Finally, we note that measurements of PL efficiency have been critical in determining the ratio of singlet to triplet excitons formed in the electroluminescence of high efficiency polymeric OLEDs. Based on comparisons of EL and PL, several recent studies have concluded that the singlet fraction is well above the spin-degenerate limit of 25%.[52-54] However, as noted above, measurements of PL efficiency can result in underestimates if the branching ratio is below unity. Indeed, if $b_0 = 0$, then under the model described in Fig. 3.1, optical excitation is exactly equivalent to electrical excitation, yielding an apparent singlet fraction of $\chi_S = \text{EL/PL} \sim 100\%$. Here again, it is desirable to employ a PL measurement technique that detects the presence of a low branching ratio. Otherwise, it may be necessary to record the photoexcitation spectrum before and after each PL and EL measurement.

## 3.8. Conclusions

We use a simple reverse bias technique for measuring the photoluminescent (PL) efficiency of an organic light emitting device, and by comparing to the electroluminescent (EL) efficiency measured in the same geometry, find that the fraction of excitons formed as singlets in the electroluminescence of $Alq_3$ is $\chi_S = (20\pm1)\%$. This confirms other measurements showing that the exciton formation statistics in small molecular weight materials approximately follow the 25% spin-degeneracy statistical limit. MEH-PPV is found to have $\chi_S = (20\pm4)\%$, also consistent with the spin-degeneracy limit. This result in an archetypal conjugated polymer like MEH-PPV suggests that the singlet fraction may have a 25% limit in polymers generally, though the possibility that $\chi_S$ is material-dependent cannot be ruled out.

Measurement of $\chi_S$ is motivated in part by its relevance to highly efficient electroluminescent materials. In small molecular weight materials, the maximum observed EL quantum efficiency of fluorescent devices is 4-5%, but is ~ 20% in small molecular weight phosphorescent devices.[56,90] Similar limits appear to hold for fluorescent polymer devices, *i.e.* external quantum efficiencies of $<< 20\%$.[53,91] Given the high photoluminescent and outcoupling efficiencies of some polymers, it might be expected that measurements of $\chi_S > 25\%$ should be reflected in polymeric EL fluorescent quantum efficiencies that approach the $\eta_{EL}$~ 20% observed in phosphorescent small molecular weight materials, although such efficiencies have not yet been demonstrated.

Thus, in addition to the potential for providing insights into exciton formation, quantification of exciton formation statistics is critical to the full exploitation of organic electroluminescent technology. By harnessing triplets and singlets, phosphorescent OLEDs exhibit efficiencies approximately four times that of molecular OLEDs that fluoresce from singlets alone.[36] If, as is observed in this chapter, the formation statistics of excitons in polymeric semiconductors are similar to the statistics in small molecular weight materials, then it is clearly desirable to develop phosphorescent or extrafluorescent (see Chapter 5) polymeric OLEDs.

In addition, knowledge of the branching ratio $b_0$ for the formation of relaxed singlet excitons from excited singlet excitons is necessary for measurements of the ideal photoluminescent efficiency of organic materials. Predicting the branching ratio is difficult, since it is expected to be dependent on the type and preparation of the organic material, on a variety of degradation processes, and on wavelength, even for pristine materials.[60,86] In particular, degradation under optical excitation may occur rapidly even in a low-oxygen

environment. It is desirable to employ a PL efficiency measurement technique which inherently also indicates whether $b_0$ is substantially less than unity. The reverse bias measurement technique detects the presence of CT states formed when $b_0$ is less than unity, and is also insensitive to changes in absorption strength, two potentially important advantages over conventional, absolute PL efficiency measurements. Finally, measurements of high (> 25%) singlet fractions in polymers under electroluminescence should be evaluated in light of the possibility that the branching ratio is substantially less than unity.

Finally, in the language of Fig. 2.13, the measurement of $\chi_S \approx 25\%$ for the variety of materials considered here ($Alq_3$, MEH-PPV, and, from a previous measurement, CBP[74]) requires that $k_{Sm} \approx k_{Tm}$ in those materials, ie, the singlet and triplet formation rates from the last-mixed CT state are approximately equal. Given the very different nature of the final singlet and triplet exciton states, it is expected that $k_{SI}$ and $k_{TI}$ in these materials are not to equal, and should in any case vary from material to material. The implication is therefore that $m > 1$. This is confirmed in Chapter 5.

# Chapter 4. Spin Resonance Measurements

## 4.1 – Introduction

Studies of optically-detected magnetic resonances (ODMR) offer a unique probe of spin-dependent phenomena in organic semiconductors.[92] The technique is particularly useful for studying dark excitations – species that are normally incapable of photoluminescence, such as spin-1/2 polarons and spin-1 triplet excitons, large populations of which may be generated under sustained illumination. Recent interpretations of spin-1/2 ODMR experiments have been used to predict the relative formation rates of singlet (SE) and triplet (TE) excitons under electrical excitation,[28,80]. These and other interpretations of ODMR data, however, rely on a physical model of the origins of the spin-1/2 resonance that continues to be debated.[93] In this Section, we propose that interactions between TEs and polarons underlie the spin-1/2 ODMR, and that two types of polarons are present: short-lived paired polarons that may recombine after spin-dependent collisions with TEs, and long-lived unpaired polarons that are re-trapped before they can recombine. As a result, paired polarons are affected by magnetic resonance, and unpaired polarons are not. We are able to construct a full quantitative model of the ODMR on this basis that successfully predicts the measured frequency responses of resonant and photoinduced absorption data of the archetypal π-conjugated polymer poly[2-methoxy-5-(2-ethylhexyloxy)-1,4-phenylenevinylene] (MEH-PPV).

Figure 4.1 shows a schematic for an optically-detected magnetic resonance experiment. An organic semiconductor is optically or electrically pumped under an applied

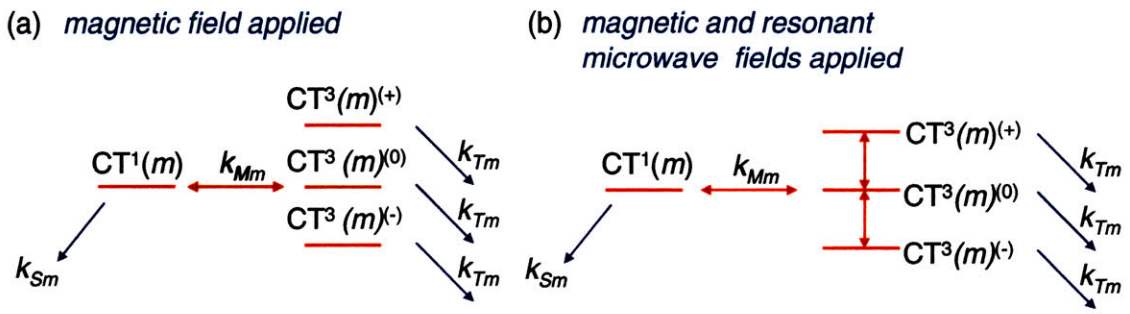


Figure 4.1 – An optically-detected magnetic resonance (ODMR) experiment schematic. (a) A magnetic field lifts the degeneracy of triplet exciton and CT states, including the CT($m$) state (Fig. 2.13). (b) A resonant microwave field then equalizes the populations of the triplet states, and, through $k_{Mm}$, the singlet state.

external magnetic field, creating all of the states shown in Fig. 2.13. The three projections of the triplet state, for both CT states and excitons (Fig. 2.2), are normally degenerate, with local magnetic fields causing a splitting of less than $k_BT$. The applied magnetic field lifts the degeneracy of all of the triplet states in the material, and the microwave field equalizes the population of these states. The equalization of the exciton triplet levels has no effect. The equalization of the triplet level degeneracy for CT states with $n > m$ can be ignored, since those states are effectively re-mixed at $n$+1 anyways. The lifting of the triplet level degeneracy for CT states with $n < m$ has no effect, since those states are unmixed. Therefore the effect of ODMR can be understood by considering only CT($m$).

In the case that a large ODMR effect is observed, the populations of the three triplet CT($m$) states (with $m_j$ = -1, 0 and +1) must not be equal, outside of resonance. This could be caused by differing $k_{Sm}$ and $k_{Tm}$ rates: $k_{Sm} > k_{Tm}$, for example, would reduce the population of

the $m_j = 0$ $CT^3(m)$ state relative to the $m_j = -1$ and +1 states. If $k_{Tm} > k_{Sm}$, the $m_j = 0$ $CT^3(m)$ state would draw on $CT^1(m)$ states, and would have a larger population than $CT^3(m)$ states with $m_j = -1$ and +1. On the other hand, a very small ODMR effect would indicate that $k_{Sm} \approx k_{Tm}$.

ODMR experiments, then, measure spectroscopic changes caused by resonance. These include changes in photoinduced absorption (PADMR), in photoluminescence (PLDMR), and in electroluminescence (ELDMR). Although TE resonances are also commonly observed, the sharp, PL enhancing and PA quenching, spin-1/2 polaron resonance with $g$-factor $g = (2.0025 \pm 0.0006)$[94] has been studied most intensively and is the focus of this work. The increase in fluorescence ($\Delta PL > 0$) and the decrease in polaron and TE densities ($\Delta PA < 0$) under spin-1/2 resonance conditions have been well established in numerous prototypical polymers.[28,92,95-100]

Electroluminescence-detected magnetic resonance (ELDMR) data affords a preliminary conclusion on the question of $k_{Sm}$ / $k_{Tm}$. In ELDMR experiments, the electroluminescence of an OLED under an applied magnetic field derives from the singlet CT state. The formation rate $k_{Sm}$ competes only with the rate $k_{Tm}$ from the $m_j = 0$ triplet CT state with which the singlet is mixed. The EL in this case is thus proportional to $\frac{k_{Sm}}{2(k_{Sm} + k_{Tm})}$ (the factor of 2 in the denominator results from the fact that $CT^1(m)$ and $CT^3(m)$ with $m_j = 0$ are 50% likely to be occupied). When a microwave field is applied, the three triplet state populations are equalized. Now, $k_{Sm}$ competes with the rate from every triplet state (every $m_j$), and is proportional to $\frac{k_{Sm}}{k_{Sm} + 3k_{Tm}}$. The ELDMR effect, $s_{ELDMR}$, is the difference between the

electroluminescence in the presence and absence of the microwave field, normalized to the electroluminescence in the absence of the microwave field:

$$s_{ELDMR} = \frac{k_{Sm} - k_{Tm}}{k_{Sm} + 3k_{Tm}}. \tag{4.1}$$

Measurements of $s_{ELDMR}$ for small molecular weight materials and polymers such as PPV are on the order of $1 \times 10^{-4}$, [81,82] implying that $k_{Sm} \approx k_{Tm}$. This is consistent with the conclusion from Section 3.8 above. It is also noteworthy that the sign $s_{ELDMR}$ has been measured to be both positive and negative. Negative PPV resonances may be partly attributed to a decrease in the conductivity of the devices under resonance conditions.

Wohlgenannt, *et al.*,[28,80] however, interpret magnetic resonance data as suggesting that $k_{Sm} > k_{Tm}$. These workers use photo-absorption detected magnetic resonance, which is analogous to ELDMR, but in which photo-absorption rather than electroluminescence is measured. Photo-absorption strength reflects polaron density, and drops under resonance. At the same time, photoluminescence (proportional to the singlet population) increases, and triplet exciton density (also measured by photo-absorption) decreases. Under resonance, the populations of the three triplet states and one singlet state are equalized through spin flipping. This allows polaron pairs

initially formed in a triplet configuration to change configuration and form singlet excitons. Thus, under resonance conditions, either $k_{Sm}$ or $k_{Tm}$ can dominate exciton formation, and if one rate is larger than the other, the resonant rate of exciton formation will increase, and the polaron population will decrease, as observed. Consequently, Wohlgenannt, *et al.*,[28,80] take $k_{Sm} > k_{Tm}$, and from changes in the polaron absorption under resonance calculate $1.7 < k_{Sm}/$

$k_{Tm} < 5$ for a range of π-conjugated polymers and oligomers, and specifically, $\chi_S = 47\%$ in MEH-PPV.

The ionic character of singlet excitons may result in stronger overlap with the initial polaron pair, leading to $k_{SI} > k_{TI}$.[28] However, as pointed out in Fig. 2.13, these rates are only relevant if they are mixed ($k_{MI}$ is large). Also, analyses of the magnetic field dependence of photoconductivity in polymers suggest that $k_{TI} > k_{SI}$.[101] Furthermore, for $1.7 < k_{Sm} / k_{Tm} < 5$, as measured by Wohlgenannt *et al*, the ELDMR signal is expected to be 10-50%, rather than the 1e-4 measured. Finally, in Chaper 3, $\chi_S$ in MEH-PPV was measured to be < 25%. Note also that while both resonance-based measurements of $k_{Sm}$ and $k_{Tm}$, and EL/PL measurements are related to $\chi_S$, they are not the same; the largest $k_S/k_T$ values are reported[4] for polymers that do not fluoresce, since the lowest-energy singlet state has $A_g$ rather than $B_u$ symmetry.

These contradictions have been resolved by the demonstration that photoluminescence-detected magnetic resonance signals do not result from exciton formation processes, as is required if $k_{Sm} / k_{Tm}$ is to be inferred from the data.[93] Below, we show that ODMR effects result from a spin-dependent singlet exciton quenching process. The contribution of exciton formation dynamics to ODMR effects is small, if it exists at all. Therefore, $k_{Sm} \approx k_{Tm}$, in agreement with Chapter 3.

## 4.2 Quenching And Recombination

Two types of models for ODMR resonances have been proposed, based on recombination and quenching, respectively. Recombination models consider $\Delta PL > 0$ to be a form of delayed fluorescence resulting from the recombination of slow (long-lived) polarons, and have been used to argue that SE formation is favored over TE formation in organic light

emitting devices (OLEDs).[28,80] The recent observation of $\Delta PL > 0$ under optical modulation frequencies orders of magnitude greater than the inverse polaron lifetime is, however, inconsistent with recombination.[93] Qualitatively, it is instead possible to explain the resonance with quenching models, under which $\Delta PL > 0$ is due to reduced SE annihilation under resonance conditions. The SE population readily follows fast modulation since the singlet exciton lifetime is on the order of 1 ns. But the identity of the quenchers and the reason for their population change under resonance remain open questions. In this section, we address these questions and build a quenching model of PLDMR experiments on MEH-PPV at low temperature. TE and polaron populations in MEH-PPV at 80 K are known experimentally to decrease under resonance.[102] Here we take into account SE quenching by both TE and polarons. In view of the limited charge mobility at low temperature, we also distinguish between polarons trapped in pairs and isolated trapped polarons. We further identify the origin of the reduction of TE and polaron populations under resonance as TE-polaron quenching (TPQ). Spin-dependent processes involving TEs and electrons or holes are well known in organic molecular crystals.[1] The greater rate of TPQ under resonance is the basis for decreased quenching of SEs and is also consistent with $\Delta PA < 0$.

We focus in this section on using the TPQ model to explain the dynamics of multiple quenching species, $X$, as measured by three experimental probes: (i) PLDMR, (ii) photoinduced absorption (PA), and (iii) double modulated PLDMR (DM-PLDMR). To briefly summarize the detailed analysis that follows this introduction, we note that in a quenching model, each SE quencher satisfies the steady-state relation

$$\frac{dS}{dt} = G_S - \frac{S}{\tau_S} - \gamma_{SX} XS = 0, \qquad (4.2)$$

where $G_S$ is the rate of generating SEs, $S$ is the SE density, $\tau_S \approx 1$ ns, and $\gamma_{SX}$ is the SE quenching rate. Since $\Delta PL > 0$ is a small (<0.1%) correction to $S = G_S\tau_S$, the magnitude of the PLDMR under a quenching model is approximately

$$\Delta PL = S^* - S = S\tau_S\gamma_{SX}(X - X^*), \tag{4.3}$$

where the star indicates resonance conditions. The lifetime of SEs is much shorter than that of the long-lived quenching species. Thus, the frequency response of the PLDMR signal $\Delta PL$ provides a direct measurement of the dynamics of the quenching species, $X$, under microwave modulation. Alternately, we may measure the frequency response of $X$ under optical modulation using PA. For the discussion that follows we define $F_{XL}$ and $F_{XM}$ as the frequency responses of $X$ to light and microwave modulation respectively, normalized to unity at zero frequency.

Further insight is gained by studying polaron and exciton dynamics in a double modulated PLDMR (DM-PLDMR) experiment,[93] in which both the microwave field and the optical pump are modulated. Under a quenching model, DM-PLDMR has

$$X(t) = \overline{X}\left[1 + \alpha_L F_{XL}(\omega_L)\cos(\omega_L t)\right]\left[1 + \alpha_{XM} F_{XM}(\omega_M)\cos(\omega_M t)\right] \tag{4.4}$$

$$S(t) = \overline{S}\left[1 + \alpha_L \cos(\omega_L t)\right], \tag{4.5}$$

where bars indicate average values, $\alpha$ indicates modulation depth, and the zero-frequency light modulation depth is assumed to be the same for $S$ and $X$. Detecting only that component that is modulated by both the optical pump and the microwave field, the DM-PLDMR signal under a quenching model is

$$\Delta PL\big|_{f_M, f_L} = \gamma_{SX}\alpha_L\alpha_M \overline{X}\,\overline{S} F_{XM}\left(1 + F_{XL}\right). \tag{4.6}$$

Significantly, the DM-PLDMR frequency response of MEH-PPV has been observed[93] to be independent of the optical modulation frequency $f_L$ for 1 kHz < $f_L$ < 100 kHz, invalidating spin-dependent recombination models of PLDMR. Equation (4.6) demonstrates that a quenching model successfully explains this flat response if $F_{XL}$ is much less than unity over this frequency range, since $F_{XL}$ is the only variable in Eq. (4.6) that depends on $f_L$. Direct measurements of $F_{XL}$ show that this condition is satisfied,[93] and also that $F_{XL}$ differs substantially from $F_{XM}$. In this work, we build a complete model of $F_{XL}$ and $F_{XM}$, calculate the contributions to these responses of the various excited states in MEH-PPV, and demonstrate that $F_{XL}$ and $F_{XM}$ differ both because of the existence of distinct populations of paired and unpaired polarons, and also because of interactions among quenchers. This analysis considers a coupled system of three quenching species: TEs, paired polarons, and unpaired polarons - the populations of which all turn out to be interdependent and much larger than the SE population.

We construct a complete quantitative model of PLDMR below, and demonstrate that PLDMR frequency response data can be used to predict the dynamics of TEs, as well as that of paired and unpaired polarons. In Part II we describe theoretically the frequency dependencies expected under the TPQ model. In Part III, we review the experimental frequency dependence of MEH-PPV,[93] and in Part IV we compare it to the responses expected from the TPQ model. We show that this model can account for the measured data, and extract parameter values from a quenching fit to the data. We discuss the results in Part V, and in the conclusion, Part VI, we summarize the physics of the resonance and the properties of the various excited states of MEH-PPV.

### 4.3 TE-Polaron Quenching Model

The generation of polarons and TEs is mediated by SEs, which are the primary excitations produced by an optical pump. Although only geminate pairs of polarons are formed by the dissociation of SEs, polaron spins are dephased and uncorrelated within 10 - 100 ns by hyperfine fields.[1] At low temperatures, polarons are localized by the disordered energetic environment of the amorphous polymeric film. Thus, even if the separation distance between oppositely charged polarons is short, the lifetime of the pair can exceed 100μs. We distinguish here between polarons which are localized near an oppositely charged neighbor (paired polarons), and polarons which are not (unpaired polarons). Evidence for the existence of paired and unpaired polarons has been found in studies of the intensity dependence of the resonance[103] and in resonance lineshapes.[104]

TEs are generated either from SEs by intersystem crossing or by the recombination of spin-randomized polarons. Since the radiative decay of TEs is retarded by spin conservation, TEs, like localized polarons, have long lifetimes. Indeed, the populations of polarons and TEs can easily exceed that of SEs under continuous illumination due to their long lifetimes, even though mostly SEs are generated directly by the optical pump.

Quenching of SEs by polarons and TEs has been invoked in several studies,[92,103-109] and the involvement of quenching processes has been suggested previously in interpretations of ODMR experiments.[92,103-105,108,109] But quenching interactions between SEs, and polarons or TEs, are not spin-dependent and will therefore not be affected by resonance. Thus, quenching-dependent resonances must be due to spin-dependent interactions among the quenching species themselves. We propose here that the positive spin-1/2 and the spin-1 TE ODMR originate in the spin-dependence of TE-polaron collisions. TE collisions with an

unpaired and a paired polaron are shown schematically in Figs. 4.2(a) and 4.2(b), respectively. In both cases a TE gives up its energy to a polaron and the TE is quenched. The polaron is excited and is more likely to recombine if there is a nearby oppositely-charged polaron. Thus, the collision leads to a decrease in the densities of TEs and *paired* polarons. The unpaired polaron density is unaffected: the excited polaron simply relaxes to its electronic ground state. In organic crystals[1] and OLEDs,[70] injected electrons or holes annihilate TEs by this mechanism.

The spin-dependence of TE-polaron annihilation is a result of spin conservation. The system comprised of the colliding spin-1 TE and spin-1/2 polaron has six spin states of equal probability, two of which have spin-1/2. After the TE is quenched, a single excited polaron with spin-1/2 remains. Spin conservation therefore disallows 2/3 of TE-polaron collisions. Spin-1/2 resonance conditions induce rapid transitions between the spin-1/2 sublevels, so that all collisions become allowed. This increases the TE-polaron annihilation rate, drives down the paired polaron and TE densities, and reduces the rate of singlet quenching by those species.[1] Similarly, spin-1 resonance conditions also increase the TE-polaron annihilation rate and will reduce the rate of singlet quenching.

We now proceed to consider the dependence of the single-modulation PLDMR signal $\Delta PL|_{\omega_M}$ on the microwave modulation frequency $\omega_M$ under the TPQ model. We assume throughout this section that all polaron decay events produce singlet and TEs in the ratio $\chi_S$:(1-$\chi_S$), where $\chi_S$ is some constant; see Fig. 4.2(b). The SE density $S$ under the TPQ model is

$$\frac{dS}{dt} = -\frac{S}{\tau_S} - \gamma_{SP} S(P+U) - \gamma_{ST} ST + G_S + \chi_S \left( G_P - \frac{dP}{dt} + G_U - \frac{dU}{dt} \right), \qquad (4.7)$$

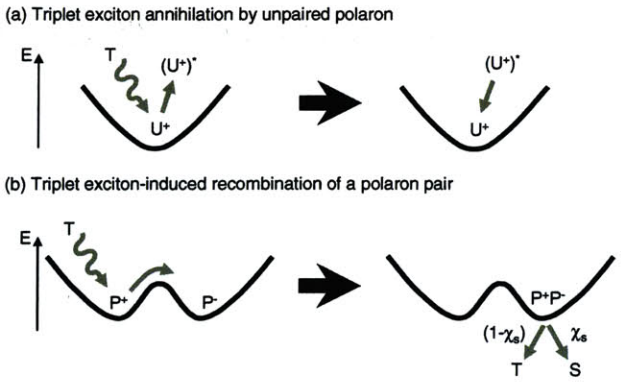


Figure 4.2 - Models for collision between a triplet exciton (TE) and **(a)** unpaired and **(b)** paired polarons at low temperature. In **(a)**, a TE is annihilated by a solitary polaron. The polaron is excited by the collision but relaxes before it encounters an oppositely charged polaron, and is therefore unaffected by TE-polaron collisions or magnetic resonance. In **(b)**, a pair of oppositely charged polarons are trapped in nearby energy wells. After collision with a TE, the TE is annihilated, and one of the polarons is excited, increasing its probability of crossing the energy barrier separating it from its oppositely charged partner. Assuming that the polarons are spin randomized, recombination creates a singlet exciton (SE) or a TE in the ratio $\chi_S$:(1- $\chi_S$), otherwise only SEs are generated by polaron recombination.

where $\tau_S$ is the SE lifetime, $P$ is the density of paired polarons, $U$ is the density of unpaired polarons, $T$ is the TE density, $G_S$ is the singlet formation rate, $G_P$ is the rate of generation of paired polarons, $\gamma_{SP}$ is the interaction rate of SEs with paired and unpaired polarons, $\gamma_{ST}$ is the interaction rate of SEs and TEs, and the recombination rates of paired and unpaired polarons are given generally by $G_P - dP/dt$ and $G_U - dU/dt$ respectively. Setting $dS/dt = 0$, Eq. (4.7) gives

$$S = G_S\tau_S\left[1-\tau_S\gamma_{SP}(P+U)-\tau_S\gamma_{ST}T\right]+\chi_S\left(G_P-\frac{dP}{dt}+G_U-\frac{dU}{dt}\right)\tau_S, \qquad (4.8)$$

where we have assumed that quenching will produce only a small perturbation on $S$, so that $\tau_S\gamma_{SP}(P+U)+\tau_S\gamma_{ST}T \ll 1$, and second-order delayed fluorescence has been ignored.

To determine the frequency dependence, we define $\mathbf{X}^{l,m}$ as the Fourier coefficient for a given modulated rate or species, $X(t)$, so that

$$X(t) = \mathrm{Re}\left\{\sum_{l,m} \boldsymbol{X}^{l,m} e^{il\omega_L t + im\omega_M t}\right\}, \qquad (4.9)$$

where a bold variable is complex and the superscripts $l$ and $m$ refer to harmonics of $\omega_L$ and $\omega_M$ respectively. Under the TPQ model, resonance leaves $\gamma_{SP}$, $\gamma_{ST}$, $\chi_S$ and $U$ unchanged but causes $P$ and $T$ to decrease through an enhanced TE-polaron interaction rate. Then from Eqs. (4.8) and (4.9), with $s = i\omega_M$,

$$\Delta PL\big|_{\omega_M} = \left|\boldsymbol{S}^{0,1}\right| = G_S\tau_S\left|-\tau_S\gamma_{ST}\boldsymbol{T}^{0,1}-\boldsymbol{P}^{0,1}\left(\tau_S\gamma_{SP}+\frac{s}{G_S}\chi_S\right)\right|. \qquad (4.10)$$

We can obtain the forms of $\boldsymbol{T}^{0,1}(\omega_M)$ and $\boldsymbol{P}^{0,1}(\omega_M)$ by considering the rate equations for TEs and polarons under the TPQ model:

$$\frac{dP}{dt} = -\frac{P}{\tau_P}-\gamma_{TP}TP+G_P \qquad (4.11)$$

$$\frac{dT}{dt} = -\frac{T}{\tau_T}+(1-\chi_S)\left(\frac{P}{\tau_P}+\frac{U}{\tau_U}\right)-\chi_S\gamma_{TP}TP-\gamma_{TP}TU+G_T \qquad (4.12)$$

$$\frac{dU}{dt} = -\frac{U}{\tau_U}+G_U. \qquad (4.13)$$

Here, $\gamma_{TP}$ is the collision rate of TEs with both paired and unpaired polarons, where we assume that TEs will be annihilated and paired polarons will recombine with 100% probability; $\tau_P$, $\tau_U$ and $\tau_T$ are the paired polaron, unpaired polaron and TE lifetimes respectively; and $G_T$ is the rate of generation of TEs by intersystem crossing.

Since the changes in the polaron and TE populations under resonance are small, Eqs. (4.11), (4.12) and (4.13) can be linearized to give the frequency response under microwave modulation predicted by the TPQ model. Since $e^{st}$ (where $s$ is complex) is an eigenfunction for all linear systems, the frequency responses of the linearized Eqs. (4.11) - (4.13) are the eigenvalues corresponding to the eigenfunction $e^{st}$ with $s = i\ \omega_M$. We note that at high densities Eqs. (4.11) - (4.13) may not predict the correct steady-state values $P_0$, $T_0$ and $U_0$ due to the implicit linearization in the parameters $\tau_P$, $\tau_T$ and $\tau_U$ of any polaron-polaron or TE-TE bimolecular interactions. The equations are, however, valid for small-signal dynamics.

The TPQ model describes the quantities $P$, $T$ , $\gamma_{TP}$ and $\gamma_{TU}$ as changing under resonance. Taking $\gamma_{TU}$ to be linearly proportional to $\gamma_{TP}$, $P$ and $T$ are linearized as

$$\frac{d}{dt}\begin{pmatrix} P-P_0 \\ T-T_0 \end{pmatrix} = \begin{pmatrix} P_P & P_T & P_\gamma \\ T_P & T_T & T_\gamma \end{pmatrix} \begin{pmatrix} P-P_0 \\ T-T_0 \\ \gamma_{TP}-\gamma_{TP0} \end{pmatrix}. \tag{4.14}$$

Here, a "0" subscript indicates a steady-state value, $P_P$ is the derivative with respect to $P$ of the right hand side of Eq. (4.11) at steady-state, $T_\gamma$ is the derivative with respect to $\gamma_{TP}$ of the right hand side of Eq. (4.12) at steady-state, and so on.

The constants used in the linearized equations (4.14) and (4.26) have the form $X_Y$ and are the derivatives of $X$ with respect to $Y$ for $Y$ at steady state. They are obtained from the expressions for $P$, $T$ and $U$ in Eqs. (4.11), (4.12) and (4.13):

$$P_P = -\frac{1}{\tau_P} - \gamma_{TP0} T_0 \tag{4.15}$$

$$P_T = -\gamma_{TP0} P_0 \tag{4.16}$$

$$P_\gamma = -T_0 P_0 \tag{4.17}$$

$$T_P = -\chi_S \gamma_{TP0} T_0 + (1-\chi_S)\frac{1}{\tau_P} \tag{4.18}$$

$$T_T = -\frac{1}{\tau_T} - \chi_S \gamma_{TP0} P_0 - \gamma_{TP0} U_0 \tag{4.19}$$

$$T_U = \frac{(1-\chi_S)}{\tau_U} - \gamma_{TP0} T_0 \tag{4.20}$$

$$T_\gamma = -\chi_S T_0 P_0 - T_0 U_0 \tag{4.21}$$

$$U_U = -\frac{1}{\tau_U} \tag{4.22}$$

Defining $P(t) - P_0 = \mathrm{Re}\left\{\boldsymbol{P}^{0,1} e^{i\omega_M t}\right\}$ and similarly for $\boldsymbol{T}^{0,1}$, $\boldsymbol{\gamma}^{0,1}$, and then solving Eq. (4.14) with $s = i\omega_M$ gives

$$\frac{\boldsymbol{P}^{0,1}}{\boldsymbol{\gamma}^{0,1}} = \frac{sP_\gamma - T_T P_\gamma + T_\gamma P_T}{s^2 + s(-T_T - P_P) + (P_P T_T - T_P P_T)}, \tag{4.23}$$

$$\frac{\boldsymbol{T}^{0,1}}{\boldsymbol{\gamma}^{0,1}} = \frac{sT_\gamma - P_P T_\gamma + P_\gamma T_P}{s^2 + s(-T_T - P_P) + (P_P T_T - T_P P_T)}. \tag{4.24}$$

From Eqs. (4.10), (4.23) and (4.24), then, under the TPQ model, the single-modulation signal $\Delta PL\big|_{\omega_M}$ will exhibit a two-pole frequency response.

We now consider the double-modulated signal $\Delta PL\big|_{\omega_L,\omega_M}$. From Eq. (4.8), we obtain

$$\Delta PL\big|_{\omega_L,\omega_M} = \mathrm{Re}\left\{\boldsymbol{S}^{1,1}\right\} = -\tau_S^2\,\mathrm{Re}\left\{\begin{array}{l}\gamma_{ST}\boldsymbol{T}^{0,1}\boldsymbol{G}_S^{0,0}\left(\dfrac{\boldsymbol{G}_S^{1,0}}{\boldsymbol{G}_S^{0,0}}+\dfrac{\boldsymbol{T}^{1,0}}{\boldsymbol{T}^{0,0}}\right)\\ +\gamma_{SP}\boldsymbol{P}^{0,1}\boldsymbol{G}_S^{0,0}\left(\dfrac{\boldsymbol{G}_S^{1,0}}{\boldsymbol{G}_S^{0,0}}+\dfrac{\boldsymbol{P}^{1,0}}{\boldsymbol{P}^{0,0}}\right)\\ +\dfrac{\chi_S i(\omega_L+\omega_M)\boldsymbol{P}^{1,1}}{\tau_S}\end{array}\right\} \tag{4.25}$$

The real part is taken because in the double lock-in experiment, the quenching contribution is small compared to the average PL, which is in phase with the optical modulation. An expression for $\boldsymbol{P}^{1,1}$ can be obtained by expanding Eqs. (4.11) and (4.12) in Fourier series, and substituting Eqs. (4.23), (4.24), (4.27) and (4.28). $\boldsymbol{P}^{1,1}$ falls to zero at high frequency. We obtain $\boldsymbol{P}^{1,0}(\omega_L)$ and $\boldsymbol{T}^{1,0}(\omega_L)$, and hence $\Delta PL\big|_{\omega_L,\omega_M}$, by repeating the linearization of Eqs. (4.11) and (4.12) in the case that only the optical power is modulated. In that case, only the quantities $P$, $T$, $U$, $G_P$, $G_T$ and $G_U$ vary, so that

$$\frac{d}{dt}\begin{pmatrix}P-P_0\\U-U_0\\T-T_0\end{pmatrix} = \begin{pmatrix}P_P & 0 & P_T\\0 & U_U & 0\\T_P & T_U & T_T\end{pmatrix}\begin{pmatrix}P-P_0\\U-U_0\\T-T_0\end{pmatrix} + \begin{pmatrix}G_P-G_{P0}\\G_U-G_{U0}\\G_T-G_{T0}\end{pmatrix}. \tag{4.26}$$

Here, $U_U$ is the derivative with respect to $U$ of the right hand side of Eq. (4.13), and so on. Analogous to the microwave-modulation case, we define $P(t)-P_0 = \mathrm{Re}\left\{\boldsymbol{P}^{1,0}e^{i\omega_L t}\right\}$, and similarly for $\boldsymbol{U}^{1,0}$, $\boldsymbol{T}^{1,0}$, $\boldsymbol{G}_P^{1,0}$, $\boldsymbol{G}_U^{1,0}$, $\boldsymbol{G}_T^{1,0}$. The matrix elements in Eq. (4.26) are listed in Appendix I, and its solution with $s = i\omega_L$ is

$$\frac{\boldsymbol{P}^{1,0}}{\boldsymbol{G_P}^{1,0}} = \frac{s^2+s\left[P_T\dfrac{G_T}{G_P}-(T_T+U_U)\right]-\dfrac{G_T}{G_P}U_UP_T+\dfrac{G_U}{G_P}T_UP_T+T_TU_U}{(s-U_U)\left[s^2+s(-T_T-P_P)+(P_PT_T-T_PP_T)\right]} \tag{4.27}$$

$$\frac{\boldsymbol{T}^{1,0}}{\boldsymbol{G}_P^{1,0}} = \frac{s^2\frac{G_T}{G_P} + s\left[T_U\frac{G_U}{G_P} + T_P - \frac{G_T}{G_P}(U_U + P_P)\right] + \frac{G_T}{G_P}U_U P_P - \frac{G_U}{G_P}T_U P_P - T_P U_U}{(s-U_U)\left[s^2 + s(-T_T - P_P) + (P_P T_T - T_P P_T)\right]}. \quad (4.28)$$

Comparing Eqs. (4.27) and (4.28) to Eqs. (4.23) and (4.24), we see that the three poles of $\boldsymbol{P}^{1,0}$ and $\boldsymbol{T}^{1,0}$ include the two poles of $\boldsymbol{P}^{0,1}$ and $\boldsymbol{T}^{0,1}$, along with a pole at $s = U_U$. The simple form of this extra pole results from the fact that $U$ is affected by the optical pump modulation but not by resonance.

Equation (4.25) shows that under the TPQ model, the double-modulation signal includes a contribution from quenching of singlet excitons by the steady-state or *average* populations of the quenching species ($\boldsymbol{P}^{0,1}$ and $\boldsymbol{T}^{0,1}$). This is a unique feature of the TPQ model, and is not found for example in the equivalent expression under the recombination model, since in that model an average polaron population cannot contribute to the double-modulated signal. We find below that $\Delta PL|_{\omega_L,\omega_M}$ in MEH-PPV is dominated by the interaction between light-modulated SEs and the steady state TE population, *i.e.*, $\Delta PL|_{\omega_L,\omega_M} \propto \boldsymbol{T}^{0,1}\boldsymbol{G}_S^{1,0}$, and is independent of the optical modulation frequency $\omega_L$ for this reason.

To see that $\Delta PL|_{\omega_L,\omega_M}$ cannot be independent of $\omega_L$ under the SDR model, we linearize the SDR equations. First we consider the dependence under the spin-dependent recombination (SDR) model of the single-modulated PLDMR signal $\Delta PL|_{\omega_M}$ on microwave modulation frequency $\omega_M$.[28] Following Ref. [55], we consider only unpaired polarons $U$ and treat unpaired polaron recombination as a bimolecular process, so that the SE density $S$ is

$$\frac{dS}{dt} = -\frac{S}{\tau_S} + \chi_S\gamma_{UU}U^2 + G_S \quad (4.29)$$

where $\gamma_{UU}$ is the interaction rate of unpaired polarons. When all modulation frequencies are much smaller than $1/\tau_S$, we may set $dS/dt = 0$ so that Eq. (4.29) gives

$$S = \chi_S \gamma_{UU} U^2 \tau_S + G_S \tau_S . \tag{4.30}$$

Under the SDR model, resonance causes the SE fraction $\chi_S$ and the unpaired polaron recombination rate $\gamma_{UU}$ to increase. Then from Eqs. (4.30) and (4.9) the single-modulated PLDMR signal will be

$$\Delta PL\big|_{\omega_M} = \left|S^{0,1}\right| = \tau_S \left| \chi_S^{0,1} \gamma_{UU}^{0,0} \left(U^{0,0}\right)^2 + \chi_S^{0,0} \gamma_{UU}^{0,1} \left(U^{0,0}\right)^2 + 2\chi_S^{0,0} \gamma_{UU}^{0,0} U^{0,0} U^{0,1} \right| . \tag{4.31}$$

The quantities $\chi_S^{0,1}$ and $\gamma_{UU}^{0,1}$ are independent of the microwave modulation frequency and so the first and second terms of Eq. (4.31) produce only a constant offset, and the dependence of $\Delta PL\big|_{\omega_M}$ on $\omega_M$ comes entirely from the last term. We can obtain the form of $U^{0,1}(\omega_M)$ by considering the rate equation for polarons under the SDR model[95],

$$\frac{dU}{dt} = -\gamma_{UU} U^2 + G_U , \tag{4.32}$$

where $G_U$ is the rate of generation of unpaired polarons. Since the variation in $U$ will be small, Eq. (4.32) can be linearized to give

$$\frac{U^{0,1}}{\gamma_{UU}^{0,1}} = \frac{-\left(U^{0,0}\right)^2}{s + 2\gamma_{UU}^{0,0} U^{0,0}} . \tag{4.33}$$

Eq. (4.33) shows that under the SDR model, the frequency response of the single-modulated signal $\Delta PL\big|_{\omega_M}$ is described by a single pole equal to $2\gamma_{UU}^{0,0} U^{0,0}$.

We turn now to the double-modulated signal $\Delta PL|_{\omega_L,\omega_M}$. By expanding Eq. (4.30) in a Fourier series, it can be shown that $\Delta PL|_{\omega_L,\omega_M} = |S^{1,1}|$ falls at least as fast with $\omega_L$ as does $U^{1,0}$. By linearizing Eq. (4.32) under double modulation, we obtain

$$\frac{U^{1,0}}{G_U{}^{1,0}} = \frac{1}{s + 2\gamma_{UU}^{0,0} U^{0,0}} \tag{4.34}$$

where $s = i\omega_L$. Comparing Eq. (4.34) to Eq. (4.33) then shows that under the SDR model, the double-modulated signal $\Delta PL|_{\omega_L,\omega_M}$ must fall at least as fast with $\omega_L$ as the single-modulated signal $\Delta PL|_{\omega_M}$ does with $\omega_M$. In contrast, the TPQ model predicts a double-modulated signal that is a constant independent of $\omega_L$ for high $\omega_L$. The SDR model prediction shown in Fig. 4.5 is a conservative estimate, where $\Delta PL|_{\omega_L,\omega_M}$ is described by the same single pole that describes $\Delta PL|_{\omega_M}$.

## 4.4 Experimental Design and Results

Fig. 4.3 shows the experimental setups, described in Ref. [93], for measuring the dependence of the single-modulated signal $\Delta PL|_{\omega_M}$ on the microwave angular frequency $\omega_M$, and the dependence of the double-modulated signal $\Delta PL|_{\omega_L,\omega_M}$ on the optical angular frequency $\omega_L$.

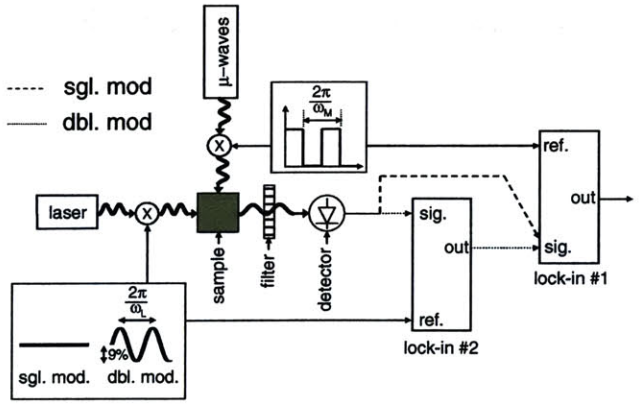


Figure 4.3 - The experimental setup for measuring the frequency response of the photoluminescence-detected magnetic resonance. The single-modulation result is measured with a single lock-in amplifier and microwave power modulation only, using the dashed signal path. The double-modulation result is measured with two lock-in amplifiers and both laser power and microwave power modulation, using the dotted signal path. Reproduced from Ref. [93].

The sample was prepared by evaporating MEH-PPV films from a 3:7 THF:toluene solvent onto the inner walls of a glass capillary that was then evacuated and sealed. The MEH-PPV was illuminated by the $\lambda = 488$ nm line of an $Ar^+$ laser with an intensity of 500 mW/cm$^2$ and subjected to spin-1/2 resonance conditions at X band ($\approx$9.35 GHz) at $T = 20$K. In the first experiment, the microwave field was square-wave modulated at $\omega_M$ and the $\omega_M$-component of the PL from the sample was measured by a lock-in amplifier. In the second experiment, in addition to this microwave modulation, the $Ar^+$ laser was sinusoidally modulated with amplitude ±8.8%. Two lock-in amplifiers were used in series, the first referenced to the modulation frequency $\omega_L$ of the laser and the second to $\omega_M$. The time constant of the first lock-in was set to 1 ms, small enough to allow through the $\omega_M$ sidebands on the $\omega_L$ 'carrier'

signal, although some sideband attenuation is introduced, and is corrected for in the data presented here. The frequency $\omega_M$ was varied in the first experiment, but held constant at $\omega_M = 2\pi \times 200$ Hz in the second experiment.

Figures 4.4 and 4.5 show the data reported previously in Ref. [93] for the single-modulation and double-modulation experiments, respectively. In both experiments the resonance was centered at 3.3 kG with a FWHM of 13 G, indicating the same resonance was observed. The single-modulation data for MEH-PPV in Fig. 4.4 is fit poorly by a single pole, (dotted line, Fig. 4.4). Much better fits are obtained using two poles (not shown), corresponding to lifetimes of 24±3 μs and 244±66 μs, suggesting that at least two species participate in the resonance together with SEs. The presence of two lifetimes is consistent with Eqs. (4.10), (4.23) and (4.24). These lifetimes may be directly assigned to TEs and polarons if these species are independent, however, in a coupled system such as the TPQ model of Eqs. (4.23) and (4.24), extraction of the TE and polaron lifetimes requires knowledge of the strength of the coupling between $T$ and $P$; see Part IV below.

The contrast between the band-limited frequency response of the single modulation case and the frequency-independent double modulation data of $\Delta PL|_{\omega_L,\omega_M}$ in Fig. 4.5 is a clear demonstration that spin-dependent polaron recombination (SDR) cannot be the origin of the PLDMR.[93] The expected response under the SDR model is shown in Fig. 4.5, normalized to the first data point (see Appendix II) and using the lifetime of the single-quencher fit in Fig. 4.4.

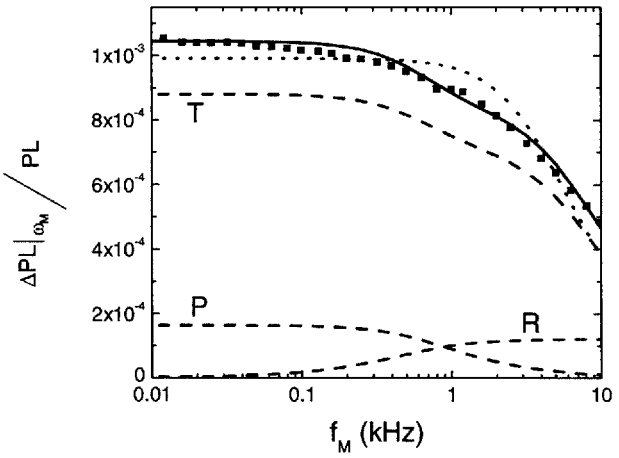


Figure 4.4 - Single modulation data (squares) for MEH-PPV as a function of microwave modulation frequency $2\pi f_M = \omega_M$. *PL* is average photoluminescence. The unlabeled solid line is the TPQ model fit to the data, given by Eqs. (4.10), (4.23) and (4.24), with triplet exciton (TE), paired and unpaired polaron lifetimes of 25±3 μs, 325±40 μs and 8.6±1.8 ms, respectively. The dashed lines break out contributions to the fit: T, P and R are the contributions of TE quenching of singlet excitons (SEs), paired polaron quenching of SEs and SE generation due to TE-induced recombination of paired polarons, respectively. The dotted line shows a single-pole fit. Frequency response data from Ref. [93].

Both TEs and polarons are expected to quench singlet excitons. Under the TPQ model, we tentatively identify the dominant quencher in MEH-PPV to be TEs based on a measurement by Wei *et. al.*[102] showing that the spectral overlap of the microwave-induced TE photoabsorption with the photoluminescent spectrum of MEH-PPV is much greater than the corresponding polaron overlap. Thus, from Eq. (4.25) the flat response in Fig. 4.5 in the frequency range 1 kHz $< f_L <$ 100 kHz requires that over this range,

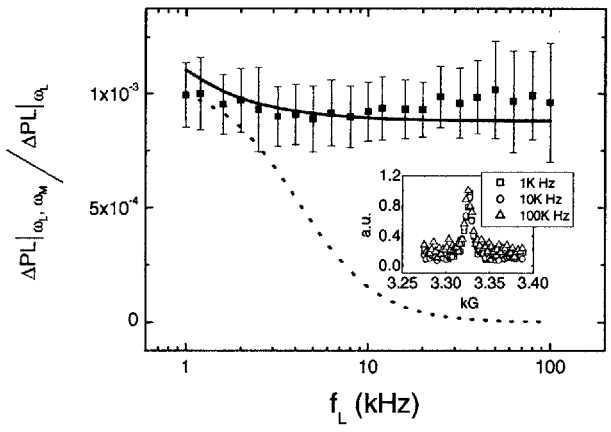


Figure 4.5 - Double modulation data for the same MEH-PPV sample as in Fig. 4.4 as a function of laser modulation frequency $f_L = \omega_L / 2\pi$, with $f_M = \omega_M / 2\pi$ held constant at 200 Hz. The solid and dotted lines are the predictions of the TPQ and SDR models respectively. The SDR model prediction has been scaled to fit the data, and uses the single-lifetime fit of Fig. 3. The TPQ model prediction has been scaled down in magnitude by 16% to fit the data, and uses Eqs. (4.25), (4.27) and (4.28), with triplet exciton (TE), paired and unpaired polaron lifetimes of 25±3 μs, 325±40 μs and 8.6±1.8 ms, respectively. **Inset**: $\Delta PL|_{\omega_L,\omega_M} / PL|_{\omega_L}$ lineshapes as a function of magnetic field for $f_L$ = 1 kHz, 10 kHz and 100 kHz are similar. Frequency response data from Ref. [93].

$$\mathrm{Re}\left\{\frac{\boldsymbol{T}^{1,0}}{\boldsymbol{T}^{0,0}}\right\} \ll \frac{\boldsymbol{G}_S^{1,0}}{\boldsymbol{G}_S^{0,0}}, \tag{4.35}$$

*i.e.* the in-phase optical modulation depth of the dominant quencher (TEs) at $f_L > 1$ kHz must be much less than the modulation depth of the optical pump (8.8%). Optical modulation of the quenching species in the absence of microwave modulation is examined in Fig. 4.6, which shows the results of a PA measurement of a drop-cast MEH-PPV film at $T$ =

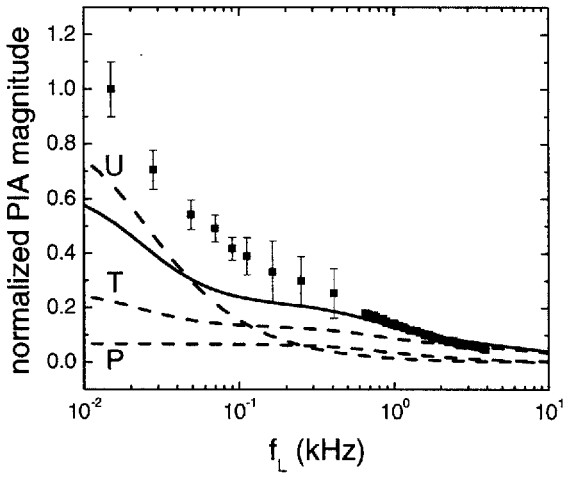


Figure 4.6 - Normalized photoinduced absorption (PA) magnitude measurement as predicted by the TPQ model (unlabeled solid line) and measured (points). The dashed lines break out contributions to the fit: T, P and U are the triplet exciton (TE), paired polaron, and unpaired polaron contributions, respectively. The T, P and U lifetimes as fit by the TPQ model are 25±3 μs, 325±40 μs and 8.6±1.8 ms, respectively. PA data from Ref. [93]. The data has been normalized to the model prediction at $f_L$ = 1660 Hz. The small-signal approximation for the modulation of $U$ breaks down at low frequencies.

20 K. The change in absorption by the sample of a probe laser on application of a $\lambda = 405$ nm pump laser was measured as a function of the pump chop frequency. The probe wavelength, $\lambda = 808$ nm, was selected to be as close as practical to the PL spectrum of MEH-PPV, thereby detecting quenchers with the best overlap with SEs, while also minimizing cross talk from optically modulated MEH-PPV PL.[93] The pump and probe lasers had intensities of 5 mW/cm$^2$ and 150 mW/cm$^2$ respectively.

The PA data measures the summed frequency responses of the absorption of $U$, $P$ and $T$ and $\lambda = 808$ nm. A good fit to the frequency response of the PA requires two poles. Least squares fits yield lifetimes of 325±40 μs and 8.6±1.8 ms, where the error bars indicate a least squares error 10% greater than optimum. Comparing Eqs. (4.23) and (4.24) to Eqs. (4.27) and (4.28), the PA and single-modulation microwave response are expected to share two poles in common. This is indeed observed in the data: the pole corresponding to the 325±40 μs lifetime measured from the PA data is consistent with the 244±66 μs lifetime extracted from the microwave data. The highest frequency pole corresponding to the 24±3 μs lifetime in the single modulated microwave resonance data is also expected to be present in the PA data (see Eqs. (4.27) and (4.28)), but the PA data lacks sufficient signal to noise to resolve this high frequency pole. In contrast, the low frequency pole corresponding to the 8.6±1.8 ms lifetime is definitively not observed in the single modulated microwave resonance data of Fig. 4.4. Under the TPQ model, the long 8.6±1.8 ms lifetime results from the interaction of TE and SEs with unpaired polarons, the population of which is not affected by magnetic resonance. Figs. 4.4 and 4.6 thus confirm the appearance of the three distinct species $P$, $T$ and $U$ described in Part II above. These species are quantitatively analysed in Part V below. Note that PA results consistent with those shown in Fig. 4.6 were also obtained by Smilowitz *et. al.*, who measured the same absorption trend as in Fig. 4.6 at low frequencies in neat films of MEH-PPV, but measured a one-pole PA response when unpaired polaron formation was frustrated in a low density mixture of MEH-PPV in a polyethylene matrix.[110]

Slow dynamics of unpaired polarons within MEH-PPV are further examined in Fig. 4.7, which shows the slow transient PL response of a drop-cast MEH-PPV film at $T = 20$ K in

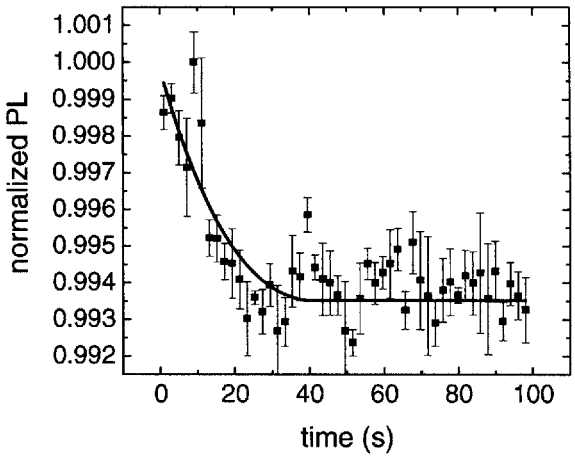


Figure 4.7 – Long-lived unpaired polarons are responsible for the slow transient response of the photoluminescence of a drop-cast MEH-PPV film at T = 20 K. The solid line is a guide to the eye.

response to laser excitation at $\lambda$ = 408 nm. The steady-state quenching magnitude of the transient data in Fig. 4.7 defines the steady-state population of unpaired polarons, $U_0$, *i.e.*:

$$U_0 = 0.6\%/(\gamma_{SP}\tau_S). \tag{4.36}$$

The transient lifetime in Fig. 4.7 ($\approx$11 s) is three orders of magnitude longer than the linearized steady state small signal lifetime 8.6±1.8 ms, extracted from the low frequency pole in the PA data. This discrepancy is likely due to the presence of fast bimolecular decay processes in steady state.

Finally, Fig. 4.8 shows the double-modulation resonance lineshape detected at the second light harmonic at $f_L$ = 10 kHz, i.e., $\Delta PL|_{2\omega_L,\omega_M}$ normalized to $\Delta PL|_{2\omega_L}$. A second harmonic signal is expected if bimolecular processes are involved in the resonance, as is the case for both SDR and TPQ models. Under the TPQ model, if polaron quenching of SEs and

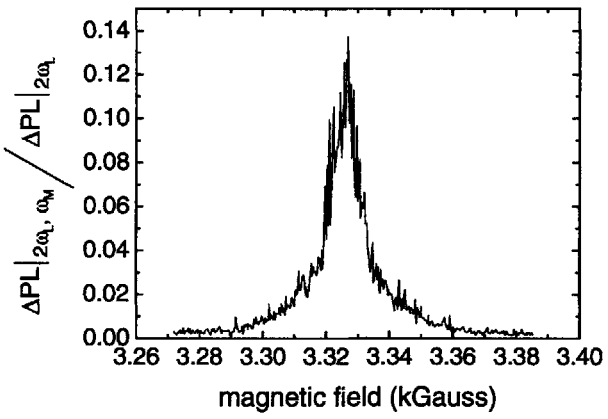


Figure 4.8 – Double-modulated resonance lineshape detected at the second light harmonic frequency with $f_L = \omega_L / 2\pi = 10$ kHz. A second harmonic signal is expected under the TPQ model. If polaron quenching of singlet excitons (SEs) and SE generation by triplet exciton (TE)-induced recombination of polaron pairs are small relative to SE-TE interactions, then $\Delta PL|_{2\omega_L,\omega_M} / \Delta PL|_{2\omega_L}$ gives the modulation depth of the TE population under microwave drive.

SE generation by TE-induced recombination of polaron pairs are small relative to singlet-TE interactions, then $\Delta PL|_{2\omega_L,\omega_M} / \Delta PL|_{2\omega_L}$ gives the modulation depth of the TE population under microwave drive.

**4.5 Analysis**

We now evaluate the parameters in the TPQ model for consistent fits to the data in Figs. 4.4-4.7. Note that the fits shown above in Figs. 4.4 – 4.6, and below in Fig. 4.7, represent a *single* set of consistent parameters in the TPQ model, and not separate fits. In this section the method for calculating the parameters of this single fit are detailed.

Beginning with the PA data, we require two poles, $p_{A1}$ and $p_{A2}$, a zero, $z_A$, and some scaling factor, $c_A$, for a good fit:

$$PA = c_A \frac{(s+z_A)}{(s+p_{A1})(s+p_{A2})}. \tag{4.37}$$

A least squares fit returns the values $p_{A1} = 3079$ rads/s, $p_{A2} = 117$ rads/s, and $z_A = 433$ rads/s. TEs, and paired and unpaired polarons will contribute to the PA data so that

$PA \propto \gamma_{ST}\boldsymbol{T}^{1,0} + \gamma_{SP}\left(\boldsymbol{U}^{1,0} + \boldsymbol{P}^{1,0}\right)$, where the triplet absorption of the pump probe relative to the polaron absorption has been taken to be $\gamma_{ST}/\gamma_{SP}$. This expression is used to calculate the predicted PA in Fig. 4.6. For the purposes of obtaining fit parameters, however, we assume that the TEs dominate the PA. This is a reasonable assumption since overlap between TEs and edge

of the MEH-PPV PL spectrum at $\lambda$ = 808 nm is greater than the corresponding overlap with polarons.[102] In addition the slow response of $U$ minimizes its contribution at high frequencies. We find the assumption that the PA is proportional to $\boldsymbol{T}^{1,0}$ produces fit parameters that change little when $U$ and $P$ are also considered. We also note that the three poles of the PA frequency response are not changed by the relative absorption strengths of $T$, $P$ and $U$ under the TPQ model.

The PA measurement is performed at low frequencies ($f_L < 4$ kHz). Because we expect the TE lifetime $\tau_T < 100$ μs, and we see only two poles in the PA, we set $dT/dt \approx 0$ for the

purposes of determining fit parameters from the PA data. Then Eqs. (4.11), (4.12) and (4.13) can be solved to give a two-pole expression for $\boldsymbol{T}^{1,0}$:

$$\mathbf{T}^{1,0} \approx \frac{-T_U G_U (s+1/\tau_P) - T_P G_P (s+1/\tau_U)}{T_T (s+1/\tau_U)(s+1/\tau_P)}, \tag{4.38}$$

where it has been assumed that TE-polaron quenching is negligible compared to the TE and polaron decay rates $1/\tau_T$, $1/\tau_P$ respectively. Then, by comparing Eqs. (4.37) and (4.38), we identify

$$\tau_P = 1/p_{A1}, \tag{4.39}$$

$$\tau_U = 1/p_{A2}. \tag{4.40}$$

The single-modulation data $\Delta PL|_{\omega_M}/PL$ of Fig. 4.4 requires two poles, $p_{M1}$ and $p_{M2}$, a zero, $z_M$, and some scaling factor, $c_M$ for a good fit:

$$\Delta PL|_{\omega_M}/PL = c_M \frac{(s+z_M)}{(s+p_{M1})(s+p_{M2})}, \tag{4.41}$$

A least squares fit returns the values $p_{M1} = 4101$ rads/s, $p_{M2} = 41393$ rads/s, and $z_M = 5148$ rads/s. While under the TPQ model, $p_{M1}$ and $p_{A1}$ are the same pole (see Part II) and are measured to be within error of each other (see Part III), superior fits are obtained using their distinct fit values.

Assuming that TEs dominate the quenching and by comparing Eqs. (4.41) and (4.24), we obtain a set of simultaneous equations that can be solved for $P_0$, $T_0$, and $\tau_T$:

$$T_T + P_P = p_{M1} + p_{M2} \tag{4.42}$$

$$P_P T_T - T_P P_T = p_{M1} p_{M2} \tag{4.43}$$

$$\frac{P_P T_\gamma - P_\gamma T_P}{T_\gamma} = z_M \,. \tag{4.44}$$

The left hand sides of Eqs. (4.42), (4.43) and (4.44) are related to $P_0$, $T_0$, and $\tau_T$ in Appendix I. Finally, by equating the zeros of Eqs. (4.37) and (4.38), we can solve for $G_U$

$$G_U = \frac{G_P T_P \tau_P (1 - \tau_U z_A)}{T_U \tau_U (\tau_P z_A - 1)} \,. \tag{4.45}$$

The parameters $\tau_P$, $\tau_U$, $\tau_T$, $P_0$, $T_0$ and $G_U$ are therefore set directly by the four poles and two zeros of the single-modulation and PA data. The singlet generation rate is calculated to be $G_S = 6 \times 10^{22}$ cm$^{-3}$/s based on an absorption length in MEH-PPV of 20 μm[111,112] and an optical intensity of 500 mW/cm$^2$ measured at the sample. In fitting the data here, we use literature values for the following parameters: $\chi_S = 0.25$,[22] $\gamma_{ST} \approx 1 \times 10^{-9}$ cm$^{-3}$/s[105] at $T = 10$ K, $\tau_S = 500$ ps,[113] and the intersystem crossing $G_T / G_S = 1\%$.[114] This leaves three free parameters to match the shape of the measured frequency responses: $\gamma_{SP}$, $\gamma_{TP}$, and $G_P$. Fitting yielded a polaron generation rate $G_P / G_S = 2.3\%$, a singlet-polaron quenching rate $\gamma_{SP} = \gamma_{ST} / 22$, and a TE-polaron annihilation rate $\gamma_{TP} = 3 \times 10^{-15}$ cm$^{-3}$/s. The low $\gamma_{SP}$ value is consistent with the relatively small spectral overlap of polarons with the PL spectrum of MEH-PPV.[102] The fitted $\gamma_{TP}$ value is smaller than the TE-polaron interaction rate measured by Greenham *et. al.*, which was $3 \times 10^{-14}$ cm$^{-3}$/s at $T = 10$ K in poly(2-methoxy-5-(3',7'-dimethyl)-octyloxy-*p*-phenylenevinylene) (OC1C10-PPV).[79] The TE-polaron interaction rate is expected to be material dependent; the presence of defect or traps reduces TE and polaron diffusion rates, lowering $\gamma_{TP}$. The change in $\gamma_{TP}$ under resonance, $\gamma^{0,1}$, required to match the magnitude of $\Delta PL|_{\omega_M} / PL$ was found to be 19%.

From Eqs. (4.39) and (4.40), we calculate $\tau_P = 325\pm40$ $\mu$s and $\tau_U = 8.6\pm1.8$ ms, where the error bars indicate a least squares error 10% greater than optimum. From Eq. (4.36), we calculate $U_0 = (2.6\pm0.2)\text{x}10^{17}$ cm$^{-3}$. From Eqs. (4.42) through (4.44), we calculate $\tau_T = 25\pm3$ $\mu$s and find $T_0 = 3.3\text{x}10^{17}$ cm$^{-3}$ and $P_0 = 1.6\text{x}10^{17}$ cm$^{-3}$. Finally, from Eq. (4.45), we find $G_U$ / $G_S$ = 0.8%. The resulting fits using Eqs. (4.10), (4.23), (4.24), (4.25), (4.27) and (4.28) are shown as solid lines in Figs. 4.4, 4.5 and 4.6, and are in good agreement with the data. We note that large changes in the unpaired polaron population $U$ occur under low frequency optical modulation, and the small-signal approximation used in the analysis in Section II breaks down.

The reason for the flat DM-PLDMR signal can now be understood using the TPQ theory. In the fit presented above, triplets are the dominant quencher in MEH-PPV due to their large population (twice the population of paired polarons), and their strong overlap with SE emission, both as indicated by the fit value of singlet-triplet interactions ($\gamma_{ST}/\gamma_{SP}$ = 22) and by literature.[102] Triplets are, however, very weakly modulated by changes in light power: with the model parameters listed above, an 8.8% modulation in the light power produces only a 1.6% modulation in the triplet population at low modulation frequency. This weak modulation results from the fact that increased light power also produces more polarons, which quench triplets. The weak response of the triplets to light modulation ensures that the dominant quenching interaction under double-modulation conditions is the annihilation of light-modulated SEs by the steady state population of TEs, which is independent of $\omega_L$. The requirement for a flat DM-PLDMR, Eq. (4.35), is satisfied. The resulting predicted

$\Delta PL|_{\omega_L,\omega_M} / \Delta PL|_{\omega_L}$ magnitude under the TPQ model matches the measured data to within 16% across the entire measured frequency range.

### 4.6 Discussion

As noted in Ref. [93], the observation of almost constant $\Delta PL > 0$ in the double-modulation experiments (Fig. 4.5) up to $f_L$ = 100 kHz rules out spin-dependent recombination models, since the lifetimes of both polarons and TEs are too long to follow the optical modulation. In quenching models, by contrast, $\Delta PL$ depends on SEs. Our quantitative application of the TPQ model is, however, limited by familiar difficulties such as the wealth of possible bimolecular excitonic processes and the limited knowledge of rate parameters. We have taken rates from previous work whenever possible, and since charges are probably trapped at T = 20 K, we have neglected *P-U* interactions, leaving three free parameters to match the shape of the measured responses ($\gamma_{ST}$, $\gamma_{TP}$ and $G_P$) and a single parameter ($\gamma^{0,1}$) to scale the predicted $\Delta PL|_{\omega_M} / PL$ magnitude. Below, we first summarize other observations that are consistent with the TPQ model. We then comment on the novel aspects of TE-paired-polaron collisions in Fig. 4.2 and on the important parameter $\chi_S$ for the fraction of polarons that recombine as singlets.

In further support of the TPQ model, we note that: (i) Resonances originating in TE-polaron collisions have been previously observed in fullerenes.[115-117] (ii) the TPQ model is consistent with the trends in the densities of SEs, TEs, and polarons observed in PADMR.[28,55,80,95,96] (iii) The TPQ model is consistent with electroluminescence detected magnetic resonance signals that are anomalously small under the spin-dependent polaron

recombination model.[22,81,82,118,119] (iv) Since TE-polaron interactions are independent of molecular weight, the TPQ model is also consistent with the PL- and EL-enhancing resonances in small molecular weight materials such as tris(8-hydroxyquinoline) aluminum ($Alq_3$).[118] (v) The TPQ model is consistent with a measured singlet ratio of (20±4)% in MEH-PPV.[22] (vi) Because a spin-1 resonance mixes TE spin sublevels, it will also increase the rate of TE-polaron collisions. The observation of both spin-1/2 and spin-1 resonances in ODMR is therefore consistent with the TPQ model. (vii) Other published measurements of the frequency response of the spin-1/2 PLDMR also exhibit a two-lifetime behavior consistent with the TPQ model (see Eqs. (4.10), (4.23) and (4.24)), including MEH-PPV,[97] 2,5-dioctoxy PPV (DOO-PPV),[98] PPV,[99] methyl-bridged ladder-type poly(*p*-phenylene) (m-LPPP),[29,104] and 2,5-dibutoxy poly(p-phenylene ethynylene) (DBO-PPE).[100] Finally, (viii) the TPQ mechanism is, to our knowledge, the only mechanism that can account for the positive spin-1/2 electrically-detected magnetic resonance (EDMR) observed in current flow through polymeric and small-molecular OLEDs under bias.[81,118] We speculate that the increase in current under resonance is due to polarons that are excited or detrapped by interactions with TEs.

Although there are numerous precedents for spin-dependent TE-polaron annihilation, no special role has been proposed for the excited polaron that is generated. Rapid vibronic relaxation to the electronic ground state is expected. For a TE collision with a paired polaron at low $T$, as sketched in Fig. 4.2(b), excitation can also promote recombination. The contribution of this recombination process to $\Delta PL|_{\omega_M} / PL$ with the present parameters is labeled "R" in Fig. 4.4. This novel $\gamma_{TP}$ process in Eq. (4.11) is an additional mechanism

coupling the TE and polaron populations. The steady-state populations are thus strongly coupled in our analysis.

The steady-state values for $P$, $T$ and $U$ listed in Part V above are calculated from Eqs. (4.39) through (4.44), rather than from the rate equations for those species, Eqs. (4.11) - (4.13), which may not produce accurate steady-state values because they do not include bimolecular interactions that are important at high densities. Solving for the steady-state values from the rate equations gives $P_0 = 4.4\times10^{17}$ cm$^{-3}$, $T_0 = 3.7\times10^{16}$ cm$^{-3}$, and $U_0 = 4.3\times10^{18}$ cm$^{-3}$, as compared to the linearized fit values $P_0 = 1.6\times10^{17}$ cm$^{-3}$, $T_0 = 3.3\times10^{17}$ cm$^{-3}$ and $U_0 = (2.6\pm0.2)\times10^{17}$ cm$^{-3}$. In our experiments, we have $S = 3\times10^{13}$ cm$^{-3}$ and since SE-SE annihilation is less than 1% of $G_S$ for a typical $\gamma_{SS} = 10^{-8}$ cm$^{-3}$/s,[1] we have not included this term in Eq. (4.7).

We have used $\chi_S = 0.25$, the statistical value for recombination of spin-1/2 polarons into SEs, but the present data do not constrain this interesting parameter directly. There is an indirect connection, however, since $\chi_S > 0.25$ has been inferred from $\Delta PL$ measurements on conjugated polymers at low temperature, including MEH-PPV, that were analyzed in terms of faster polaron recombination under resonance conditions. Theoretical arguments for $\chi_S > 0.25$ have been advanced for such recombination,[28,80,95] motivated by these data. Quenching models that include spin-dependent TE-polaron processes account for $\Delta PL > 0$ without so far having to invoke $\chi_S > 0.25$.

Finally, the success of the TPQ model does not rule out the existence of other relevant spin-dependent quenching mechanisms. For example, radiationless charge recombination to the singlet ground state is spin dependent [120], and will lower polaron quenching of singlet

excitons. This latter process is of minimal importance in electroluminescence, but may be significant in photovoltaic cells.

### 4.7 Conclusion

The TE-polaron quenching (TPQ) model ascribes the photoluminescence-detected magnetic resonance to a reduction in the singlet quenching rate caused by an increased rate of TE-polaron collisions under resonance. The TPQ model can fully account for the measured photoinduced absorption, single-modulation PLDMR, and double-modulation PLDMR frequency responses of the archetypal $\pi$-conjugated polymer MEH-PPV. With just four free parameters, the TPQ model successfully reproduces the shapes of these three independent frequency responses over decades of frequency, as well as the magnitudes of the two PLDMR frequency responses. A frequency analysis of the spin-dependent polaron recombination model confirms that it cannot account for these measurements.[93] The flat double-modulation PLDMR frequency response is explained by the TPQ model as resulting from singlet quenching by an average quencher population.

The existence of unpaired polarons is clearly indicated by a low-frequency pole in the photoabsorption (PA) data, which is not present in the PLDMR frequency response. Using the TPQ model, we thus find three SE quenching species and their lifetimes: paired polarons with $\tau_P = 325\pm40$ μs, unpaired polarons with $\tau_U = 8.6\pm1.8$ ms and TEs with $\tau_T = 25\pm3$ μs. Paired polarons may recombine after being excited by collisions with TEs. Unpaired polarons are similarly excited by collisions with TE excitons, but are retrapped before they are able to recombine, and so are unaffected by resonance, although they may be the source of the positive spin-1/2 EDMR observed in polymeric and small-molecular weight OLEDs at low

temperatures.[81,118] Photoinduced absorption measurements modulate all three quenchers, and therefore exhibit three lifetimes, while magnetic resonance measurements do not modulate unpaired polarons and therefore exhibit only two lifetimes. Parameter values such as lifetimes and populations can be extracted from these measured frequency responses using the TPQ model.

Optically detected magnetic resonance effects are quenching phenomena, and are not related to exciton formation dynamics. The effect on exciton formation dynamics of resonant conditions, then, is minimal. This suggests that the $m_j$ = -1, 0 and +1 populations of $CT^3(m)$ states are equal even outside of resonance (Fig. 4.1), and that therefore $k_{Sm} \approx k_{Tm}$. The small size of ELDMR resonances is consistent with this conclusion, as are the results of Chapter 3. $k_{Sm} \approx k_{Tm}$ is consistent with $m > 1$ in Fig. 2.13. This is because the very different nature of the final state singlet and triplet exciton suggests $k_{S1}$ and $k_{T1}$ are not equal. The further apart are the charges of the last-mixed CT state, the more similar $k_{Sm}$ and $k_{Tm}$ are expected to be. $m > 1$ is proved in Chapter 5.

## 4.8 Comments

The work in Section 4.3 prompted a comment from Vardeny *et al*, who developed the spin dependent recombination model invalidated by Fig. 4.5. The original comment is shown here, along with our reply.

### 4.8.1 Comment on "Frequency response and origin of the spin-1/2 photoluminescence-detected magnetic resonance in a π-conjugated polymer"

C. G. Yang[1], E. Ehrenfreund[2], M. Wohlgenannt[3], and Z. V. Vardeny[1*]

[1]Department of Physics, University of Utah, Salt Lake City, Utah 84112, USA

[2]Department of Physics and Solid State Institute, Technion-Israel Institute of Technology, Haifa 32000, Israel

[3]Department of Physics and Astronomy, The University of Iowa, Iowa City, Iowa 52242-1479, USA

Segal et al. [1] reported the dynamics of spin-½ photoluminescence detected magnetic resonance (PLDMR) and photoinduced absorption (PA) in films of the archetypal π-conjugated polymer, namely poly[2-methoxy-5-(2-ethylhexyloxy)-1,4-phnylenevinylene] (MEH-PPV) at 20 K. They claimed that the frequency response of the resonance is consistent with a triplet-polaron quenching (TPQ) model, in which the resonance is mediated by spin-dependent interactions between photogenerated triplet excitons (TE) and polaron pairs in the film [1]. We measured the *full* dynamics of both spin-½ and spin-1 PLDMR resonances in MEH-PPV films as a function of microwave power at various temperatures. In this Comment we show that the TPQ model fails to explain the data. We checked that an alternative model, namely the spin dependent recombination (SDR) of polarons [2], readily accounts for the results.

In the TPQ model [1] the photogenerated TE interact with spin-paired polarons by collisions

that enhance the polaron recombination. Thespin dependence of the TE-polaron annihilation process in this model is a result of *spin conservation*. The spin subsystem of a colliding spin-1 TE and spin-½ polaron comprises of six spin-states of equal probability, in which only two have spin ½. After the TE is annihilated, the excited polaron with spin-½ remains; therefore spin conservation disallows 2/3 of TE-polaron collisions. Resonant spin-½ conditions induce rapid transitions between the spin-½ sublevels so that all TE-polaron collisions become allowed [1]. The TPQ model for explaining the spin-½ PLDMR resonance is therefore viable under two important conditions, *which may be readily checked by the experiment.* Firstly, in addition to photogenerated polaron density, a substantial density of long-lived photogenerated TE should also exist in the film; and secondly, the TE spin-lattice relaxation time should be longer than the TE-polaron collision time, so that their spin-state is not randomized before colliding with the paired polarons; in other words, the TE spin-lattice relaxation rate should be relatively small. Measuring spin-1 and spin-½ PLDMR resonance dynamics, and PA of polarons and TE at various temperatures scrutinize these two conditions as reported here.

In addition, Segal et al. [1] also calculated the microwave frequency ($f_M$) response dynamics of the spin-½ PLDMR resonance based on the TPQ model (Eq. (26) in ref. [1]); and used it to fit the experimental PLDMR dynamics. Alas, only the magnitude ($|\Delta PL|$) of the spin-½ PLDMR frequency response was measured in [1], where $|\Delta PL| = [((\Delta PL_I)^2+(\Delta PL_Q)^2]^{1/2}$, and $\Delta PL_I$ and $\Delta PL_Q$ are the in-phase and quadrature components of the change $\Delta PL$ in the photoluminescence (PL) at resonance. Thus unfortunately, important information on the PLDMR dynamics was missed; with rather severe consequences. In our PLDMR experiments we measured *both* $\Delta PL$ components vs. $f_M$ at various microwave powers to ensure that we

register the *full* dynamics of the spin-½ PLDMR resonance. When the *full* PLDMR dynamics is unraveled, then it becomes obvious that the TPQ model fails to reproduce the data. This is important since the PLDMR dynamics can disclose the underlying mechanism for the resonance, and thus the failure to reproduce the data shows that the TPQ model is irrelevant for explaining the PLDMR in π-conjugated polymers.

The PA and PLDMR measurements were conducted at various temperatures on a MEH- PPV film drop-casted from a toluene solution that was mounted in a high Q microwave cavity. The polymer film was excited with an $Ar^+$ laser at 488 nm with an intensity of ~ 500 $mW/cm^2$ subjected to spin-½ (H = 1070 Gauss) or spin-1 (at 'half field', H = 370 Gauss) resonance conditions at ~3 GHz (S-band) microwave frequency [2]. For PA measurements, an incandescent light source was used, and the changes $\Delta T$ in the transmission T caused by the laser illumination at various modulation frequency, $f_L$ were measured using phase-sensitive technique. Both the in-phase and quadrature components of $\Delta T$ were routinely recorded. For PLDMR, we measured the changes $\Delta PL$ in PL caused by the magnetic resonance, where the microwave intensity was modulated at various frequencies, $f_M$; again both the in-phase and quadrature $\Delta PL$ components were measured, where the phase, φ was set with respect to the microwave modulation. In addition, the PLDMR was studied under variable microwave power conditions, $P$ in the range 2.5 to 100 mW.

Fig. 1 shows the spin-½ PLDMR response vs. $f_M$ at 20 K and $P$ = 80 mW for the two $\Delta PL$ components; the magnitude $|\Delta PL|$ and the phase φ vs. $f_M$ were also calculated and shown for completeness. The measured $|\Delta PL(f_M)|$ response is quite similar to the response obtained in

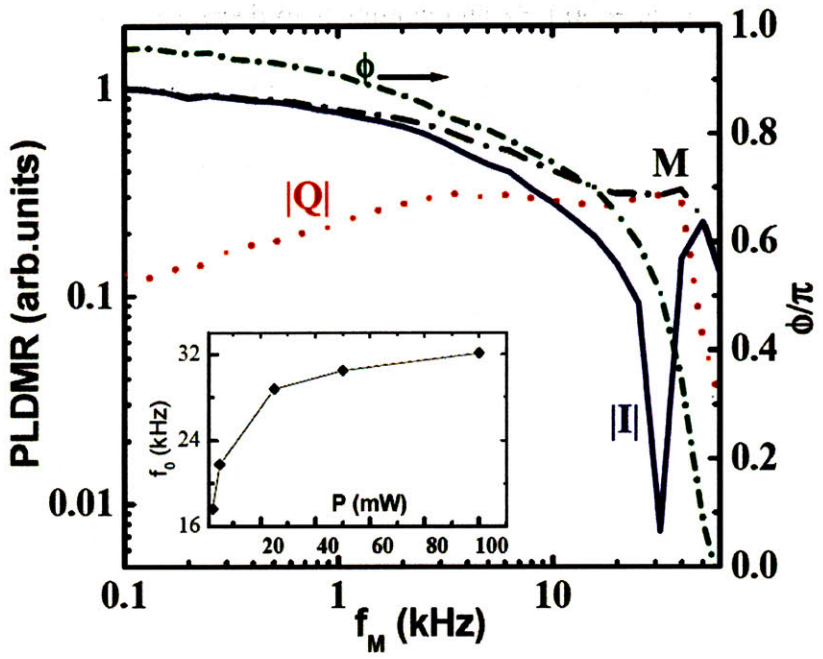


Fig. 1: The spin-½ PLDMR, ΔP vs. the microwave modulation frequency, $f_M$ for a MEH-PPV film at 20 K. The in-phase (I, blue; solid line) and quadrature (Q, red; dotted line) PLDMR components are shown separately, as well as the magnitude $|\Delta PL|$ (M, black; dash-dotted line) and the phase (Φ, green; short dash-dotted line; right scale). Note the zero crossing of the in-phase ΔPL component at $f_o \approx 30$ kHz, for microwave power $P = 50$ mW. The inset shows the dependence of $f_o$ on P.

[1] indicating that the polymer sample and resonance conditions in the two laboratories are very similar. However, by measuring the microwave modulation frequency response of both $\Delta PL$ components, an unexpected surprise is unraveled; this was completely overlooked in [1]. As seen in Fig. 1, the in-phase component $\Delta PL_I(f_M)$ changes sign at a frequency $f_0$ of about 30 kHz before decaying away at higher frequencies. Importantly, this response is unique for the in-phase component; the quadrature component retains its sign within the same experimental frequency range. The phase response $\varphi(f_M)$ shows the sign change in $\Delta PL_I(f_M)$ more clearly; it

crosses the value $\varphi = \pi/2$ at ~ 30 kHz and continues to decrease thereof as $f_M$ increases. We checked that this curious PLDMR dynamic behavior is not an artifact of the measuring set-up by changing the microwave power, $P$. Fig. 1 (inset) shows the dependence of $f_o$ with $P$. We found that $f_o$ increases with $P$, and thus cannot be an artifact. Moreover, $f_o$ changes when varying the laser excitation intensity, or when films of different polymers and semiconductors were measured. This bizarre PLDMR $f_M$-response cannot be detected when measuring only the magnitude $|\Delta PL(f_M)|$; thus the true PLDMR dynamics was completely missed in [1]. Moreover, it cannot be explained by a simple one- or two-oscillators response as introduced in [1] for $|\Delta PL|$ dynamics via the TPQ model. A much more profound understanding of PLDMR dynamic response must be involved for explaining the astonishing $\Delta PL_I(f_M)$ dynamics and its dependence on $P$ [3].

We first attempt to explain the surprising PLDMR dynamics using the TPQ model introduced in [1]. The PLDMR vs. $f_M$ response was fitted in [1] using the following two-oscillators equation for the complex $\Delta PL(f_M)$ response (Eq. (26) in ref. [1]);

$$\Delta PL(f_M)/PL = c_M(i\omega + z_{M1})/[(i\omega + p_{M1})(i\omega + p_{M2})], \quad (1)$$

where $c_M$ is a scaling factor, $\omega = 2\pi f_M$, and $z_M$, $p_{M1}$ and $p_{M2}$ are some effective decay rates, which were determined by the TPQ model. Using the best fitting parameters given in [1] we calculated the two $\Delta PL(f_M)$ components, as well as the magnitude $|\Delta PL(f_M)|$ and phase $\varphi(f_M)$ responses, as shown in Fig. 2(a). It is apparent that *the TPQ model cannot describe the data in Fig. 1*. Firstly, $\Delta PL_I(f_M)$ does not change sign; this is also seen in the $\varphi$ response that does not

decrease beyond $\varphi = \pi/2$; secondly, the two bumps in $\Delta PL_Q(f_M)$ response using Eq. (1) are not reproduced in the experimental data; and thirdly, there cannot be any dependence on the microwave power P, as seen experimentally; since Eq. (1) is independent on P. We also tried to change the parameters $z_M$, $p_{M1}$ and $p_{M2}$ in Eq. (1) so that a zero crossing occurs in $\Delta PL_I(f_M)$ response. For the unrealistic parameters $z_M > p_{M1} + p_{M2}$ there is indeed a change in sign; however, the sign change in $\Delta PL_I(f_M)$ is followed by a sign change in $\Delta PL_Q(f_M)$ as well, in disagreement with the experimental data in Fig. 1. We conclude that the TPQ model that apparently describes $|\Delta PL(f_M)|$ response in an ad-hoc manner, is, in fact inadequate to describe the complete $\Delta PL(f_M)$ response. This is significant since the full PLDMR response gives a clue as to the underlying physical process responsible for the resonance.

On the contrary, a model in which the polaron recombination is spin dependent (the SDR model [2]) describes the full PLDMR dynamic. This model, dubbed 'distant pair recombination model' has been used previously in various inorganic [3-7] and organic semiconductors [2, 8, 9]. In the SDR model polaron pairs with antiparallel spins (having population $n_1$) recombine faster than polaron pairs with parallel spins (having population $n_2$). If the polaron pairs are generated with equal initial populations, then 'spin polarization' is established by the different recombination rates of parallel and antiparallel pairs, since at steady state conditions $n_1 < n_2$. Microwave absorption reverses the spin sense of some of the polaron pairs so that at saturation $n_1 = n_2$. Therefore, the resonance conditions enhance the overall polaron recombination rate, and consequently the polaron density decreases as seen in the experiment [2]. Whether the PL increases due to reduction in polaron quenching of singlet excitons [1] or/and due to polaron pair radiative recombination [10], is a secondary question

that would depend on the polymer film nanomorphology [11]; and thus has little to do with the PLDMR kinetics. The PLDMR dynamics in the SDR model is described by a pair of rate equations given by [3]:

$$dn_1/dt = G - n_1/\tau_1 - (n_1 - n_2)/2T_{sl} - (n_1 - n_2)P \quad (2)$$

$$dn_2/dt = G - n_2/\tau_2 - (n_2 - n_1)/2T_{sl} - (n_2 - n_1)P \quad (3)$$

where G is the generation rate; $\tau_1$ and $\tau_2$ are the lifetimes of polaron pairs with spin antiparallel and parallel, respectively; and $T_{sl}$ is the polaron spin-lattice relaxation time. The coupled equations (2) and (3) were solved numerically, and the change $\Delta n$ in the polaron density due to the microwave power P was calculated in the frequency domain. The two $\Delta n$ components, namely $\Delta n_I$ and $\Delta n_Q$, as well as $|\Delta n|$ and the phase $\varphi$ were obtained as a function of $f_M$; this procedure was repeated at various P. In addition, an analytical approximate solution to equations close in form to Eqs. (2) and (3) also gives results similar to our numerical solution [12]. A typical ODMR $f_M$ -response based on the numerical calculations of Eqs. (2) and (3) is shown in Fig. 2(b); the $f_M$ dynamics was obtained with the parameters: $\tau_1$ = 14 μsec; $\tau_2$ = 60 μsec; and $T_{sl}$ = 10 μsec. In contrast to the TPQ model, it is seen that the elegant SDR model excellently describes all the PLDMR experimental response features. Firstly, the in-phase ODMR component correctly changes sign at $f_o$, followed by the phase $\varphi$ passing the value $\varphi = \pi/2$; secondly, the quadrature ODMR component is rather smooth and does not change sign; and thirdly, the calculations reproduce the increase of $f_o$ with P (Fig. 2(b) inset).

The change in sign of the in-phase ODMR is quite natural in the SDR model and does not depend on the parameters used; in fact it shows that the two spin states ($n_1$ and $n_2$) involved in the resonance have indeed different recombination rates [13]. We therefore conclude that the SDR model is capable of describing the PLDMR dynamics in full, whereas the TPQ model does not.

Next, we studied the PLDMR and PA dynamics as a function of temperature, $\theta$. Fig. 3(a) [left panel] shows the spin-½ and spin-1 PLDMR of polarons and TE, respectively, at various temperatures. Whereas the spin-1 PLDMR sharply decreases with $\theta$ indicating that the TE spin-

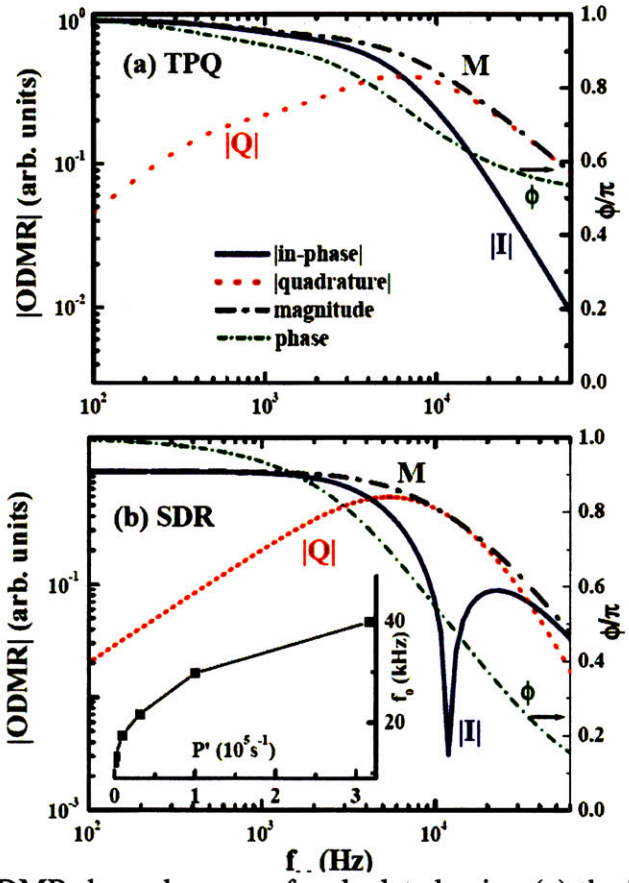


Fig. 2: The spin-½ PLDMR dependence on $f_M$ calculated using (a) the TPQ model (Eq. (1)); and (b) the SDR model (Eqs. (2) and (3)). The response of the two PLDMR components are shown together with the magnitude $|\Delta PL|$ and the phase; the color codes and symbols are as in Fig. 1. The zero crossing of the in-phase component using the SDR model reproduces the data in Fig. 1. The inset in (b) shows that the calculated zero crossing frequency, $f_0$ in the SDR model increases with the microwave power similar to the data in Fig. 1 (inset). [The abscissa in the inset, P' is proportional to the microwave power applied in the experiment, P via: $P'(1/sec) \cong 6.7 \times 10^3 P\,(mW)$].

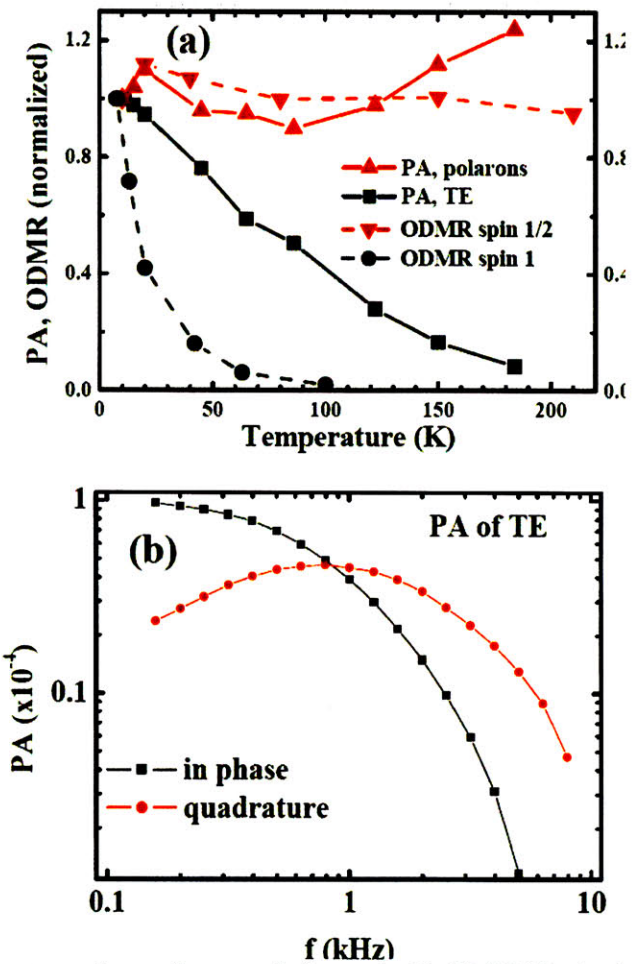


Fig. 3: (a) The temperature dependence of the spin-½ PLDMR (red triangles), and spin-1 (black circles) resonances; plotted together with the temperature dependence of the PA of polarons (red triangles) and triplet excitons (TE; black squares). (b) The PA dependence on the laser modulation frequency, $f_L$ for the TE. Both the inphase (black squares) and the quadrature (red circles) components are shown. However, the decrease in TE density with θ apparently does not have any influence on the spin-½ PLDMR resonance, or polaron PA response; in contrast to the conditions stated above for the TPQ model [1].

lattice relaxation rate dramatically increases with θ; the spin-½ PLDMR hardly changes with θ. This shows that (i) at high temperatures the TE do not conserve spins, and thus cannot participate in spin-dependent collisions between TE and polarons, as required by the TPQ model; and (ii) that the dramatic increase in TE spin-lattice relaxation rate with θ has no influence over the spin- ½ PLDMR resonance; the polaron and TE spin dynamics are simply *not correlated*, in contrast to the TPQ model [1].

Fig. 3(a) also shows the PA temperature dependence of TE measured at 1.35 eV, and polarons measured at 0.4 eV [14]. In agreement with the spin ½ PLDMR, the polaron PA hardly changes with θ. By contrast, the triplet PA decreases with θ by more than an order of magnitude up to 200 K.

Finally, we also examined the PA dynamics at low temperatures. Fig. 3(b) shows the two components of the PA vs. laser modulation frequency ($f_L$) for the TE measured at 1.35 eV. As seen the TE recombination kinetics may be described by a single time constant. From the crossover of the two PA components at $f_L \approx 800$ Hz, where $\omega\tau \approx 1$ [15] ($\omega = 2\pi f_L$, and $\tau$ is the TE lifetime) we get $\tau \approx 200$ μsec. This is about one order of magnitude longer than $\tau = 25$ μsec extracted for the TE using the TPQ model for the PLDMR and PA dynamics in [1]. This shows that the TPQ model, once again disagrees with the data.

In conclusion, by measuring the full dynamics of the spin-½ and spin-1 PLDMR as a function of microwave power and temperature, together with the PA dynamics vs. temperature, we show that the TPQ model is irrelevant for describing the PLDMR and PA responses in MEH-PPV films. In contrast, we show that a competing model, namely the spin dependent

recombination of polarons, which has been extensively used in previous publications, describes well the whole body of experimental results, and in particular the spin-½ PLDMR bizarre frequency response measured here.

## References


[1] M. Segal, M.A. Baldo, M.K. Lee, J. Shinar, and Z.G. Soos, Phys. Rev. B **71**, 245201 (2005).

[2] Z.V. Vardeny, and X. Wei, in Handbook of Conducting Polymers, T.A. Skotheim, R. L. Elsenbaumer, and J. R. Reynolds, editors, Marcel Dekker, Inc., second edition 1998, pp 639-666.

[3] E. Lifshitz, L. Fradkin, A. Glozman, and L. Langof, Annu. Rev. Chem. **55**, 509 (2004).

[4] B. C. Cavenett, Advances in Physics **30**, 475 (1981).

[5] I. Hirabayashi, and K. Morigaki, Solid State Commun. **47**, 469 (1983).

[6] J.J. Davis, J. Cryst. Growth **72**, 317 (1985).

[7] L. Langof, E. Ehrenfreund, E. Lifshitz, O.I. Micic, and A.J. Nozik, J. Phys. Chem. B **106**, 1606 (2002).

[8] Z.V. Vardeny, E. Ehrenfreund, J. Shinar, and F. Wudl, Phys. Rev. B **35**, 2498 (1987).

[9] M. Wohlgenannt, K. Tandon, S. Mazumdar, S. Ramasesha, and Z.V. Vardeny, Nature (London) **409**, 494 (2001).

[10] M. Wohlgenannt, C. Yang, and Z.V. Vardeny, Phys. Rev. B **66**, 241201 (R) (2002).

[11] B. J. Schwartz, Annu. Rev. Phys. Chem. **54**, 141 (2003).

[12] M. Wohlgenannt, and Z. V. Vardeny in "Handbook of Organic Electronics and Photonics", to be published by American Scientific Publishers (2006).

[13] C. G. Yang, E. Ehrenfreund, and Z.V. Vardeny, to be published.

[14] X. Wei, B. C. Hess, Z. V. Vardeny, and F. Wudl, Phys. Rev. Lett. **68**, 666 (1992).

[15] O. Epshtein, G. Nakhmanovich, Y. Eichen, and E. Ehrenfreund, Phys. Rev. B **63**, 125206 (2001); O. Epshtein, Y. Eichen, E. Ehrenfreund, M. Wohlgenannt, and Z.V. Vardeny, Phys. Rev. Lett. **90**, 046804 (2003).

### 4.4.2 Reply To Comment on "Frequency response and origin of the spin ½ photoluminescence-detected magnetic resonance in a π-conjugated polymer"

This comment addresses a single modulation experiment, *i.e.* the dependence of the photoluminescence-detected magnetic resonance (PLDMR) on the modulation frequency of the microwave power. It is claimed that transient microwave modulation is technically superior to double modulation. It is also claimed that triplet-polaron collisions cannot account for the measured phase, microwave power, and temperature dependencies. We address each new claim by Yang, *et al.* [121], in order of seriousness.

**(i) The Transient Response of PLDMR in MEH-PPV**

In their comment Yang *et al.* [121], argue on experimental grounds that the double modulation technique is 'insensitive' and 'has been abandoned in favor of the time-resolved ODMR, which is more powerful'. Subsequently, Yang, *et al.* [121] employ time-resolved PLDMR to measure the response of the photoluminescence to microwave modulation. Now, the response of PLDMR to microwave modulation is typically measured in the frequency domain. The technique is familiar from amplitude modulation (AM) in communication systems. It effectively takes advantage of bandpass filtering to reduce noise. Indeed Yang *et al.* [121] use this technique and measure the frequency response of PLDMR in Fig. 1 of their comment. We used the same technique and obtained nearly identical data in Fig. 3 of Ref. [122], replotted for comparison here in Fig. 1.

In their transient PLDMR experiment, however, the response of PLDMR to microwave modulation is measured in the time domain, rather than the frequency domain.

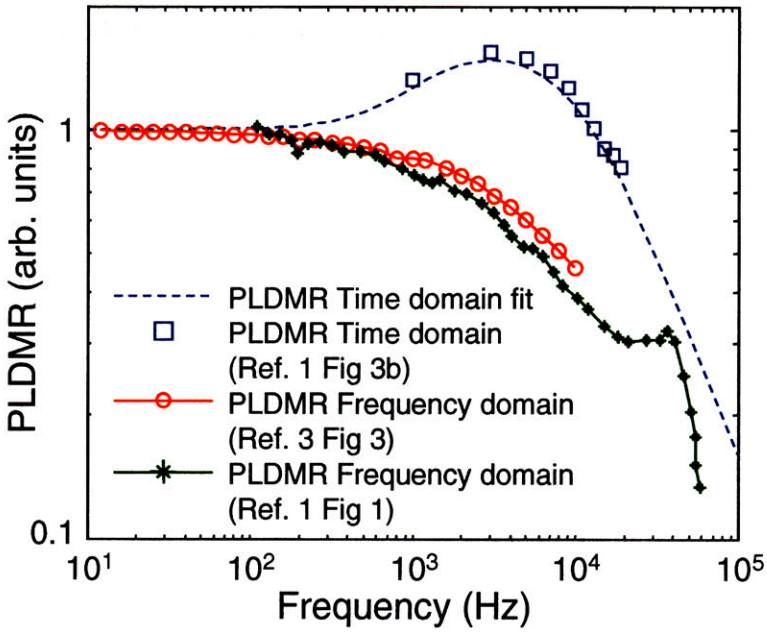


Fig. 1. A comparison of the frequency response of the PLDMR signal in MEH-PPV to modulation of the microwave power. Data measured in the frequency domain is similar and overdamped. Taken from the Yang, *et al.*[121] and Ref. [122]. Lines linking data points recorded in the frequency domain are guides to the eye. In contrast, the data measured in the time domain appears underdamped. The frequency response of the data measured in the time domain was obtained by performing a Fourier transform on the transient response in Yang, *et al.*[121] Fig. 3b. The dashed line fitting the frequency response of the data measured in the time domain is obtained using a zero at 800 Hz and two poles at 1.3 kHz and 10 kHz, respectively.

Thus, Yang *et al.* [121] have performed the same measurement twice: once in the frequency domain (Ref. [121], Fig. 1), and once in the time domain (Ref. [121], Fig. 3b). Yet, it is evident that the frequency response is overdamped while the transient step response appears underdamped. Compare, for example, the overshoot in the step response of Ref. [121], Fig. 3b and the frequency response roll-off in Ref. [121], Fig. 1. The apparent inconsistency is

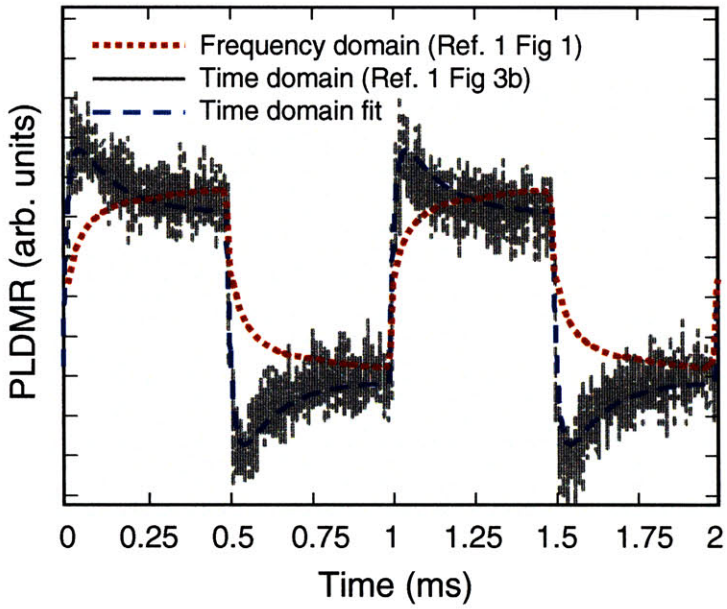


Fig. 2. In their comment, Yang, *et al.*[121] measured the microwave frequency response of the spin-1/2 resonance in MEH-PPV in two different ways: once in the time domain (Fig. 3b of Ref. [121]), and once in the frequency domain (Fig. 1 of Ref. [121]). Here, we compare the measurements in the time domain by taking the inverse Fourier transform of the frequency response data and convolving it with a 1 kHz square wave, to represent the microwave modulation. Note that the reported transient data and the frequency domain data are inconsistent. The transient data appears underdamped[123] and the frequency response is overdamped. Note also that the frequency domain data exhibits much lower noise, consistent with the expected superiority of the frequency domain approach. We also plot a fit to the transient data obtained using a zero at 800 Hz and two poles at 1.3 kHz and 10 kHz, respectively. The frequency response of this fit is shown in Fig. 1. It appears underdamped and does not match the overdamped response of the data measured in the frequency domain.

confirmed in Fig. 2, by performing a Fourier transform on the transient response or an inverse Fourier Transform on the frequency response data of Yang *et al.* [121] Note also that the transient data is much noisier. This disproves claims that the transient measurement is a superior technique. It is instead a redundant method for determining the frequency response of PLDMR to microwave modulation.

Finally, note that the frequency-domain PLDMR matches the photo-induced absorption detected magnetic resonance (PADMR) relatively well, as seen in Fig. 3. This is expected under a quenching model.

**(ii) The Phase and Microwave Power Dependencies of the Resonance**

In our original work, we sought to explain the flat frequency response under double modulation conditions [122,124]. Neither the response of the system to microwave modulation at very high frequencies nor the response to variations in microwave power was relevant. Consequently, magnetic sublevels were ignored. We emphasized [122,124] that single-modulation results can usually be fit by either triplet-polaron quenching (TPQ) or spin dependent recombination (SDR), even though the models are different, because all the relevant excitations, their concentrations, and various microscopic rates are not known accurately enough. This was the principal reason for using double modulation to demonstrate the participation of singlet excitons in PLDMR.

In their comment, Yang *et al.* [121] cite several apparent failures of the TPQ model that are due to the neglect of magnetic sublevels. It is straightforward to demonstrate that the TPQ

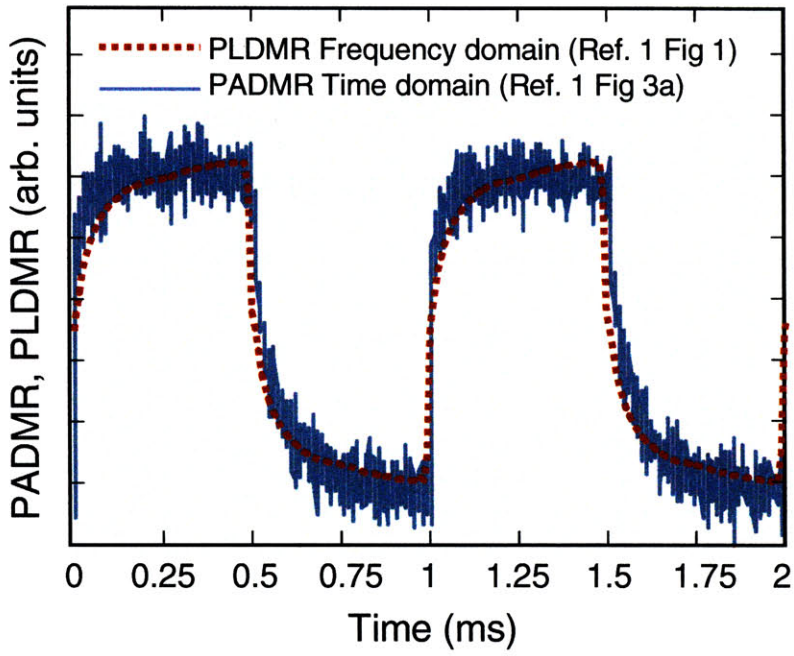


Fig. 3. In contrast to the apparent inconsistency of the data in Fig. 2, here we compare the PLDMR frequency response data to the transient PADMR data; both from Ref. [121]. Although the transient technique is again much noisier, the responses are relatively similar, and both are overdamped. The similarity provides evidence for the quenching basis of PLDMR.

model can exhibit the correct phase and power dependencies when magnetic sublevels are introduced. Consider the interaction of a polaron and a triplet exciton. If the triplet exciton is to be annihilated, the total spin of the combination must be ½. We label the three triplet states as $T^{+1}$, $T^{0}$, and $T^{-1}$, and the polaron states as $P^{+1/2}$ and $P^{-1/2}$. Interactions between $T^{0}$ and polarons do not change under spin ½ resonance. But the $T^{+1}$ triplet, for example, can only interact with a $P^{-1/2}$ polaron. So let $n_1$ be the population of $T^{+1}/P^{-1/2}$ and $T^{-1}/P^{+1/2}$ (antiparallel) pairs and $n_2$ be the population of $T^{+1}/P^{+1/2}$ and $T^{-1}/P^{-1/2}$ (parallel) pairs. Parallel pairs can only decay via the natural triplet decay process, which is very slow. But antiparallel pairs can decay via either collisions or natural decay, so there are different lifetimes for $n_1$ and $n_2$. Then

when we introduce the microwave power and spin-lattice relaxation, we get rate equations of the same form as the SDR model, yielding the same phase and microwave power dependencies [123].

**(iii) The Temperature Dependence of PLDMR**

The simplest model for singlet exciton quenching by triplets or polarons is

$$\Delta S = \overline{S}\left(\gamma_{ST}\overline{T} + \gamma_{SP}\overline{P}\right)\Delta\gamma_{TP} \qquad (1)$$

where $\gamma_{ST}$, $\gamma_{SP}$ and $\gamma_{TP}$ are the bimolecular rate constants for singlet-triplet, singlet-polaron and triplet-polaron annihilation, respectively. $\overline{S}$, $\overline{T}$ and $\overline{P}$ are the average values of the singlet, triplet and polaron densities, respectively. The $\Delta$ symbol indicates microwave dependent modulation of $\gamma_{TP}$ and hence the singlet density. To simplify the model we have assumed that the lifetime of triplets and polarons is controlled only by triplet-polaron interactions. We also have ignored the difference between paired polarons, which may recombine after collision with a triplet exciton, and unpaired polarons, which cannot; see Ref. [122] for full details. Nevertheless, this simplistic model shows clearly: (i) singlet excitons are quenched by triplet excitons *and* polarons, and (ii), the temperature dependencies of $\gamma_{ST}$, $\gamma_{SP}$ and $\gamma_{TP}$ must not be neglected. Each bimolecular rate constant is expected to increase with temperature.

Thus, Yang *et al.* [121], have incorrectly summarized the expected temperature dependence of singlet quenching by triplets and polarons. The temperature dependencies of the triplet population and the spin ½ resonance are not necessarily equal under this quenching model.

**(iv) Summary**

In two separate comments, Yang *et al.* [121,125] have faulted the technique and conclusion of the double modulation experiment. In the first comment [125] they claimed the double modulation data could be explained by 'polaron pairs having lifetime shorter than ~ 2 μsec'. In the comment discussed here, Yang, *et al.*[121] addressed the double modulation technique only in passing, claiming that it was inferior to single modulation transient measurements.

Neither claim can withstand scrutiny. The transient technique is redundant, and the frequency response measurement demonstrates that the fraction of polarons with lifetimes < 2 μs is extremely small [122,125]. The frequency response of polarons demonstrates that it is impossible for spin dependent polaron recombination to generate a *flat* frequency response under double modulation conditions. Furthermore, neither single modulation experiment probes the participation of purely optically-modulated species. This remains a unique advantage of the double modulation experiment.

Thus, we can only reiterate the original conclusion of the double modulation experiment: The flat frequency response under double modulation conditions confirms the participation of *singlet* excitons. These are the only species fast enough to respond at optical modulation frequencies exceeding 100 kHz. Hence PLDMR and PADMR monitor singlet exciton quenching processes and have no apparent relevance to exciton formation.

We further note that triplet-polaron quenching is but one possible spin dependent quenching phenomena. It was proposed in the absence of any other explanation given the apparent failure of the spin-dependent polaron recombination model. Triplet-polaron quenching is well established [1], and undoubtedly occurs within the films to some extent, but it may not be the only spin-dependent quenching process at work. For example, radiationless

charge recombination to the singlet ground state is spin dependent [120], and will lower polaron quenching of singlet excitons. This latter process is of minimal importance in electroluminescence, but may be significant in photovoltaic cells.

Thus, we conclude that the application of spin-1/2 magnetic resonances to the prediction of the singlet exciton fraction in electroluminescence is unfounded. Analysis of PLDMR and PADMR was claimed [28,80] to reveal the mechanisms of exciton formation and the fundamental efficiency limits of organic light emitting devices. But the double modulation experiment [124] confirmed that there is no link between spin-1/2 magnetic resonances and the singlet exciton fraction. This conclusion is model-independent. Thus, the singlet exciton fractions predicted from spin-1/2 magnetic resonance have no apparent validity. Rather, the double modulation experiment has confirmed that spin-1/2 magnetic resonances are second-order phenomena that monitor second and third-order quenching processes in organic semiconductors. This debate should not obscure the fact that analysis of magnetic resonances has not revealed the singlet exciton fraction, as was originally claimed [28,80].

**References**


[1] C. G. Yang, E. Ehrenfreund, M. Wohlgenannt, and Z. V. Vardeny, Phys. Rev. B (2007).

[2] M. K. Lee, M. Segal, Z. G. Soos, J. Shinar, and M. A. Baldo, Phys. Rev. Lett. **94**, 137403 (2005).

[3] M. Segal, M. A. Baldo, M. K. Lee, J. Shinar, and Z. G. Soos, Phys. Rev. B **71**, 245201 (2005).

[4] C. G. Yang, E. Eherenfreund, and Z. V. Vardeny, Phys. Rev. Lett. **96**, 089701 (2006).

[5] M. K. Lee, M. Segal, Z. G. Soos, J. Shinar, and M. A. Baldo, Phys. Rev. Lett. **96**, 089702 (2006).

[6] The single modulation data reported in Ref. 1 is inconsistent in the time and frequency domains. The associated theory matches both sets of data because it appears to have been applied inconsistently. Furthermore, if Eq. 2 in Ref. 1 is accurate, quenching and not spin dependent recombination explains the frequency response. This analysis is supported by linearizing Eq. 2, which yields a second order system with an overdamped homogeneous equation. The linearized solution for $n_1$ exhibits a zero below either pole frequency, yielding an overshoot in its transient response. The linearized solution for $n_2$ also exhibits a zero, but it is above the lowest pole frequency. Interestingly, the zeros cancel for $n_1+n_2$, apparently confirming that the sum may have been used to simulate the PLDMR in Fig. 2b. This is unphysical since singlet excitons cannot form from parallel polaron pairs. In contrast, the transient data is fit to some other combination of spin parallel and antiparallel polaron modulations; see the introduction of differing values for $\tau_{R1}$ and $\tau_{R2}$. Thus, the model of Ref. 1 can fit the transient but it cannot fit the frequency domain data. Equation 2 may also be used to describe the dynamics of triplet-polaron quenching. But

the triplet-polaron model depends only on the total population of quenchers. Hence the zeros in $n_1$ and $n_2$ are cancelled and the triplet-polaron model fits the frequency domain data.

[7] M. Pope and C. Swenberg, *Electronic Processes in Organic Crystals* (Oxford University Press, Oxford, 1982).

[8] B. van Dijk, P. Gast, and A. J. Hoff, Phys. Rev. Lett. **77**, 4478 (1996).

[9] M. Wohlgenannt, K. Tandon, S. Mazumdar, S. Ramasesha, and Z. V. Vardeny, Nature **409**, 494 (2001).

[10] M. Wohlgenannt, X. M. Jiang, Z. V. Vardeny, and R. A. J. Janssen, Phys. Rev. Lett. **88**, 197401 (2002).

# Chapter 5. Extrafluorescent Electroluminescence in Organic Light Emitting Devices

## 5.1 Introduction

Chapters 3 and 4 showed that the rate of singlet and triplet state formation for the last-mixed CT state, $k_{Sm}$ and $k_{Tm}$, are approximately equal for a variety of small molecule and polymeric organic semiconductors (Fig. 2.13). In this chapter, the value of $m$ is shown to be greater than unity for the prototypical semiconductor $Alq_3$, ie, the state consisting of an electron and hole on neighboring $Alq_3$ molecules is unmixed. Furthermore, the ability to manipulate the fraction of excitons which form as singlets in fluorescent materials by altering the structure of an OLED is demonstrated. A mixing layer that affects only charge transfer (CT) states, which are the precursors to excitons, is inserted. As a result, the singlet fraction and efficiency of the red fluorophore DCM2 is tripled. Fluorescence enhanced by CT spin mixing is termed 'extrafluorescence'. Its origin is in part an inversion of the usual energetic ordering of the singlet and triplet CT states.

## 5.2 CT State Ordering

Density functional theory is used to investigate the energetics of the CT(1) states in the archetypal small molecule tris(8-hydroxyquinoline) aluminum ($AlQ_3$) (Fig. 5.1(a)). First, the structure of a neutral, isolated $AlQ_3$ dimer taken from the δ-$AlQ_3$ crystal structure is optimized. Constrained DFT calculations on the $AlQ_3^{+,\uparrow}/AlQ_3^{-,\downarrow}$ and $AlQ_3^{+,\uparrow}/AlQ_3^{-,\uparrow}$ configurations are then performed, from which a CT(1) singlet-triplet gap

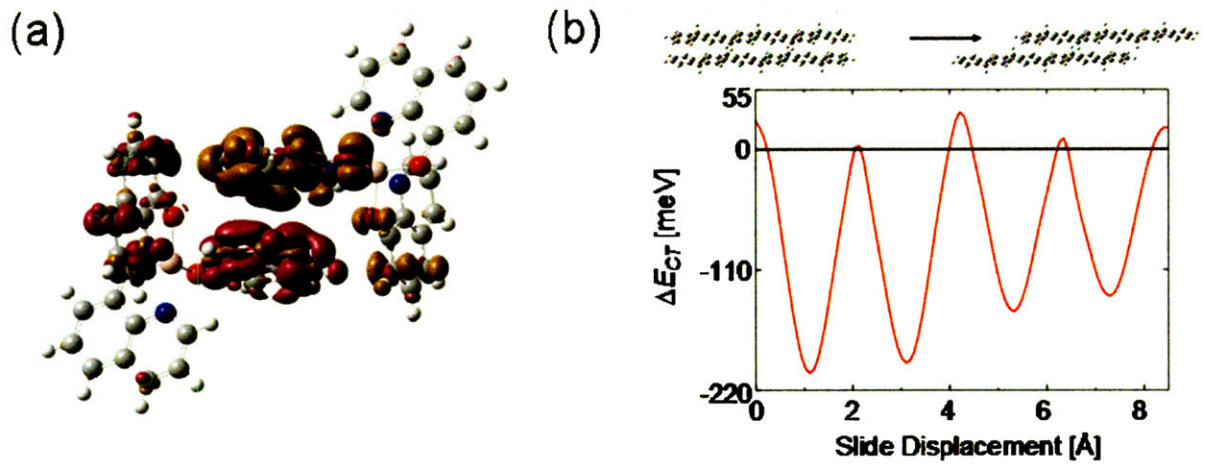


Fig. 5.1 - The spin state energies of CT(1) states are calculated with density functional theory (DFT). **(a)** The calculated charge density difference between the singlet and triplet CT(1) states, and the ground state, in a δ-$AlQ_3$ dimer. The right (left) hand molecule is constrained to be negatively (positively) charged, and gold (purple) surfaces enclose volumes where the CT(1) state has more (fewer) electrons. Analogous plots for the triplet CT(1) state are visually indistinguishable from the above plot. The proximity of negatively and positively charged regions stabilizes the singlet via kinetic exchange. The singlet CT(1) state is calculated to be lower in energy than the triplet CT(1) state by $\Delta E_{CT1}$ = -70 meV for the δ-$AlQ_3$ dimer shown, and by $\Delta E_{CT1}$ = -25 meV for an α-$AlQ_3$ dimer. **(b)** Singlet Triplet CT(1) splitting in polyphenylene dimer. As one monomer shifts relative to the other, the singlet-triplet gap oscillates due to the variation in the kinetic exchange contribution. For zero displacement the polarity of the Kadashchuk, *et al* result[45] is reproduced; at other displacements, however, S < T.

$\Delta E_{CT1}$ = −70 meV is obtained. This indicates that, for the CT(1) state, the singlet lies significantly *below* the triplet. A similar calculation on α–$AlQ_3$ places the singlet 25 meV

below the triplet. It has previously been shown that this technique accurately predicts the energies of both spin[126] and CT[127,128] states, supporting the accuracy of this prediction. For more distant $AlQ_3$ pairs $\Delta E_{CT1}$ should decay exponentially, rapidly becoming unimportant. All calculations are performed with NWChem[129,130] using B3LYP[131]. For δ-$AlQ_3$, the neutral geometry was optimized in the 3-21G basis and the constrained single point calculations used 6-31G*. For α-$AlQ_3$ and FIrpic/DCM2, the constrained state geometries were optimized in the 3-21G basis, while a 6-31G basis was used to compute the CT state singlet triplet gap in α-$AlQ_3$.

The larger than expected[45] CT(1) singlet-triplet gap indicates that the CT(1) mixing in $AlQ_3$ is probably slow (Eq. (2.25)). The spin statistics for $Alq_3$ are then set by the rates of the last-mixed CT state, ie, $k_{Sm}$ and $k_{Tm}$. As described in Chapter 3, measurements of small molecular weight fluorescent materials show that $\chi_S$ is limited to 0.25, despite the fact that $k_{S1}$ and $k_{T1}$ are not expected to be identical.

In addition, the calculated energetic ordering of the singlet and triplet CT(1) states is opposite to the exciton ordering, contrary to the usual assumption. The ordering of singlet and triplet CT(1) states was previously studied by Kadashchuk, *et al.*[45] Their work drew two conclusions. First, thermally stimulated luminescence (TSL) in MeLPPV indicated that triplet geminate pairs were typically 3-6 meV lower than their singlet counterparts. Meanwhile, INDO calculations on polyphenylene oligomers in a particular configuration gave S-T gaps similar to (if somewhat larger than) the experimental results. The obvious conclusion was that triplet CT(1) states are lower than their singlet counterparts, in contrast to the present findings. An attempt is made here to reconcile the two observations. On the theoretical side, a more extensive study of the S-T splitting in the phenylene oligomer dimer studied by

Kadaschuk, *et al* is performed.[45] The calculations are analogous to the $AlQ_3$ calculations above – constrained B3LYP in a 3-21G basis is used to isolate the two spin states for the CT(1) pair and evaluate the splitting. In this smaller basis set, the magnitude of the gap is expected to be overestimated by approximately a factor of two compared to the results for $Alq_3$, but trends should be accurately reproduced. Two monomers are held at a fixed separation of 3.75 Å in all cases, as a typical intermolecular distance achieved in small molecule thin films. If the oligomers are placed in a parallel cofacial arrangement (as was done in Kadashchuk, *et al.*) the same qualitative result is obtained: the singlet CT(1) state lies above the triplet. However, if one monomer is allowed to slide parallel to the other, a very rapid change in the S-T gap is seen. As is clear from Figure 5.1(b), even for this molecule the singlet state is usually lower and the deepest traps are clearly associated with singlets. In this light, the original geometry appears to be more an anomaly than the rule. The oscillations in $\Delta E_{CT1}$ can be explained using a kinetic exchange model. Taken together the results for phenylene oligomers support the original conclusion: while the singlet-triplet gap is material dependent it is certainly possible and even probable that the singlet CT(1) state lies lower in typical devices.

On the experimental side, there is no conflict in principle between Kadashchuk, *et al* and the modeling work presented here. The S-T gap in the CT(1) state is almost certainly *material dependent*, so it should not be surprising if a polymeric system like MeLPPV has a different CT(1) S-T ordering than a small molecule system like $AlQ_3$. Nevertheless, in a material with a dispersion of S-T gaps, the TSL technique will likely select those CT(1) pairs with stabilized triplets. For example, the TSL measurement begins with optical excitation of a film of MeLPPV at T = 4.2K for 30s. After the excitation is removed, there is a short dwell

time that allows the CT(1) states to come to equilibrium. Then, the temperature is slowly increased and the thermally-stimulated fluorescence and phosphorescence is recorded. The data unequivocally demonstrates that fluorescence requires 3-6 meV additional thermal activation. During the dwell time, however, we assume that the CT(1) states will occupy the lowest energy spin configuration, which the theory suggests is a singlet in some locations. But singlet CT(1) states can decay to the (singlet) ground state, whereas this decay process is nominally forbidden for triplet CT(1) states. Thus, it is possible that the dwell time effectively selects only those sites with stabilized triplet CT(1) states. Consistent with this model, the afterglow fluorescence decays within 5μs, but phosphorescence is observed after $10^3$ s, approximately three orders of magnitude longer than the triplet exciton lifetime.

The remainder of this Chapter explores the effect of turning CT(1) mixing on.

### 5.3 Spin-Mixing in Alq3:PtOEP

Fig. 5.1(a) shows that $Alq_3$ CT(1) states are non-degenerate, and the measurement of $\chi_S \approx 0.25$ in Chapter 3 shows that $k_{Sm} \approx k_{Tm}$ in $Alq_3$. Therefore $\chi_S$ is expected to vary only if the mixing interaction is artificially enhanced. Figure 5.2(a) shows the energy structure of an OLED used to investigate the effect of spin mixing on the singlet exciton fraction. The emissive layer in this OLED consists of $AlQ_3$ doped with either the Pt-containing molecule platinum octaethylporphine (PtOEP), or its Pt-free analog, octaethylporphine (OEP). PtOEP introduces strong spin-orbit coupling into the system, mixing both CT and exciton states. The OEP control allows for the isolation of the spin-orbit coupling effect. In addition, PtOEP captures triplet excitons formed in the $AlQ_3$ host, allowing for the monitoring of the triplet

population within $AlQ_3$ and the measurement of $\chi_S$. PtOEP will also capture some singlet excitons from $AlQ_3$.

All OLEDs are fabricated on cleaned and UV-ozone treated glass substrates precoated with an indium tin oxide (ITO) anode with a sheet resistance of ~ 20 Ω/sq. To enhance hole injection from the anode, all devices use a thin layer of poly(3,4-ethylenedioxythiophene):poly(4-styrenesulphonate) (PEDOT:PSS). This layer is prepared by spin coating onto the ITO substrate followed by baking at T ~ 115 °C for at least 30 minutes in an oxygen-free environment. Subsequent layers are deposited by thermal evaporation at pressures less than $3\times10^{-6}$ Torr. The cathode consists of 12 Å of LiF followed by 1000 Å of Al.

In both OEP and PtOEP devices, the molar concentration of the porphyrin is 0.9%, below the requirement for complete Förster transfer of singlet excitons, ensuring that some $AlQ_3$ fluorescence can be observed. The singlet and triplet exciton populations in the emissive layer are thus reflected in $AlQ_3$ fluorescence and PtOEP phosphorescence, whose efficiencies may be described generally by the respective equations[51]

$$\eta_{Alq_3}^{EL} = \eta_{Alq_3}^{PL}\left[(1-d_{EL})(1-r_S)\chi_S\right] \tag{5.1}$$

$$\eta_{PtOEP}^{EL} = \eta_{PtOEP}^{PL}\left[(1-d_{EL})\left[(1-\chi_S)r_T + r_S\chi_S\right] + d_{EL}\right]. \tag{5.2}$$

Here $\eta_{Alq_3}^{PL}$ and $\eta_{PtOEP}^{PL}$ are the PL efficiencies of $AlQ_3$ and PtOEP, $r_S$ and $r_T$ are the fraction of singlet and triplet excitons, respectively, that are transferred to the porphyrin

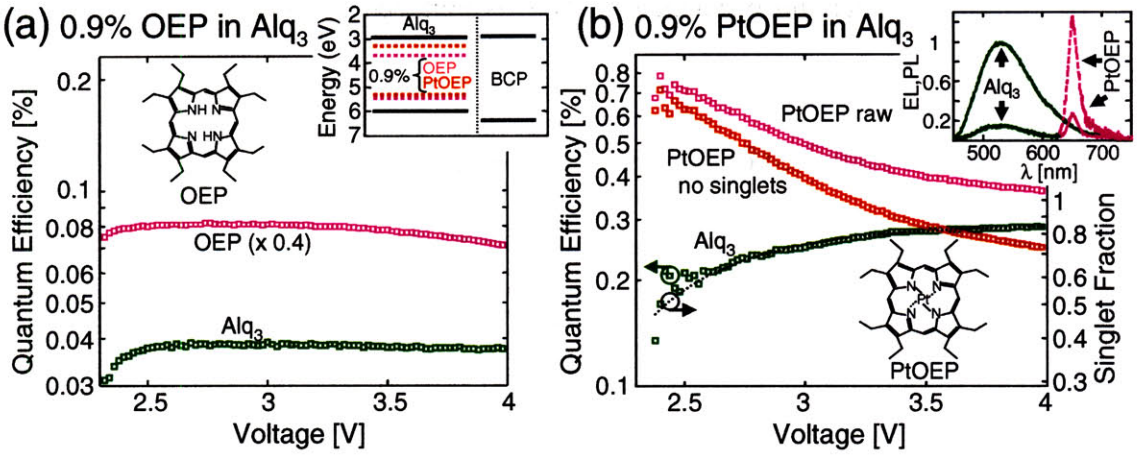


Fig. 5.2 - A comparison of the external quantum efficiency of an $AlQ_3$ OLED with mixing (doped with PtOEP) and without mixing (doped with OEP). **(a)** The external quantum efficiency of the $AlQ_3$ and OEP emission, with 0.9% OEP doping. **Inset** The OLED energy structure. An $AlQ_3$ emissive region is doped with either PtOEP to cause high mixing rates, or its Pt-free analog, OEP, to make a control device with low mixing rates. This device is used to measure $\chi_S$ when mixing is fast (this Figure), and $\Delta E_{CT}$ (Fig. 5.3). The thicknesses of the TPD, BCP and emissive layers are 500, 350 and 50 Å, respectively. See Methods for fabrication technique. **(b)** The external quantum efficiency of $AlQ_3$ and PtOEP emission, with 0.9% PtOEP doping. PtOEP efficiency is shown with ("raw") and without ("corrected") contribution from $AlQ_3$ singlet excitons and direct formation on PtOEP ($r_S$ and $d_{EL}$, respectively, in Eqs. (5.1) and (5.2)). The singlet exciton fraction $\chi_S$ is calculated from Eq. (5.3) with $A = 1$ and matches the $AlQ_3$ efficiency, confirming that the introduction of Pt causes $\chi_S$ to vary with voltage. We note that even if the raw PtOEP efficiency is used without correcting for $r_S$ and $d_{EL}$, $\chi_S$ still reaches 0.75 at 4V. **Inset** The photoluminescent (PL) spectra (solid lines) of a film of $AlQ_3$ doped with 0.9% PtOEP, and of a neat film of $AlQ_3$, whose maximum is normalized to unity. The ratio of PtOEP emission to $AlQ_3$ emission from the doped film is $f = (0.5 \pm 1)$ (see Eq. (5.3)). The introduction of PtOEP reduces the $AlQ_3$ PL efficiency by a factor of ~7, but reduces the $AlQ_3$ EL efficiency by a factor of ~2, from 0.7% to 0.3%. This is consistent with an increased singlet exciton fraction. The PtOEP EL emission at 6 V, shown with a dashed line, is significantly enhanced relative to the PtOEP PL emission, primarily due to the transfer of triplet excitons from $AlQ_3$ with probability $r_T \sim 1$.

from $AlQ_3$, and $d_{EL}$ is the fraction of all electrically-excited excitons that form on PtOEP rather than on $AlQ_3$. The flat efficiency of $AlQ_3$ for $2.5 < V < 4$ V in the presence of OEP in Fig. 5.2(a) demonstrates that $r_S$ and $d_{EL}$ in $AlQ_3$ doped with a porphyrin are independent of voltage.

In contrast, the quantum efficiency of $AlQ_3$ is voltage-dependent for $2.5 < V < 4$ V when Pt is introduced via PtOEP, suggesting that $\chi_S$ is changing. To confirm this, the $r_S$ and $d_{EL}$ contributions from the PtOEP emission are removed using a PL measurement of a thin film of 0.9% PtOEP:$AlQ_3$ with a $\lambda = 408$ nm pump. The ratio of PtOEP PL to $AlQ_3$ PL is defined as $f$. It is related to $d_{PL}$ and $r_S$ as $f = \left[(1-d_{PL})r_S + d_{PL}\right]\eta_{PtOEP}^{PL} \Big/ \left[(1-r_S)(1-d_{PL})\eta_{Alq_3}^{PL}\right] = (0.5 \pm 0.1)$, where $d_{PL}$ is the fraction of all optically-excited excitons that form on PtOEP rather than on $AlQ_3$. Then defining $\mathcal{P} = \log\left(\eta_{PtOEP}^{EL} - f\eta_{Alq_3}^{EL}\right)$ and $\mathcal{F} = \log\left(\eta_{Alq_3}^{EL}\right)$ gives

$$\chi_S = -A\frac{d\mathcal{P}}{d\mathcal{F}} \Big/ \left(1 - \frac{d\mathcal{P}}{d\mathcal{F}}\right), \tag{5.3}$$

where $A = \left[r_T + d_{EL}/(1-d_{EL})\right] \Big/ \left[r_T + d_{PL}/(1-d_{PL})\right]$.

From the respective absorption strengths of $AlQ_3$ and PtOEP at the pump wavelength, a calculation gives $d_{PL} \approx 6\%$. Thus, the triplet transfer efficiency, $r_T$, which is approximately unity,[50] dominates the denominator in the expression for $A$. It follows that $A >\approx 1$ regardless of $d_{EL}$, which is in any case expected to exceed $d_{PL}$. Figure 5.2(b) shows that the minimum $\chi_S$, calculated from Eq. (5.3) with $A = 1$ and an exponential fit to the data, accurately tracks $\eta_{Alq_3}^{EL}$. This confirms that the voltage dependence of the $AlQ_3$ fluorescent efficiency results from a changing $\chi_S$. At 4V, $\chi_S = (0.84 \pm 0.03)$, greatly exceeding the zero-mixing limit of $\chi_S = 0.25$ and the measured value of $\chi_S = (0.20 \pm 0.01)$ in $AlQ_3$.[22] The increase in $\chi_S$ is also reflected in comparisons of the EL and PL efficiencies (see Fig. 5.2(b) inset). The rising value of $\chi_S$ with voltage is consistent with the $AlQ_3$ triplet and singlet exciton energies $V_T = 2.05$ eV and

$V_S = 2.7$ eV,[132,73] so that injected carrier pairs must be thermally excited to form the singlet exciton for voltages $V_T < V < V_S$.

Next, the variation of $\eta_{PtOEP}^{EL}$ from the same OLED (Fig. 5.2(a)) with current density and temperature is examined. At low temperature, the calculated inversion of the usual singlet-triplet CT state energetic ordering suggests that the triplet population should vanish and $\chi_S \rightarrow 1$. From Eq. (5.2) we note that PtOEP captures both triplet and singlet excitons originally formed on $AlQ_3$. To extract the triplet signal from $\eta_{PtOEP}^{EL}$ we subtract $\eta_{PtOEP}^{EL}\big|_{T\rightarrow 0}$. Then we find the difference is proportional to the triplet density (1 - $\chi_S$),

$$\eta_{PtOEP}^{EL} - \eta_{PtOEP}^{EL}\big|_{T\rightarrow 0} = \eta_{PtOEP}^{PL}(1-d_{EL})(r_T - r_S)(1-\chi_S) \propto \exp\left(\frac{-|\Delta E_{CTm}|}{k_B T}\right), \qquad (5.4)$$

where $k_B$ is Boltzmann's constant, $T$ is temperature, and $\Delta E_{CTm}$ is the energy splitting of the last-mixed CT state in this system. The temperature dependence of $\eta_{PtOEP}^{EL}$ shown in Fig. 5.3 confirms the presence of a baseline at low temperatures and thermally-activated phosphorescence above the baseline. The inset of Fig. 5.3 shows that an Arrhenius plot of the triplet signal with $\eta_{PtOEP}^{EL}\big|_{T\rightarrow 0} \approx \eta_{PtOEP}^{EL}\big|_{T=12\,\mathrm{K}}$ fits a straight line well, yielding $\Delta E_{CTm}$ = - (7 ± 3) meV. Consistent with previous measurements,[133] $\eta_{PtOEP}^{PL}$ is approximately constant over this temperature range. Singlet exciton transfer ($r_S$) is not expected to be temperature dependent, and the efficiency of exothermic triplet transfer ($r_T$) from a fluorescent host to PtOEP has been measured to be constant with respect to temperature to within 5% over the relevant temperature range.[133] Finally, the temperature dependence of the OEP and $AlQ_3$ electroluminescent efficiencies from the OLED of Fig. 5.2(a) at these temperatures

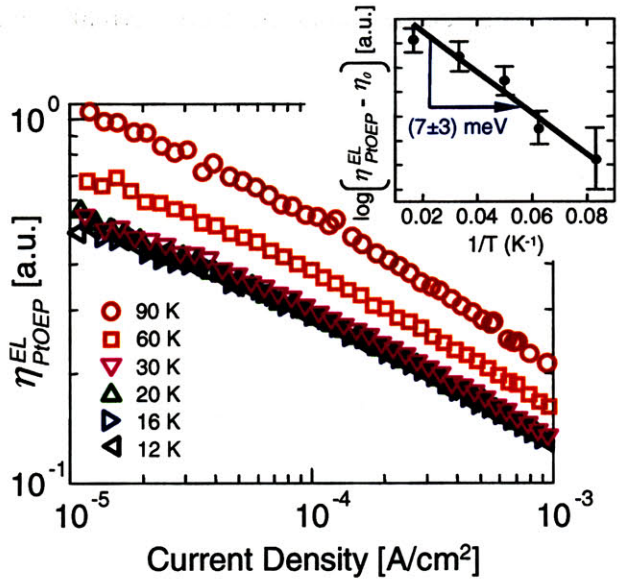


Fig. 5.3 - The PtOEP EL efficiency of the OLED of Fig. 5.2, doped with PtOEP, rises with temperature, indicating a lower-energy singlet CT($m$) state, where $m$ indicates the last-mixed CT state in the presence of 0.9% PtOEP doping. The rise with temperature is more pronounced at lower current densities, indicating that it is not the result of charge quenching. **Inset** An Arrhenius plot produces a straight line, confirming that phosphorescence is thermally activated, and yielding $\Delta E_{CTm} = -(7 \pm 3)$ meV. The error bars are calculated from the variation over current densities between $10^{-5}$ and $10^{-3}$ A/cm$^2$. Efficiency is zeroed as in Eq. (5.4), with $\eta_0 = \eta^{EL}_{PtOEP}\big|_{T\to 0} \approx \eta^{EL}_{PtOEP}\big|_{T=12\,\mathrm{K}}$.

is measured. The Arrhenius slope of $\eta^{EL}_{PtOEP}$ corrected for each of these efficiencies falls within error of the stated result, confirming that $\Delta E_{CTm}$ is not influenced by unforeseen temperature-dependent processes. Note that the presence of PtOEP in this measurement will increase mixing rates, it is unclear what the last-mixed state will be (ie, the value of $m$ is unclear in Fig 2.13).

This measurement of $\Delta E_{CTm}$ is consistent in sign but not in magnitude with the calculated values of $\Delta E_{CT1}$ = -70 meV and -25 meV for δ-$AlQ_3$ and α-$AlQ_3$ respectively (Fig. 5.1(a)). This may be the result of $m > 1$ in the $Alq_3$:PtOEP system of Fig. 5.2, because PtOEP does not cause a high enough $E_{MIX}$, at the low concentrations used here, to successfully mix CT(1). Alternatively, in the case that $m = 1$ in this experiment, the discrepancy with calculation could result from a larger average electron-hole separation in the experiments, which involve amorphous films, than in the calculations, which assume a closely packed crystal structure. A final possibility is that excitons form directly from CT(2) or higher, bypassing the CT(1) state entirely.

Regardless of which of these possibilities is true, the measured splitting energy is the more relevant value. It suggests $k_{Sm} >> k_{Tm}$ in $Alq_3$ doped with 0.9% PtOEP. To see this, consider that from Fig. (2.13), the singlet fraction can be expressed as

$$\chi_S = {k_{Sm}(1-P_T)} \Big/ {k_{Sm}(1-P_T) + k_{Tm}P_T}, \tag{5.5}$$

where $P_T = \exp\left(-\Delta E_{CTm} \Big/ k_B T\right)$ is the probability that the higher-energy triplet CT($m$) state is occupied, and the CT($m$) states are assumed to be completely thermalized. A splitting of $\Delta E_{CTm}$ = -7 meV is insufficient to account for the measured singlet fraction of $\chi_S = 0.84$, and so requires $k_{Sm} >> k_{Tm}$. Note that $m$ in $Alq_3$ doped with PtOEP will be lower than in neat $Alq_3$, since PtOEP introduces additional mixing. In any case, measurements of $\chi_S = 0.84$ and $\chi_S <$ 0.25 in the presence and absence, respectively, of spin-orbit coupling confirm that CT(1) state mixing is usually slow relative to $k_{S1}$ and $k_{T1}$. The measured splitting is sufficient to significantly reduce mixing rates.

Exchange effects are conservatively estimated to fall by an order of magnitude for an increase in charge separation of the size of one $Alq_3$ molecule, ~10 Å, (ie, going from $n$ to $n$ + 1 in Fig. 2.13). This assumes that the electron and hole wavefunctions fall to 1/e of their maximum value, a distance of 3 Å away from the molecule. Using even the larger, calculated CT(1) singlet-triplet splitting of 70 meV in $Alq_3$, this gives a splitting of $< 7$ μV for $n = 5$, on the order of the expected spin-orbit interaction strength.[26] Therefore $1 < m < 5$ for $Alq_3$.

## 5.4 The X-OLED

The demonstration of $\chi_S >> 0.25$ in the $AlQ_3$:PtOEP system suggests that engineering the CT mixing interaction can enable significant increases in the fluorescence efficiency of small-molecular weight OLEDs. But an increase in fluorescent efficiency was not achieved in the $AlQ_3$:PtOEP OLED of Fig. 5.2(a) since $AlQ_3$ singlet excitons transfer to PtOEP, or are mixed to the triplet state. Thus, to enhance fluorescence, an OLED should mix CT states *but not excitons*. In Fig. 5.4(a) an OLED with a selective CT mixing layer is described. As in other heterostructure OLEDs, excitons are formed on the lower energy side of the interface between the hole transport layer (HTL) and the electron transport layer (ETL). The emissive material is the red fluorophore DCM2. It is inserted on the HTL side of the interface in a narrow layer just 50 Å thick, to minimize the possibility of efficiency artifacts caused by shifts in the exciton formation zone.[53] DCM2 is doped into the host material 4,4'-N,N'-dicarbazolyl-biphenyl (CBP) at 1.6% molar concentration to prevent 'concentration quenching' of its emission. From the energy levels in Fig. 5.4(a), DCM2 is the lowest energy site, and is likely to host exciton formation at its interface with the ETL.

To obtain CT state mixing and extrafluorescence, we employ an ETL consisting of a thin film of iridium(III) bis [(4,6-difluorophenyl) pyridinato-$N,C^{2'}$] picolinate (FIrpic).[134] The presence of iridium in FIrpic enhances spin orbit coupling and mixes the spin state of the electron it carries. The spin of the CT state consisting of an electron on FIrpic and a hole on DCM2 is therefore also mixed. Further, calculations similar to those described above give a singlet-triplet CT(1) gap of 60 meV for a $FIrpic^-/DCM2^+$ heterodimer. Thus the interfacial CT states should be appreciably split. FIrpic will not quench DCM2, as FIrpic phosphoresces in the blue-green. It is employed here, however, purely as an ETL. Indeed, its electroluminescent quantum efficiency is only 0.2% in a neat film. In addition, FIrpic's spin mixing effect on neighboring molecules is reduced by the bulky side groups which surround its central heavy metal atom, reducing intersystem crossing effects in DCM2. In a control device, the FIrpic ETL is replaced by an ETL with low spin orbit coupling: 2,9-dimethyl-4,7-diphenyl-1,10-phenanthroline (BCP).[22] To constrain the emissive layer on the HTL side we employ an additional HTL: *N,N'*-bis(3-methylphenyl)-[1,1'-biphenyl]-4,4'-diamine (TPD).

Figure 5.4(b) compares the performance of the extrafluorescent OLED (or X-OLED) to the control device. The external quantum efficiency of the X-OLED reaches a maximum of 3.4%, or 2.8 times larger than the control. An OLED identical to the X-OLED, but with the FIrpic layer spaced from DCM2 by 100 Å of BCP, does not show enhanced efficiency. This is consistent with extrafluorescence resulting from spin mixing at the exciton formation interface.

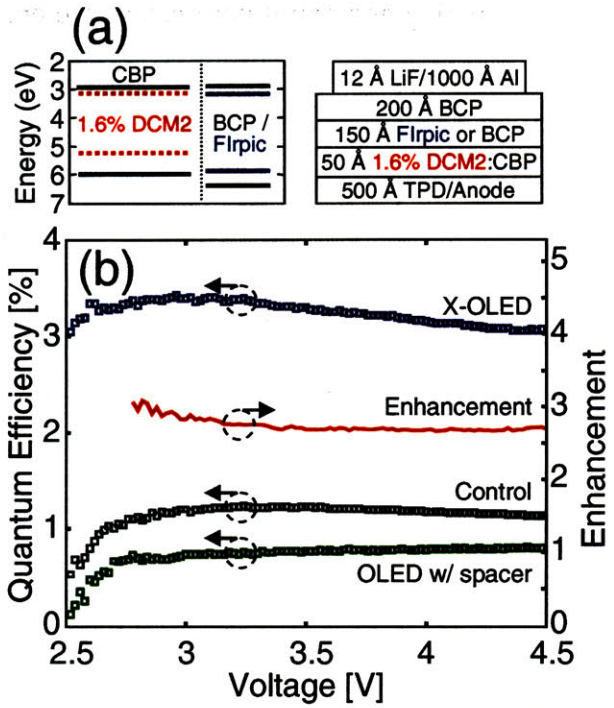


Fig. 5.4 - The structure and performance of the X-OLED and its control. **(a)** The X-OLED (with FIrpic) and its control (with BCP). Lowest unoccupied molecular orbital energy levels are derived from absorption measurements and exclude exciton binding energies. The doping concentrations given are molar and accurate to within ±20%. **(b)** The quantum efficiencies of the X-OLED and its control, in which FIrpic is replaced with BCP; and of an OLED identical to the X-OLED, but with the FIrpic layer spaced from the DCM2 layer by 100 Å of BCP, ie, the ETL is 100 Å BCP/150 Å FIrpic/ 100 Å BCP. The efficiency enhancement achieved by the X-OLED with respect to its control is shown on the right y-axis.

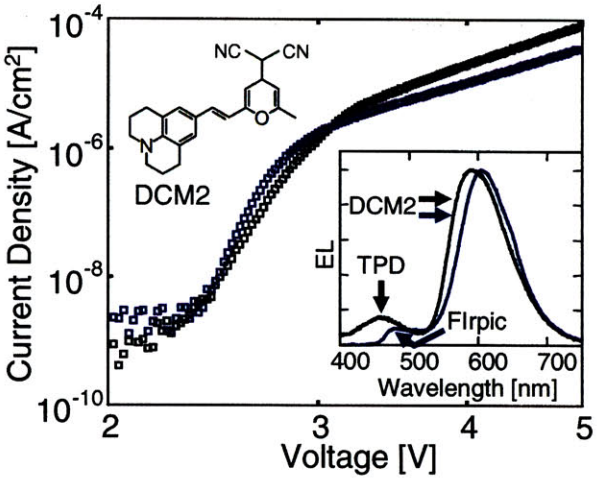


Fig. 5.5 - Current-voltage characteristics and EL spectra at 5 V (**Inset**) of the X-OLED (blue) and its control (black). The presence of polar FIrpic slightly red-shifts the EL spectrum of the X-OLED.[135]

Figure 5.5 compares the current-voltage (IV) characteristic and EL spectrum of the X-OLED device to its control. There are no significant differences in the IV characteristics of the two OLEDs, confirming that extrafluorescent phenomena are not due to variations in charge balance. The spectra of the two devices are also similar, although a small FIrpic shoulder is observed from the X-OLED and a small TPD shoulder is observed from the control, likely due to discontinuities in the thin emissive layers. The small red shift in the DCM2 emission in the X-OLED compared to the control is due to the higher dipole moment of FIrpic.[135]

Next, to verify that the X-OLED emission is fluorescence, and not sensitized fluorescence[41] or phosphorescence,[36] spectral- and time-resolved transient measurements were performed with a streak camera as shown in Fig. 5.6. The raw data contains a very

small shoulder in the spectral range $400 < \lambda < 450$ nm which we attribute to fluorescence from the CBP host. The CBP transient may be taken as the RC-limited response of the OLED. The transient of the control device is also RC-limited, with the same time constant $\tau$ < 55 ns. The full X-OLED response is observed to follow the same RC limit with the addition of a slow tail that comprises less than 10% of the total emission. By varying the reverse bias applied after the excitation pulse, the slow transient is demonstrated to be influenced by charge storage, *i.e.* a larger reverse bias speeds the removal of carriers from the OLED and quenches the slow transient. Thus, the X-OLED transient response shows that (i) the fast initial DCM2 transient is exactly as expected for fluorescence given the RC limitation of this OLED, and (ii) the slow tail is not evidence of sensitized fluorescence.

Fig. 5.6 shows that the lifetime of the DCM2 emission matches the RC limit of the device, and shows no evidence of sensitized fluorescence from slowly-decaying triplets in FIrpic. In principle, however, sensitized fluorescence can yield transient lifetimes that approach those of fluorescence. The limiting step is triplet to singlet energy transfer from the phosphorescent sensitizer to the fluorophore, and Förster energy transfer quenches the normally long-lived triplet. The quenching is a complicated function of the device structure and the Förster overlap between the phosphorescent donor and fluorescent acceptor. In the X-OLED, interpreting the efficiency enhancement as due to sensitization would require that DCM2 reduces the radiative lifetime[136] of FIrpic from 1.2 μs to less than the RC limit of 55 ns, a factor of 22 or more. However, when DCM2 is sensitized by $Ir(ppy)_3$, DCM2 is observed to reduce the radiative lifetime[136] of $Ir(ppy)_3$ from ~ 1.3 μs to 140 ns,[41] a factor of only 9.

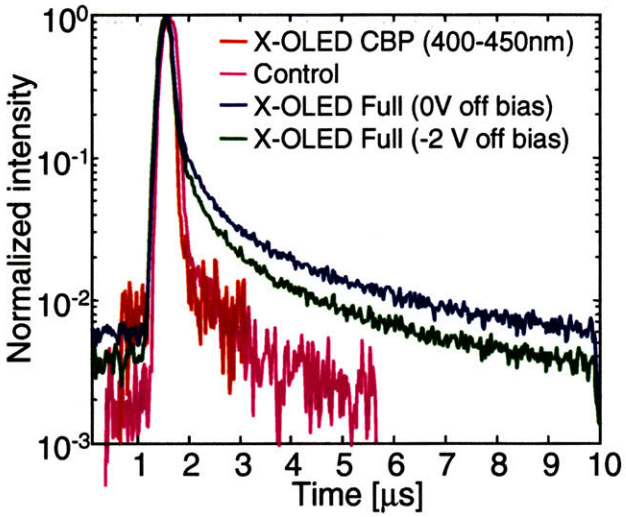


Fig. 5.6 - Transient responses of the X-OLED and its control to a 16 V drive. The X-OLED emission includes a small CBP component, which can be taken to be the X-OLED's RC-limited response, with lifetime $\tau < 55$ ns. The control device response is also RC-limited. The full spectrum X-OLED response is dominated by this RC-limited response. It also contains a long tail that is dependent on the strength of the reverse bias, indicating that the tail is due to charge storage. The CBP and control device transients have been cropped for clarity. These data confirm that fluorescence and not phosphorescence or sensitized fluorescence is the dominant emissive process in the X-OLED.

This difference in quenching occurs despite the fact that the phosphor is *blended* with DCM2 in the sensitized device, rather than separated into two half spaces by an interface. Thus, in contrast with the apparent quenching ratios, the overlap between phosphor and fluorophore is greater in the sensitized device. Furthermore, the discrepancy cannot be explained by a varying DCM2 concentration or differing Förster radii. As evidenced by the device EL spectra, which provide the most sensitive measure of DCM2 concentration,[135] DCM2 is doped at approximately the same concentration in CBP in both devices, and the Förster radii of

$Ir(ppy)_3$-DCM2 and FIrpic-DCM2 are also similar, 37Å and 40Å respectively. Thus, the short transient lifetime of DCM2 in the X-OLED cannot be explained by sensitized fluorescence.

As noted above, sensitization requires exciton formation in FIrpic. Given that holes are trapped in DCM2, there is a large hole injection barrier into FIrpic, but little or no electron barrier between FIrpic and DCM2. The elimination of the CBP host removes any possibility that holes are transported into FIrpic via the deeper CBP HOMO. Yet, the efficiency enhancement persists. FIrpic is also a poor exciton donor, with an EL quantum efficiency of just 0.2%. Finally, the observation of an enhanced singlet fraction in $AlQ_3$ in the presence of PtOEP, *cannot* be due to sensitized fluorescence. PtOEP is an acceptor and not a phosphorescent donor to $AlQ_3$. Thus, there is no sensitization pathway in that device, yet $\chi_S$ >> 25% is observed. It is interesting to note the similarity of the enhancement factor in $Alq_3$, and in the X-OLED, despite the different natures of the CT states involved in each.

It is verified experimentally that the host material is not significant by examining a second device, whose emissive layer consists of neat DCM. Fig. 5.7(a) shows the structure of a second X-OLED ("X-DCM1"), identical to the X-OLED above ("X- DCM2") except that the CBP:DCM2 layer is replaced by a layer of neat (*i.e.* undoped) DCM1. X-DCM1 shows a 2.3 times enhancement in external quantum efficiency relative to a control device, in which the FIrpic layer is replaced by BCP. Fig. 5.7(b) compares the current voltage characteristic and PL and EL spectra of X-DCM1 to its control. Both the PL and EL spectra of X-DCM1 are red-shifted with respect to the control.

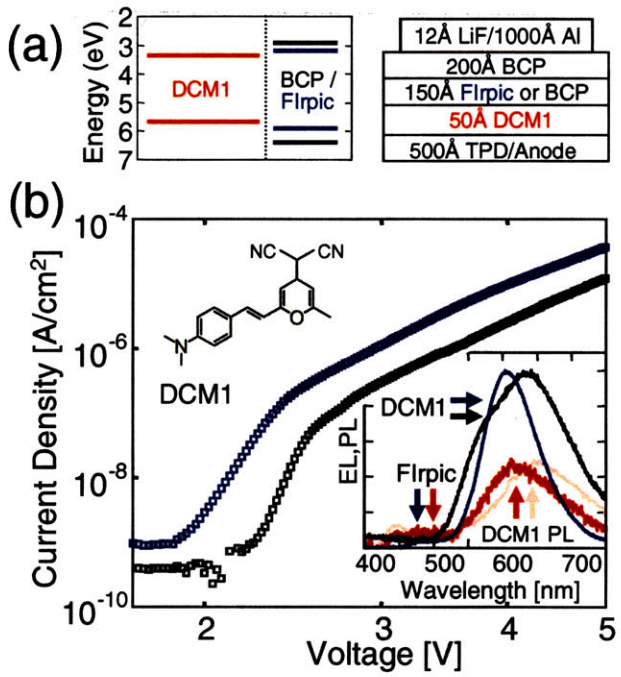


Figure 5.7 **(a)** A second X-OLED (with FIrpic) and its control (with BCP), identical to the X-OLED and control in Fig. 5.4(a), except that the CBP:DCM2 layer is replaced by a layer of neat DCM1. This second X-OLED is referred to here as "X-DCM1", and the X-OLED in Fig. 5.4(a) as "X-DCM2". Lowest unoccupied molecular orbital energy levels here and in the text are derived from absorption measurements and exclude exciton binding energies.[36,45,126-128,137] X-DCM1 is fabricated in the same manner as X-DCM2. **(b)** Current-voltage characteristics and EL spectra at 5 V (**Inset**) of X-DCM1 (blue) and its control (black). The inset also shows the PL spectra of X-DCM1 (red) and its control (pink). The presence of FIrpic blue-shifts both the PL and EL spectra.

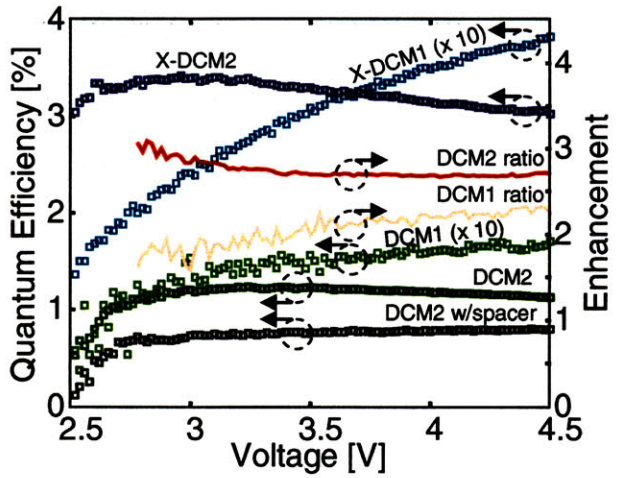


Figure 5.8 - The quantum efficiencies of X-DCM1 and its control, added to Fig. 5.4(b). The X-DCM1 and X-DCM2 controls are labeled "DCM1" and "DCM2" respectively. The efficiency enhancements achieved by the two X-OLEDs, shown on the right y-axis, are similar.

The PL efficiencies of DCM1 next to BCP or FIrpic, however, are similar, so this shift cannot account for the enhancement in EL efficiency. Fig. 5.8 adds the external quantum efficiency of X-DCM1 and its control to Fig. 5.4(b). X-DCM1 achieves an external quantum efficiency of 0.38% at $V = 4.5$ V, or 2.3 times larger than its control, suggesting $\chi_S > 0.58$ in DCM1. Note that the absolute efficiencies of the DCM1 devices are lower than the DCM2 devices due to 'concentration quenching' in the neat film of DCM1.

The energy level diagram in Fig. 5.7(a) shows that excitons will form on DCM1 as it is the lowest energy material contained between the ETL and the HTL. In addition, a hole injection barrier between FIrpic and DCM1 prevents exciton formation in FIrpic. Therefore, the efficiency enhancement of X-DCM1 cannot be due to sensitized fluorescence. In addition, the efficiency enhancement of extrafluorescence is preserved in this device

despite the absence of the host material CBP used in the X-DCM2 devices, demonstrating that CBP does not participate in extrafluorescence. Rather, the exciton precursor in both extrafluorescent OLEDs is $FIrpic^-/DCM^+$ which collapses to an exciton on DCM.

## 5.5 Conclusion

The enhancement of the electroluminescent efficiency of the two red dyes DCM1 and DCM2 is shown to be the result of an enhanced singlet fraction through the following checks: (1) the singlet fraction in $Alq_3$ under high mixing rates is shown to increase by ~3x, consistent with the EL efficiency increase from DCM1 and DCM2; (2) the enhancement is independent of voltage, so it is not a quenching effect; (3) the similarity of the current-voltage characteristics of the X-OLED and its control indicate the enhancement is not a charge balance effect; (4) the spectra of the X-OLED and its control, and the tightly confined recombination zone used, indicate the enhancement is not a cavity effect; (5) the absence of a host for the X-OLED employing DCM1 indicates the host does not play a role; (6) the enhancement disappears when the mixing layer is moved away from the recombination zone, consistent with a CT mixing explanation; (7) transient analysis shows that the enhancement is not the result of energy transfer from excited states created on the mixing layer.

Extrafluorescence does not require an emissive phosphor, and can be applied to existing stable fluorescent materials. It provides an alternative to the established techniques for achieving 100% internal quantum efficiency, phosphorescence[36] and sensitized fluorescence.[41] Among its advantages are a wide library of stable fluorophores, many of which combine deep color saturation, narrow linewidths, and stability; and a low-lifetime emissive state (singlet excitons) which avoids efficiency quenching at high concentrations.

This work also helps resolve the controversy concerning the conjugation length dependence of $\chi_S$.[22] It is demonstrated that in small molecules such as $AlQ_3$ and DCM2, the CT(1) mixing rate is slower than singlet or triplet exciton formation. This is demonstrated directly by the fact that turning the CT(1) mixing rate high dramatically increases EL efficiency. The reason for the slow mixing rate is shown to be a significant energy splitting between singlet and triplet CT(1) states. This splitting is demonstrated both through density functional calculation and direct measurement, for $Alq_3$. Thus, previous reports[22,50] of degenerate spin fractions in small molecules can be explained mixing interactions which are weak relative to the strength of the singlet-triplet splitting. Comparisons between theory[47] and experiment must consider material-dependent CT(1) mixing rates, as well as distinguish between bulk and interfacial measurements of $\chi_S$.[22] The measured value of the CT state splitting presented here suggests that $k_{S1} >> k_{T1}$, in order to account for the high measured singlet fraction of $\chi_S = 0.84$.

CT(1) state splitting also helps explain why exciton formation is impervious to spin-½ magnetic resonance conditions (Refs [81,82,93] and Chapter 4): namely $m > 1$. The larger is $m$, the more alike $CT^1(m\text{-}1)$ and $CT^3(m\text{-}1)$ states will become, so the more alike $k_{Sm}$ and $k_{Tm}$ will become, and the more equal the populations of $m_j$ = -1,0 and +1 $CT^3(m)$ states will become. Resonance, which serves only to equalize these populations, has no effect.

# Chapter 6. Conclusion

The theme of this thesis has been to probe the mixing rates between singlet and triplet excitons and CT states in organic semiconductors, shown in Fig. 2.13. Chapter 3 introduces a robust technique for the measurement of the photoluminescent (PL) efficiency of an organic emitter. The technique's advantages are that (1) it does not require knowledge of the fraction of pump light absorbed; (2) it does not require knowledge of the fraction of photoluminescence outcoupled to the detector (and makes knowledge of this factor for the electroluminescence efficiency measurement unnecessary); and (3) it is sensitive to material degradation. A double-modulated synchronous measurement setup makes this approach more robust, by excluding potential noise sources such as leakage current and pump intensity fluctuations. Using this technique, it is found that ≈25% of excitons formed as singlets, and ≈75% as triplets, in the materials $Alq_3$ and MEH-PPV. Previous measurement had found the singlet fraction in CBP to also be ≈25%.[41,74] Thus, in these materials, the singlet and triplet formation rates are equal, for the last-mixed CT state. In the language of Fig. 2.13, $k_{Sm} = k_{Tm}$, where the last-mixed CT state is CT($m$), in which the electron and hole are $m$th nearest neighbors. It is expected, however, that $k_{S1} / k_{T1}$ in these materials does not equal unity, due to the differing nature of the final singlet and triplet exciton states. Therefore this data suggests, but does not prove, that spin mixing turns off before the nearest-neighbor CT(1) states are formed, or in other words, $m > 1$ (Fig. 2.13).

Previous studies had found singlet fractions greatly exceeding 25% in PPVs (OC1C10-PPV[52], and orange and green PPV[53]). High measured values of polymer singlet

fractions may have resulted from a measurement inaccuracy as discussed in Section 3.7; or from an unintentional turning on of mixing rates in the materials studied, for example by trace amounts of heavy metal catalysts remaining from synthesis. Furthermore, in the presence of a mixing agent, the energy delivered to the recombination interface of an OLED can affect the singlet fraction (Fig. 5.2(b)). The OLED used in this thesis to determine the singlet fraction for MEH-PPV uses a BCP hole-blocking layer, potentially altering the energy delivered to this interface, and affecting the result.

Chapter 4 examines photoluminescence-detected resonance (PLDMR) data that was taken in the literature as evidence for $k_{S1} >> k_{T1}$ for the polymer MEH-PPV. It is demonstrated in Ref. [93] and in Chapter 4 that optically detected magnetic resonance effects result from a singlet exciton quenching process, rather than from exciton formation dynamics. The previous literature conclusion that, in MEH-PPV, $k_{S1} >> k_{T1}$, and that the singlet fraction is $>> 25\%$, is therefore invalid. In Chapter 4, a complete quantitative model for the frequency dependence of singly-modulated photoabsorption-detected magnetic resonance, and singly- and doubly-modulated PLDMR, is constructed and shown to work well. The model is based on the spin-dependent interactions of *two* separate singlet exciton quenchers: triplet excitons, and polarons. Under resonance, these two species quench each other at a higher rate, reducing the densities of each, and increasing photoluminescence. With just four free parameters, this model successfully reproduces the shapes of these three independent frequency responses over decades of frequency, as well as the magnitudes of the two photoluminescence-detected frequency responses. The model also finds that two types of polarons exist (paired and unpaired), and is used to extract from the data parameter values such as quencher lifetimes and populations.

By showing that PLDMR effects are not related to exciton formation (or equivalently, resonance does not effect exciton formation), Chapter 4 effectively shows that the populations of the three different $CT^3(m)$ states ($m_j$ = -1, 0 and 1 in Fig. 4.1) are already equal outside of resonance. The equalization of these populations by applying a resonant microwave field then has no effect. This in turn suggests $k_{Sm} \approx k_{Tm}$. This conclusion is consistent with the small size of electroluminescence-detected resonances (ELDMR) and with the conclusion of Chapter 3.

It is expected that $k_{S1}$ and $k_{T1}$ are not equal, because the nature of the final singlet and triplet exciton states differ significantly. As $m$ increases, $k_{Sm}$ and $k_{Tm}$ are expected to become more similar. Chapters 3 and 4 suggest, therefore, that $m > 1$, so that even if $k_{S1} > k_{T1}$, as has been argued in the literature, a lack of CT(1) mixing prevents this inequality from affecting electroluminescence (EL) efficiency. Chapter 5 explores the effect of turning on the CT(1) mixing rate, $k_{M1}$. The result is a 2.7x increase in fluorescent EL efficiency from two red fluorescent dyes, DCM1 and DCM2. This, together with the direct measurement of high singlet fractions in $Alq_3$ when CT state mixing is turned on, serves as direct evidence that CT(1) mixing is usually off and $m$ >1. Chapter 5 proves that the increased fluorescent EL results from a higher singlet fraction. It further shows through calculation and measurement that the energetic splitting between $CT^1(1)$ and $CT^3(1)$ states in the archetypal small-molecule $Alq_3$ greatly exceeds the expected mixing interaction energy, thus providing an explanation for low CT(1) mixing rate. Both calculation and experiment also show that the energetic ordering of CT states is opposite to that of excitons, namely, the singlet state has lower energy than the triplet state.

The calculated CT(1) splitting is sufficient to account for the entire enhancement of the singlet fraction, and does not require a fast singlet formation rate ($k_{S1} >> k_{T1}$). The measured

CT splitting, however, is an order of magnitude smaller and does require a faster singlet formation rate to explain the high measured singlet fraction. This discrepancy may be due to assumptions used in the calculation, or because the measurement probes the energetics of CT($m$) with $m > 1$. In both cases, the measured splitting is the more relevant number. Thus, this thesis contests measurements of high singlet fractions in PPV polymers (Chapter 3), and disproves the connection between spin statistics and magnetic resonance (Chapter 4) which was used to argue for high singlet fractions in MEH-PPV, but suggests that $k_{S1} >> k_{T1}$ in small molecules, as has been claimed for polymers.[47,48.,49]

As a final comment, the X-OLED can be seen as an example of the utility of a "division of labor". The challenge with achieving stable, saturated phosphorescent blue results from the fact that the phosphor must both be an efficient emitter, and efficient at mixing spin states. Optimizing the performance of a device is more difficult when multiple performance metrics are affected by one variable. A remedy is to distribute different device functions among different parameters. This kind of an approach is common in the history of many technologies, including organic semiconductors. For example, OLEDs commonly emit light from organic dyes doped into charge transport materials, rather than from the transport materials themselves (as was done with early OLEDs). This allows the dye and the transport materials to be individually tailored to their respective functions. Similarly, organic photovoltaic devices must trade off absorption against charge separation efficiency, both of which are affected by device thickness. Unpublished work by Heidel, Mapel *et al* separates absorption and charge separation functions by attaching an external "antenna" to the device. The antenna is responsible for all of the device absorption. The X-OLED follows in this vein

by separating the spin-orbit coupling function necessary to alter the spin fraction, from the luminescent function of the emissive dye itself.

# Appendix. Protein Electronics

An account of my time at MIT would not be complete without describing my efforts to push and pull current through innocent proteins. Figure 1.1 showed the progression of complexity of organic semiconductors, culminating with the protein. Optimized by evolution, protein electronic machinery is characterized by a remarkably fine positioning of components, and very high efficiencies. The protein I focused on was the photosynthetic reaction center complex, extracted from the purple bacterium *Rhodobacter (Rb.) sphaeroides*. This protein, working at the core of the photosynthetic process, is 95% efficient at converting absorbed light into charge. In addition, it features some of the smallest known electronic circuitry (Figs. A1 and A2). An attempt was made to exploit each of these characteristics, in two distinct projects: the first, to fabricate a photovoltaic cell in which a monolayer of photosynthetic proteins acts to absorb light, and separate excited states into charge. This project was led by my colleagues Rupa Das, and Patrick Kiley. I performed the spectrally-resolved photocurrent measurement presented in this Appendix. The second project, which I led, was to fabricate a nanoscale transistor with a channel consisting of a single RC protein. The gate would serve to switch the conduction pathway between the two branches shown on the right hand side of Fig. A1.

In both projects, chemical self-assembly was used to orient and bind the RC protein to a gold surface. Fig. A3 shows the self-assembly scheme. As described in Ref. [138], 1 nm of Cr and 4 nm of Au are deposited onto ITO-coated glass. This is then incubated with 6.1 mg/mL of DTSSP for 10 minutes, washed with deionized $H_2O$,

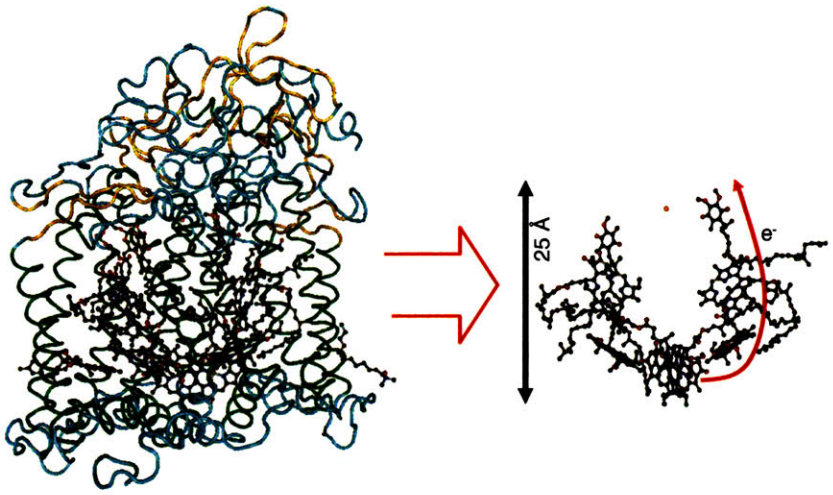


Fig. A1 – The photosynthetic reaction center complex from the purple bacterium *Rhodobacter (Rb.) sphaeroides*. On the left, the complete protein is shown, comprising a scaffold of three subunits which coordinate six pigment molecules, shown on the right. These pigment molecules are held to Angstrom precision. Excitons are channeled towards the bacteriochlorophyl pigment dimer known as the "special pair", where they are broken into charge that is then channeled away along another pigment, as shown. The conversion efficiency of absorbed light to extracted charge is 95%.

incubated with 0.33 mg/mL of NTA ligand for 10 minutes, charged with 200 mM nickel sulfate, and incubated with 100 μL of RC solution for 1 hour at 4° C in the dark.

The photovoltaic device structure is shown in Fig. A4. After self-assembly, two layers of organic semiconductors are thermally evaporated onto them. These layers serve to protect the proteins from the thermally-evaporated metal cathode. Since the proteins are oriented with the end of the electron pathway facing away from the substrate, these protective layers must

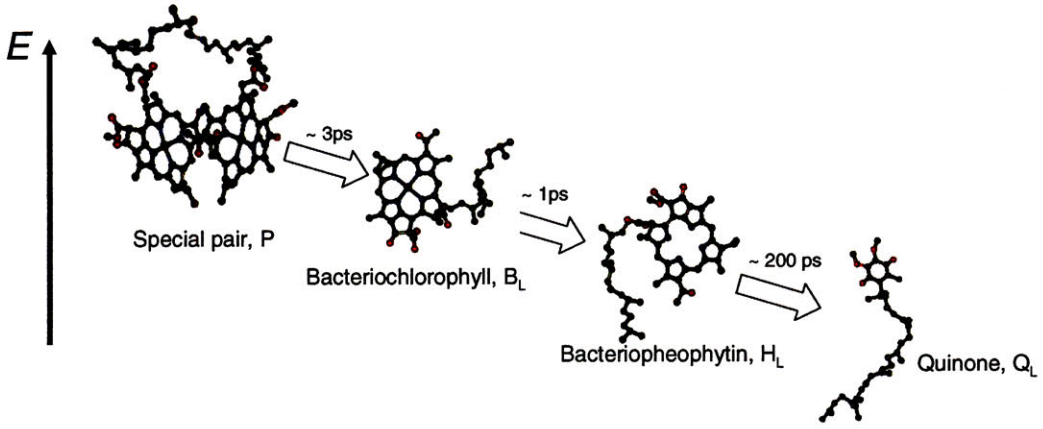


Fig. A2 – Descending energy staircase of pigments shown in Fig. A1. Excitons are broken into charge at the special pair and transfer rapidly to other pigments.

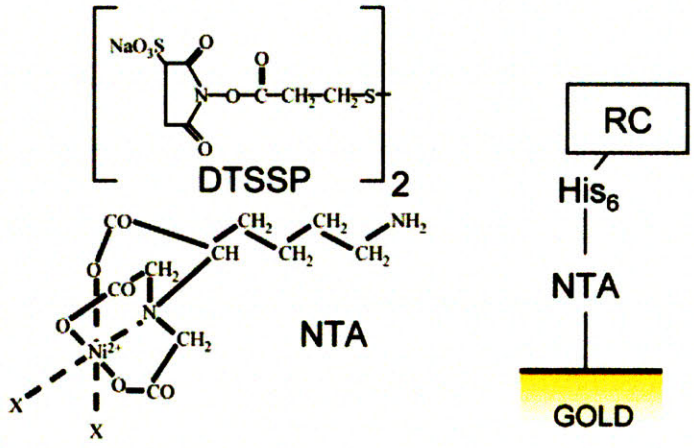


Fig. A3 – Self assembly scheme for RC protein. Gold surfaces are functionalized with DTSSP and then $Ni^{2+}$ - NTA. RC proteins are are immobilized using a $His_6$ tag. From Ref. [138].

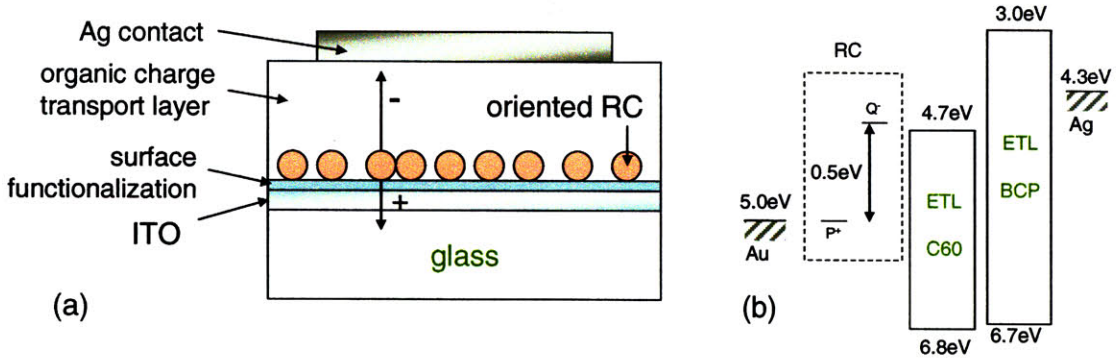


Fig. A4 – A photovoltaic cell whose active layer consists of RC proteins. (a) The device structure. RC proteins are attached and oriented to a Cr/Au surface. Two organic layers are thermally evaporated on top, followed by an Ag contact. (b) The energy structure of the device. The two organic semiconductor layers protect the proteins, and convey electrons to the Ag cathode. BCP also serves to block hole injection.

be electron-transporting. The BCP layer also serves to prevent hole injection into the device, improving the IV characteristics. Fig. A5 shows the device performance. Pumped at $\lambda = 800$ nm, where the thermally-evaporated organic layers absorb only minimally, the device has an open circuit voltage of 0.085 V, a closed-circuit current of 0.44 $\mu A/cm^2$, and a power conversion efficiency of 0.01%. The device, therefore, will not break any records. Since there are likely to be voltage drops across the thermally-evaporated layers, they limit the device's open circuit voltage. In addition, the monolayer of proteins is likely incomplete, and many of the assembled proteins may be non-functional.

The importance of the device, though, is its characteristic in Fig. A5(b). This data shows that the device's photocurrent dependence on pump wavelength approximately

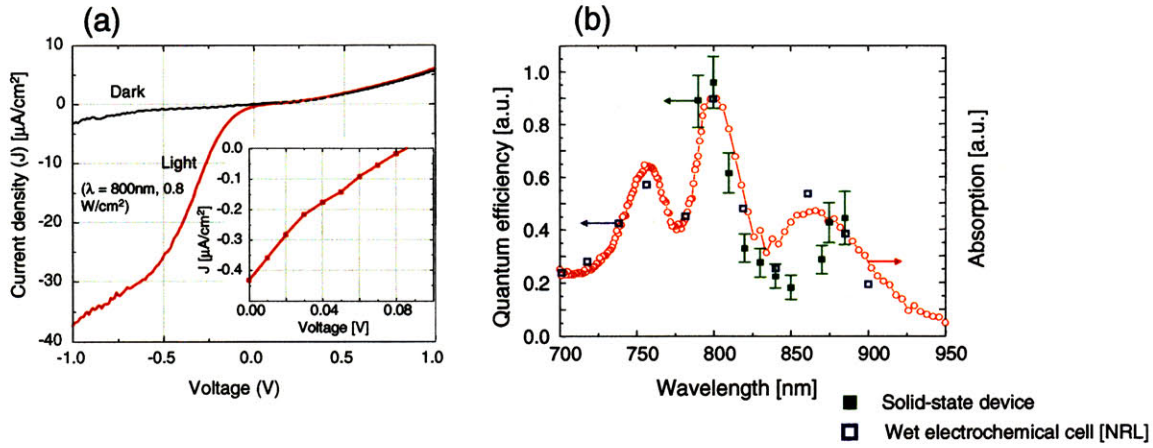


Fig. A5 – The performance of the device of Fig. A4. (a) Dark and light IV spectra. **Inset**: Open-circuit voltage and closed-circuit current under illumination. (b) The dependence of photocurrent on pump wavelength (green) matches the same characteristic of an electrochemical wet cell (blue), and the absorption characteristic of the proteins in solution (red).

matches both the absorption spectrum of the proteins in solution, and the photocurrent spectrum of a wet electrochemical cell using the same protein. This indicates that the proteins are active and functional, and that the device is a successful hybrid between biological and electrical functionality.

Fig. A6 shows the schematic of a transistor device whose channel consists of a single reaction center protein. The source and drain are made from gold, onto which the protein will self assemble. This structure was expected to produce two kinds of interesting data: first, two-terminal rectifying current-voltage characteristics. The rectification behavior is expected to result from the energy staircase of Fig. A2. The $His_6$ tag on the protein is near the special pair, so that it is expected to orient itself with its electron pathway roughly parallel to the oxide.

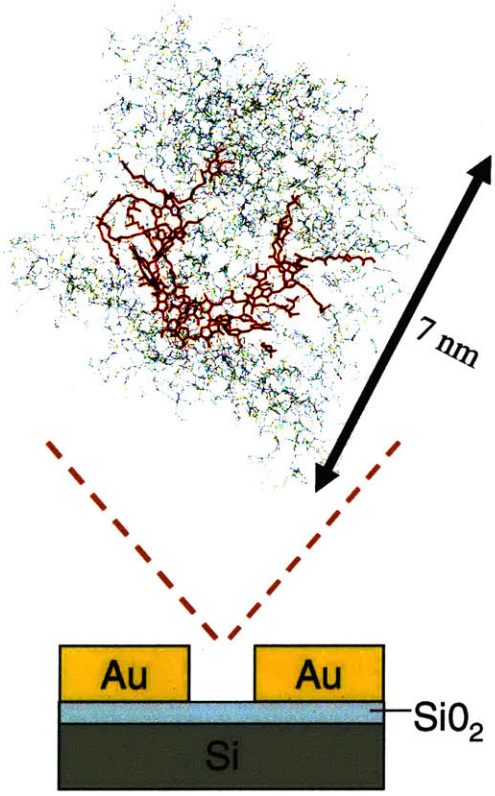


Fig. A6 – A schematic of a transistor with a channel consisting of a single RC protein, with its scaffold shown in grey and the electron pathway shown in red. The protein self-assembles onto the gold, with the axis of its electron pathway parallel to the $SiO_2$. Which gold contact it attaches to is uncontrolled, as is its rotational orientation. In certain orientations, the Si gate may be able to control which of the two RC electron pathways current flows through.

The polarity of the rectification can not be predicted, however, since both source and drain are gold. The second kind of interesting data expected from this structure is a gate effect on conductivity. The RC protein channels electrons preferentially through one of its two pathways (Fig. A1). In certain orientations, the gate was expected to make conduction through

the other pathway energetically favorable. Given that the two pathways would likely have very different tunnel barriers to the drain, a significant conductivity difference was expected.

The challenge was to fabricate a transistor with a ~7 nm channel length, and place a single reaction center into it. The problem was approached with a combination of photolithography, electron-beam lithography, electroplating, and electromigration. Figure A7 shows the large-scale contacts, with a separation distance of about 50 μm, and the small-scale contacts defined inside them, with a separation distance of about 100 nm. It was found difficult to define through e-beam lithography contacts separated by less than 50 nm. To take the distance from 100 nm to 7 nm, two approaches were used. The first was to place the entire wafer of contacts into an Au electroplating bath, and plate the contacts together until the distance between them had been reduced to the desired quantity. An array of contacts was defined, with gradually increasing separation distances. A single reference contact was also defined, with a short separation distance. The impedance of the reference contact was monitored during electroplating. When it shorted, plating was stopped. This acted as a kind "fuse" on the electroplating time. The second approach attempted was electromigration.[139] Here, fused contacts were defined with electron-beam lithography, and then broken by applying high voltages at low temperatures. Micrographs of the resulting contacts are shown in Fig. A8. Each approach had its difficulties. Electroplating produced asymmetrical contacts, since only one side of the contact pair was plated. Both approaches produced rough contacts. The most significant challenge, however, was detecting the presence of the protein after self-assembly. This was not accomplished. Note that the electroplated devices had the protein self-assembly step after fabrication, while for the electromigration devices, self-assembly was performed after the e-beam steps but before electromigration.

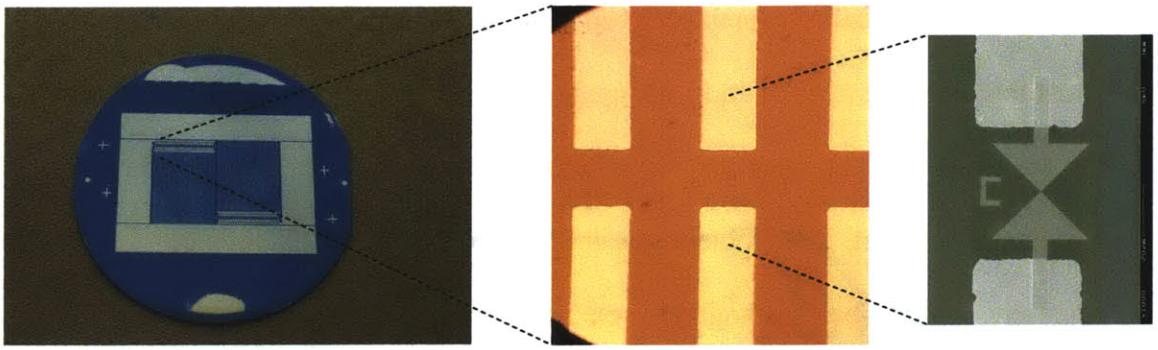

Fig. A7 – Fabrication of the device of Fig. A6. Left: An array of Au contacts is photolithographically defined on a Si wafer. Each contact is connected to a thick contact pad, which is used during electroplating. After electroplating, the wafer is cleaved and the contacts become electrically independent. Middle: An optical micrograph of a photolithographically defined contact. The vertical separation is 50 μm. Left: After the micron-scale contacts are defined, electron-beam lithography is used to create either a pair of gold contacts separated by ~100 nm, which are then electroplated to smaller separation; or, a fused pair of contacts which are broken by electromigration (Fig. A8).

Fig. A9 shows two-terminal current-voltage characteristics of the electroplated and electromigration devices after protein self-assembly. Rectification was achieved in the electroplated devices, and the current levels corresponded well with literature values, measured with STM. However, this rectification effect could be due to the asymmetry in the contact morphologies resulting from electroplating. The electromigrated device showed only mild rectification behavior compared with the literature measurement.[140] While the fabrication approach succeeded, then, in making a test structure into which proteins could be self-assembled, the conclusion of the project was that a robust method

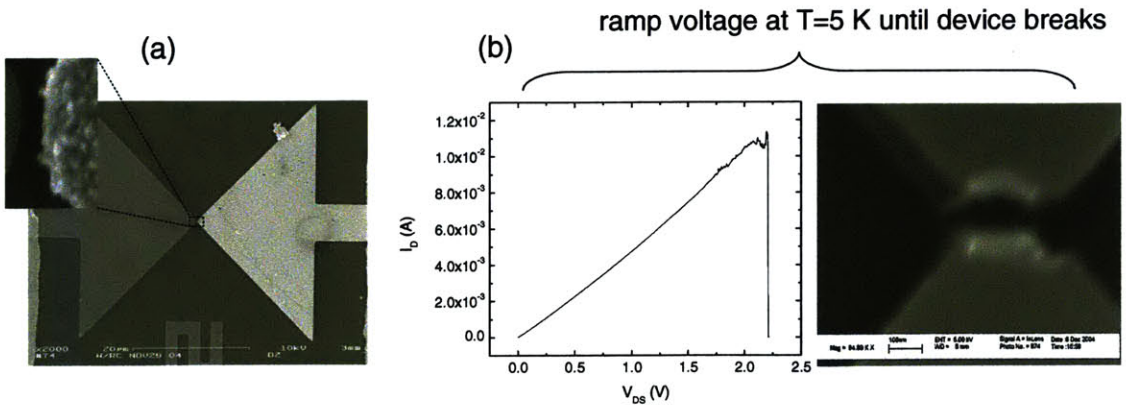


Fig. A8 – Two techniques used to approach the 10 nm scale required for the transistor device of Fig. A6. (a) Starting with a pair of contacts separated by ~100 nm, one contact is electroplated (in this case, the right contact) until the desired distance is reached. The resistance of a reference pair of contacts is monitored during electroplating, and electroplating is stopped when this resistance drops to zero, assisting in achieving the desired separation distance. The scale bar shown has a size of 200 nm. (b) Starting with a pair of fused contacts, a voltage is applied to the contacts at low temperature, and ramped up until a break is measured. The scale bar shown has a size of 100 nm.

of detecting the presence of the proteins would have to be developed before the three-terminal measurement platform could prove useful.

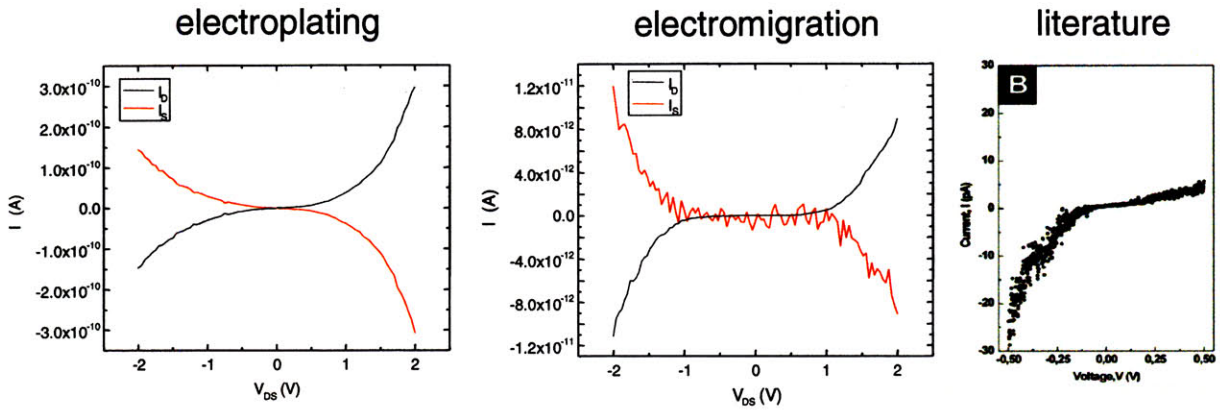


Fig. A9 – Current-voltage characteristics for the devices of Fig. A8, after protein self-assembly, compared to a literature value measured through a single reaction center with STM (right).[140] Black curves are current flowing into the drain; red curves are current flowing into the source.

## References


[1] Martin Pope and Charles Swenberg, *Electronic Processes in Organic Crystals*, 1st ed. (Oxford University Press, Oxford, 1982).

[2] Sergey Lamansky, Peter Djurovich, Drew Murphy et al., "Highly Phosphorescent Bis-Cyclometalated Iridium Complexes: Synthesis, Photophysical Characterization, and Use in Organic Light Emitting Diodes," J. Am. Chem. Soc. **123** (18), 4304-4312 (2001).

[3] M Segal, M. Singh, K. Rivoire et al., "Extrafluorescent Electroluminescence in Organic Light Emitting Devices," Nature Materials **6**, 374-378 (2007).

[4] L.S. Sapochak, A. Padmaperuma, N. Washton et al., "Effects of Systematic Methyl Substitution of Metal (III) Tris(n-Methyl-8-Quinolinolato) Chelates on Material Properties for Optimum Electroluminescence Device Performance," J. Am. Chem. Soc. **123**, 6300-6307 (2001).

[5] R. McNeill, R. Siudak, J.H. Wardlaw et al., "Electronic Conduction in Polymers," Aust. J. Chem. **16**, 1056-1103 (1963).

[6] S. Pramanik, C.-G. Stefanita, S. Patibandla et al., "Observation of extremely long spin relaxation times in an organic nanowire spin valve," Nature Nanotechnology **2**, 216-219 (2007).

[7] Wilhelm Warta and Norbert Karl, "Hot holes in naphthalene: High, electric-field-dependent mobilites," Phys. Rev. B **32** (2), 1172-1182 (1985).

[8] Y. Luo, H. Aziz, Zoran D. Popovic et al., "Degradation mechanisms in organic light-emitting devices: Metal migration model versus unstable tris(8-hydroxyquinoline) aluminum cationic model," J. Appl. Phys. **101**, 034510 (2007).

[9] H-C Yuan, G. Wang, Z. Ma et al., "Flexible thin-film transistors on biaxial- and uniaxial-strained Si and SiGe membranes," Semicond. Sci. Technol. **22**, S72-S75 (2007).

[10] H. Sirringhaus, T. Kawase, R.H. Friend et al., "High-Resolution Inkjet Printing of All-Polymer Transistor Circuits," Science **290**, 2123 (2000).

[11] S.A. Shaheen, C.J. Brabec, N.S. Sariciftci et al., "2.5% efficient organic plastic solar cells," Appl. Phys. Lett. **78** (6), 841-843 (2001).

[12] P Peumans, S. Uchida, and S.R. Forrest, "Efficient bulk heterojunction photovoltaic cells using small-molecular-weight organic thin films," Nature **425**, 158-162 (2003).

[13] 2001.

[14] C. Féry, B. Racine, D. Vaufrey et al., "Physical mechanism responsible for the stretched exponential decay behavior of aging organic light-emitting diodes.," Appl. Phys. Lett. **87**, 213502-213501 (2005).

[15] P.F. Carcia, R.S. McLean, M. Reilly et al., "Ca test of Al203 gas diffusion barriers grown by atomic layer deposition on polymers," Appl. Phys. Lett. **89**, 031915 (2006).

[16] L. Ke, S. Kumar, K. Zhang et al., "Organic light emitting devices performance improvement by inserting thin parylene layer," Synth. Met. **140**, 295-299 (2004).

[17] M.A. Baldo, (2004).

[18] P.W. Anderson, "Absence of Diffusion in Certain Random Lattices," Physical Review **109** (5), 1492-1505 (1958).

[19] P.W. Atkins and R.S. Friedman, *Molecular Quantum Mechanics*, 3rd ed. (Oxford University Press, New York, 1997).

[20] P Peumans, Princeton, 2004.

[21] Neil W. Ashcroft and N. David Mermin, *Solid State Physics*, 1st ed. (Harcourt Brace, Orlando, 1976).

[22] M Segal, M.A. Baldo, R.J. Holmes et al., "Excitonic singlet-triplet ratios in molecular and polymeric organic materials," Phys. Rev. B **68**, 075211 (2003).

[23] N.J. Turro, *Modern Molecular Photochemistry*. (University Science Books, Mill Valley, 1991).

[24] David J. Griffiths, *Introduction to Quantum Mechanics*, Second Edition ed. (Pearson Prentice Hall, Upper Saddle River, NJ, 2005).

[25] D.S. McClure, J. Chem. Phys. **20**, 682 (1952).

[26] Yue Wu, Zhihua Xu, and Bin Hu, "Tuning magnetoresistance and magnetic-field-dependent electroluminescence through mixing a strong-spin-orbital-coupling molecule and a weak-spin-orbital-coupling polymer," Phys. Rev. B **75** (`), 035214 (2007).

[27] V. Dediu, M. Murgia, F.C. Matacotta et al., "Room temperature spin polarized injection in organic semiconductor," Solid State Communications **122**, 181-184 (2002).

[28] M. Wohlgenannt, Kunj Tandon, S. Mazumdar et al., "Formation cross-sections of singlet and triplet excitons in pi-conjugated polymers," Nature **409**, 494-497 (2001).

[29] M. Wohlgenannt, Kunj Tandon, S. Mazumdar et al., "Formation cross-sections of singlet and triplet excitons in pi-conjugated polymers - Supplementary Information," Nature **409**, 494-497 (2001).

[30] Z. Shuai, D. Beljonne, R.J. Silbey et al., "Singlet and Triplet Exciton Formation Rates in Conjugated Polymer Light-Emitting Diodes," Phys. Rev. Lett. **84** (1), 131-134 (2000).

[31] K. Tandon, S. Ramasesha, and S. Mazumdar, "Electron correlation effects in electron-hole recombination in organic light-emitting diodes," Phys. Rev. B **67**, 045109 (2003).

[32] A.P. Monkman, H.D. Burrows, L.J. Hartwell et al., "Triplet Energies of pi-Conjugated Polymers," Phys. Rev. Lett. **86** (7), 1358-1361 (2001).

[33] R.E. Watson, S. Koide, M. Peter et al., "Effective Conduction-Electron-Local-Moment Exchange Interaction in Metals: Rare-Earth Interband Mixing," Physical Review **139** (1A), A167-A178 (1965).

[34] J.B. Goodenough, *Magnetism and the chemical bond.* (Interscience Publishers, New York, 1963).

[35] L. Hviid, W.G. Bouwman, M.N. Paddon-Row et al., "Spin control of the lifetime of an intramolecular charge-transfer excited state," Photochem. Photobiol. Sci. **2**, 995-1001 (2003).

[36] M.A. Baldo, D.F. O'Brien, Y. You et al., "High efficiency phosphorescent emission from organic electroluminescent devices," Nature **395**, 151-154 (1998).

[37] W. Helfrich and W.G. Schneider, "Recombination radiation in anthracene crystals," Phys. Rev. Lett. **14** (7), 229-231 (1965).

[38] P.S. Vincett, W.A. Barlow, R.A. Hann et al., Thin Solid Films **94**, 171 (1982).

[39] C.W. Tang and S.A. VanSlyke, "Organic electroluminescent diodes," Appl. Phys. Lett. **11**, 913-915 (1987).

[40] V.I. Adamovich, S.R. Cordero, P.I. Djurovich et al., "New charge-carrier blocking materials for high efficiency OLEDs," Organic Electronics **4**, 77-87 (2003).

[41] M.A. Baldo, M.E. Thompson, and S.R. Forrest, "High efficiency fluorescent organic light-emitting devices using a phosphorescent sensitizer," Nature **403**, 750-753 (2000).

[42] A. Fischer, S. Chenais, S. Forget et al., "Highly efficient multilary organic pure blue light emitting diodes with substitute carbazoles compounds in the emitting layer," Journal of Applied Physics D: Applied Physics **39**, 917-922 (2006).

[43] C.L. Mulder, K. Celebi, K.M. Milaninia et al., "Saturated and Efficient Blue Phosphorescent Organic Light Emitting Devices with Lambertian Angular Emission," Appl. Phys. Lett. **90**, 211109 (2007).

[44] M. Reufer, M.J. Walter, P.G. Lagoudakis et al., "Spin-conserving carrier recombination in conjugated polymers," Nature Materials **4**, 340-346 (2005).

[45] A. Kadashchuk, A. Vakhnin, I. Blonski et al., "Singlet-Triplet Splitting of Geminate Electron-Hole Pairs in Conjugated Polymers," Phys. Rev. Lett. **93** (6), 066803 (2004).

[46] Carsten Rothe and Andy Monkman, "Regarding the origin of the delayed fluorescence of conjugated polymers," The Journal of Chemical Physics **123**, 224904 (2005).

[47] D. Beljonne, A. Ye, Z. Shuai et al., "Chain-length dependence of singlet and triplet exciton formation rates in organic light-emitting diodes," Advanced Functional Materials **14**, 684-692 (2004).

[48] D. Beljonne, H.F. Wittmann, A. Kohler et al., "Spatial extent of the singlet and triplet excitons in transition metal-containing poly-ynes," J. Chem. Phys. **105** (9), 3868-3877 (1996).

[49] W. Barford, "Theory of singlet exciton yield in light-emitting polymers," Phys. Rev. B **70**, 205204 (2004).

[50] M.A. Baldo, D.F. O'Brien, M.E. Thompson et al., "Excitonic singlet-triplet ratio in a semiconducting organic thin film," Phys. Rev. B **60**, 14422-14428 (1999).

[51] M.A. Baldo and S.R. Forrest, "Transient analysis of organic electrophosphorescence. I. Transient analysis of triplet energy transfer," Phys. Rev. B **62** (16), 10958-10966 (2000).

[52] Y Cao, ID Parker, G Yu et al., "Improved quantum efficiency for electroluminescence in semiconducting polymers," Nature **397**, 414-417 (1999).

[53] Ji-Seon Kim, Peter K. H. Ho, Neil C. Greenham et al., "Electroluminescence emission pattern of organic light-emitting diodes: Implications for device efficiency calculations," J. Appl. Phys. **88** (2), 1073-1081 (2000).

[54] J.S. Wilson, A.S. Dhoot, A.J.A.B. Seeley et al., "Spin-dependent exciton formation in pi-conjugated compounds," Nature **413**, 828-831 (2001).

[55] M. Wohlgenannt and Z. Valy Vardeny, "Photophysics properties of blue-emitting polymers," Synth. Met. **125**, 55-63 (2002).

[56] Chihaya Adachi, Marc A. Baldo, Mark E. Thompson et al., "Nearly 100% internal phosphorescence efficiency in an organic light emitting device," J. Appl. Phys. **90** (10), 5048-5051 (2001).

[57] R.C. Hughes and Z.G. Soos, "Yield of singlet and triplet excitons from x-ray and ruby laser excitation of anthracene single crystals," Chemical Physics **63** (3), 1122-1126 (1975).

[58] M. Iltaf Khan, Guilermo C. Bazan, and Zoran D. Popovic, "Evidence for electric field-assisted dissociation of the excited singlet state into charge carriers in MEH-PPV," Chem. Phys. Lett. **298**, 309-314 (1998).

[59] W. Stampor, J. Kalinowski, P. Di Marco et al., "Electric field effect on luminescence efficiency in 8-hydroxyquinoline aluminum ($Alq_3$) thin films," Appl. Phys. Lett. **70**, 1935-1937 (1997).

[60] N.T. Harrison, G.R. Hayes, R.T. Phillips et al., "Singlet Intrachain Exciton Generation and Decay in Poly(p-phenylenevinylene)," Phys. Rev. Lett. **77** (9), 1881-1884 (1996).

[61] M Segal and M.A. Baldo, "Reverse bias measurements of the photoluminescent efficiency of semiconducting organic thin films," Organic Electronics **4**, 191-197 (2003).

[62] Results were confirmed using material from two suppliers: American Dye Source. 555 Morgan Blvd. Baie D'Urfe, Quebec, Canada H9X 3T6, and H.W. Sands. 1080 E. Indiantown Rd, Suite 206. Jupiter FL 33477. The molecular weights of each polymer were reported to be $10^6$ and 35,000, respectively.

[63] D.Z. Garbuzov, V. Bulovic, P.E. Burrows et al., "Photoluminescence efficiency and absorption of aluminum-tris-quinolate ($Alq_3$) thin films," Chem. Phys. Lett. **249**, 433-437 (1996).

[64] Hedi Mattoussi, Hideyuki Murata, Charles D. Merritt et al., "Photoluminescence quantum yield of pure and mlecularly doped organic solid films," J. Appl. Phys. **86** (5), 2642-2650 (1999).

[65] V. Bulovic, V.B. Khalfin, G. Gu et al., "Weak Microcavity Effects in Organic Light Emitting Devices," Phys. Rev. B **58**, 3730 (1998).

[66] NC Greenham, IDW Samuel, GR Hayes et al., "Measurement of absolute photoluminescence quantum efficiencies in conjugated polymers," Chem. Phys. Lett. **241**, 89-96 (1995).

[67] Paul F. van Hutten, Victor V. Krasnikov, and Georges Hadziioannou, "Polymers for opto-electronic applications: structure and morphology of thin films and their interfaces," Synth. Met. **122**, 83-86 (2001).

[68] I.G. Hill and A. Kahn, "Organic semiconductor heterointerfaces containing bathocuproine," J. Appl. Phys. **86**, 4515-4519 (1999).

[69] P Peumans and SR Forrest, "Very-high-efficiency double-heterostructure copper phthalocyanine/C60 photovoltaic cells," Appl. Phys. Lett. **79** (1), 126-128 (2001).

[70] M.A. Baldo and S.R. Forrest, "Interface-limited injection in amorphous organic semiconductors," Phys. Rev. B **64**, 085201 (2001).

[71] R.R. Chance, A. Prock, and R. Sibley, "Molecular fluorescence and energy transfer near metal interfaces," Adv. Chem. Phys. **37**, 1-65 (1978).

[72] M.A. Baldo, C. Adachi, and S.R. Forrest, "Transient analysis of organic electrophosphorescence. II. Transient analysis of triplet-triplet annihilation," Phys. Rev. B **62** (16), 10967-10977 (2000).

[73] P.E. Burrows, Z. Shen, V. Bulovic et al., "Relationship between electroluminescence and current transport in organic heterojunction light-emitting devices," J. Appl. Phys. **79**, 7991-8006 (1996).

[74] Brian W. D'Andrade, Marc A. Baldo, Chihaya Adachi et al., "High-efficiency yellow double-doped organic light-emitting devices based on phosphor sensitized fluorescence," Appl. Phys. Lett. **79** (7), 1045-1047 (2001).

[75] M.A. Baldo, M.E. Thompson, and S.R. Forrest, "Phosphorescent materials for application to organic light emitting devices," Pure Appl. Chem. **71** (11), 2095-2106 (1999).

[76] M.A. Baldo, R.J. Holmes, and S.R. Forrest, "The prospects for electrically-pumped organic lasers," Phys. Rev. B **66**, 035321 (2002).

[77] Th. Förster, "Transfer mechanisms of electronic excitation," Disc. Faraday Soc. **27**, 7-17 (1959).

[78] L.C. Lin, H.F. Meng, J.T. Shy et al., "Triplet-to-Singlet Exciton Formation in poly(*p*-phenylene-vinylene) Light-Emitting Diodes," Phys. Rev. Lett. **90** (3), 036601 (2003).

[79] A.S. Dhoot, D.S. Ginger, D. Beljonne et al., "Triplet formation and decay in conjugated polymer devices," Chem. Phys. Lett. **360**, 195-201 (2002).

[80] M. Wohlgenannt, X.M. Jiang, Z.V. Vardeny et al., "Conjugation-Length Dependence of Spin-Dependent Exciton Formation Rates in pi-Conjugated Oligomers and Polymers," Phys. Rev. Lett. **88** (19), 197401 (2002).

[81] N.C. Greenham, J. Shinar, J. Partee et al., "Optically detected magnetic resonance study of efficient two-layer conjugated polymer light-emitting devices," Phys. Rev. B **53** (20), 13528-13533 (1996).

[82] L.S. Swanson, J. Shinar, A.R. Brown et al., "Electroluminescence-detected magnetic resonance study of polyparaphenylenevinylene (PPV)-based light emitting diodes," Phys. Rev. B **46** (23), 15072-15077 (1992).

[83] A. Köhler, M. Younus, M.R.A. Al-Mandhary et al., "Donor-acceptor interactions in organometallic and organic poly-ynes," Synth. Met. **101**, 246-247 (1997).

[84] Joanne S. Wilson, Nazia Chawdhury, Muna R.A. Al-Mandhary et al., "The Energy Gap Law for Triplet States in Pt-Containing Conjugated Polymers and Monomers," J. Am. Chem. Soc. **123**, 9412-9417 (2001).

[85] D. Beljonne, Z. Shuai, J. Cornil et al., "On the luminescence efficiency of polymer light-emitting diodes: a quantum-chemical investigation," Journal of Photochemistry and Photobiology A: Chemistry **144**, 57-62 (2001).

[86] R.G. Kepler, J.M. Zeigler, L.A. Harrah et al., "Photocarrier generation and transport in sigma-bonded polysilanes," Phys. Rev. B **35**, 2818-2822 (1987).

[87] G.J. Denton, N. Tessler, N.T. Harrison et al., "Factors Influencing Stimulated Emission from Poly(p-phenylenevinylene)," Phys. Rev. Lett. **78** (4), 733-736 (1997).

[88] Xiwen Chen, Jin-Long Liao, Yongmin Liang et al., "High-Efficiency Red-Light Emission from Polyfluorenes Grafted with Cyclometalated Iridium Complexes and Charge Transport Moiety," J. Am. Chem. Soc. **125**, 636-637 (2003).

[89] A.W. Grice, D.D.C. Bradley, M.T. Bernius et al., "High brightness and efficiency blue light-emitting polymer diodes," Appl. Phys. Lett. **73**, 629-631 (1998).

[90] Masamichi Ikai, Shizuo Tokito, Youichi Sakamoto et al., "Highly efficient phosphorescence from organic light-emitting devices with an exciton-block layer," Appl. Phys. Lett. **79** (2), 156-158 (2001).

[91] R.H. Friend, R.W. Gymer, A.B. Holmes et al., "Electroluminescence in conjugated polymers," Nature **397**, 121-128 (1999).

[92] J. Shinar, in *Handbook of Organic Conductive Molecules and Polymers*, edited by H.S. Nalwa (J. Wiley, NY, 1997), pp. 319-366.

[93] M.K. Lee, M. Segal, Z.G. Soos et al., "On the Yield of Singlet Excitons in Organic Light-Emitting Devices: A Double Modulation Photoluminescence-Detected Magnetic Resonance Study," Phys. Rev. Lett. **94**, 137403 (2005).

[94] V. Dyakonov, G. Zoriniants, M. Scharber et al., "Photoinduced charge carriers in conjugated polymer-fullerence composites studied with light-induced electron-spin resonance," Phys. Rev. B **59** (12), 8019-8025 (1999).

[95] M. Wohlgenannt, C. Yang, and Z. Valy Vardeny, "Spin-dependent delayed luminescence from nongeminate pairs of polarons in pi-conjugated polymers," Phys. Rev. B **66**, 241201 (2002).

[96] M. Wohlgenannt, W. Graupner, G. Leising et al., "Photogeneration and recombination processes of neutral and charged excitations in films of a ladder-type poly(para-phenylene)," Phys. Rev. B **60** (8), 5321-5330 (1999).

[97] D.S. Ginger and N.C. Greenham, "Photoinduced electron transfer from conjugated polymers to CdSe nanocrystals," Phys. Rev. B **59** (16), 10622-10629 (1999).

[98] X. Wei, B.C. Hess, Z.V. Vardeny et al., "Studies of Photoexcited States in Polyacetylene and Poly(paraphenylenevinylene) by Absorption Detected Magnetic Resonance: The Case of Neutral Photoexcitations," Phys. Rev. Lett. **68**, 666-669 (1992).

[99] N.F. Colaneri, D.D.C. Bradley, and R.H. Friend, "Photoexcited states in poly(p-phenylene vinylene): Comparison with trans,trans-distyrylbenzene, a model oligomer," Phys. Rev. B **42** (18), 11670-11681 (1990).

[100] J. Partee, J. Shinar, G. Leising et al., "Long-Lived Polarons and Triplet Excitons in Ladder-Type Poly(p-phenylenes) and Poly(p-phenylene ethynylenes)," Proceedings of SPIE **3145**, 118-131 (1997).

[101] E.L. Frankevich, A.A. Lymarev, I. Sokolik et al., "Polaron-pair generation in poly(phenylene vinylene)," Phys. Rev. B **46** (12), 9320-9324 (1992).

[102] X. Wei, Z.V. Vardeny, N.S. Sariciftci et al., "Absorption-detected magnetic-resonance studies of photoexcitations in conjugated-polymer/C60 composites," Phys. Rev. B **53** (5), 2187-2190 (1996).

[103] E.J.W. List, C.-H. Kim, A.K. Naik et al., "Interaction of singlet excitons with polarons in wide band-gap organic semiconductors: A quantitative study," Phys. Rev. B **64**, 155204 (2001).

[104] W. Graupner, J. Partee, J. Shinar et al., "Dynamics of Long-Lived Polarons in Poly(para-phenylene)-Type Ladder Polymers," Phys. Rev. Lett. **77** (10), 2033-2036 (1996).

[105] E.J.W. List, U. Scherf, K. Mullen et al., "Direct evidence for singlet-triplet exciton annihilation in pi-conjugated polymers," Phys. Rev. B **66**, 235203 (2002).

[106] S. Hayashi, K. Kaneto, and K Yoshino, Sol. St. Comm. **61**, 249-251 (1987).

[107] D.D.C. Bradley and R.H. Friend, J. Phys. Condensed Matter **1**, 3671 (1989).

[108] Z. Valy Vardeny and X. Wei, Mol. Cryst. Liq. Cryst. **256**, 465 (1994).

[109] E.J.W. List, C.-H. Kim, W. Graupner et al., "Nonradiative quenching of singlet excitons by polarons in pi-conjugated polymers," Synth. Met. **119**, 511-514 (2001).

[110] L. Smilowitz and AJ Heeger, "Photoinduced Absorption from Triplet Excitations in poly(2-methoxy,5-(2'-ethyl-hexyloxy)-p-phenylene vinylene) oriented by gel-processing in polyethylene," Synth. Met. **48** (2), 193-202 (1992).

[111] S.-H. Lim, T.G. Bjorklund, and C.J. Bardeen, "The role of long-lived states in the photoluminescence dynamics of poly(phenylene vinylene) conjugated polymers. II. Excited-state quenching versus ground-state depletion," J. Chem. Phys. **118** (9), 4297-4305 (2003).

[112] S.-H. Jin, M.-S. Jang, and H.-S. Suh, "Synthesis and Characterization of Highly Luminescent Asymmetric Poly(p-phenylene vinylene) Derivatives for Light-Emitting Diodes," Chem. Mat. **14** (2), 643-650 (2002).

[113] L. Smilowitz, A. Hays, A.J. Heeger et al., "Picosecond time resolved photoluminescence in MEHPPV - solution film, gel and blend," Synth. Met. **55** (1), 249-254 (1993).

[114] H.D. Burrows, J.S. de Melo, C. Serpa et al., "S1 -> T1 intersystem crossing in pi-conjugated organic polymers," J. Chem. Phys. **115** (20), 9601 (2001).

[115] P.A. Lane, L.S. Swanson, Q.-X. Ni et al., Phys. Rev. Lett. **68**, 887 (1992).

[116] Carlos A. Steren, Hans van Willigen, and Marco Fanciulli, "Photoinduced spin polarization of paramagnetic centers in solid C60," Chem. Phys. Lett. **245**, 244-248 (1995).

[117] P.A. Lane and J. Shinar, Phys. Rev. B. **51**, 10028 (1995).

[118] G. Li, C.-H. Kim, P.A. Lane et al., "Magnetic resonance studies of tris-(8-hydroxyquinoline) aluminum-based organic light-emitting devices," Phys. Rev. B **69** (16), 165311 (2004).

[119] M. Wohlgenannt, "Polarons in pi-conjugated semiconductors: absorption spectroscopy and spin-dependent recombination," Phys. Stat. Sol. A **201** (6), 1188-1204 (2004).

[120] B. van Dijk, P. Gast, and A.J. Hoff, "Control of Radical Pair Lifetime by a Switched Magnetic Field," Physical Review Letters **77** (21), 4478-4481 (1996).

[121] C.G. Yang, E. Eherenfreund, M. Wohlgenannt et al., "Comment on "Frequency response and origin of the spin-1/2 photoluminescence-detected magnetic resonance in a pi-conjugated polymer"," Phys. Rev. B **75**, 246201 (2007).

[122] M. Segal, M.A. Baldo, M.K. Lee et al., "The Frequency Response and Origin of the Spin-1/2 Photoluminescence-Detected Magnetic Resonance in a pi-Conjugated Polymer," Physical Review B **71**, 245201 (2005).

[123] The single modulation data reported in Ref. 1 is inconsistent in the time and frequency domains. The associated theory matches both sets of data because it appears to have been applied inconsistently. Furthermore, if Eq. 2 in Ref. 1 is accurate, quenching and not spin dependent recombination explains the frequency response. This analysis is supported by linearizing Eq. 2, which yields a second order system with an overdamped homogeneous equation. The linearized solution for $n_1$ exhibits a zero below either pole frequency, yielding an overshoot in its transient response. The linearized solution for $n_2$ also exhibits a zero, but it is above the lowest pole frequency. Interestingly, the zeros cancel for $n_1+n_2$, apparently confirming that the sum may have been used to simulate the PLDMR in Fig. 2b. This is unphysical since singlet excitons cannot form from parallel polaron pairs. In contrast, the transient data is fit to some other combination of spin parallel and antiparallel polaron modulations; see the introduction of differing values for $\tau_{R1}$ and $\tau_{R2}$. Thus, the model of Ref. 1 can fit the

transient but it cannot fit the frequency domain data. Equation 2 may also be used to describe the dynamics of triplet-polaron quenching. But the triplet-polaron model depends only on the total population of quenchers. Hence the zeros in $n_1$ and $n_2$ are cancelled and the triplet-polaron model fits the frequency domain data.


[124] M.K. Lee, M. Segal, Z.G. Soos et al., "Yield of Singlet Excitons in Organic Light-Emitting Devices: A Double Modulation Photoluminescence-Detected Magnetic Resonance Study," Physical Review Letters **94**, 137403 (2005).

[125] C.G. Yang, E. Eherenfreund, and Z. Valy Vardeny, "Comment on "Yield of Singlet Excitons in Organic Light-Emitting Devices: A Double Modulation Photoluminescence-Detected Magnetic Resonance Study"," Phys. Rev. Lett. **96**, 089701 (2006).

[126] I. Rudra, Q. Wu, and T. Van Voorhis, "Accurate magnetic exchange couplings in transition-metal complexes from constrained density-functional theory," The Journal of Chemical Physics **124**, 024103 (2006).

[127] Q. Wu and T. Van Voorhis, "Direct optimization method to study constrained systems with density-functional theory," Physical Review A **72** (2), 024502 (2005).

[128] Q. Wu and T. Van Voorhis, "Constrained Density Functional Theory and Its Application in Long-Range Electron Transfer," Journal of Chemical Theory and Computation **2** (3), 765-774 (2006).

[129] R.A. Kendall, E. Aprà, D.E. Bernholdt et al., "High performance computational chemistry: An overview of NWChem a distributed parallel application," Computer Physics Communications **128**, 260-283 (2000).

[130] T.P. Straatsma, E. Aprà, T.L. Windus et al., NWChem (Pacific Northwest National Laboratory, Richland, Washington, 99352-0999, USA, 2004 ).

[131] A.D. Becke, "Density-functional thermochemistry. III. The role of exact exchange," J. Chem. Phys. **98** (7), 5648-5652 (1993).

[132] M. Colle and C. Garditz, "Phosphorescence of aluminum tris(quinoline-8-olate)," Appl. Phys. Lett. **84** (16), 3160-3162 (2004).

[133] T. Tsuboi, H. Murayama, and A. Penzkofer, "Energy transfer in a thin film of TPD fluorescent molecules doped with PtOEP and Ir(ppy)3 phosphorescent molecules," Applied Physics B **81**, 93-99 (2005).

[134] R.J. Holmes, S.R. Forrest, Y.-J. Tung et al., "Blue organic electrophosphorescence using exothermic host-guest energy transfer," Appl. Phys. Lett. **82** (15), 2422-2424 (2003).

[135] V. Bulovic, A. Shoustikov, M.A. Baldo et al., "Bright, saturated, red-to-yellow organic light -emitting devices based on polarization-induced spectral shifts," Chem. Phys. Lett. **287**, 455-460 (1998).

[136] Y. Kawamura, J. Brooks, J.J. Brown et al., "Intermolecular Interaction and a Concentration-Quenching Mechanism of Phosphorescent Ir(III) Complexes in a Solid Film," Phys. Rev. Lett. **96**, 017404 (2006).

[137] W. Barford and E.E. Moore, "An estimate of the inter-system crossing time in light-emitting polymers," arXiv:physics/0410253 (2004).

[138] R. Das, P.J. Kiley, M. Segal et al., "Integration of Photosynthetic Protein Molecular Complexes in Solid-State Electronic Devices," Nano Letters **4** (6), 1079-1083 (2004).

[139] H. Park, A.K.L. Lim, A. Paul Alivisatos et al., "Fabrication of metallic electrodes with nanometer separation by electromigration," Appl. Phys. Lett. **75** (2), 301-303 (1999).

[140] A. Stamouli, J.W.M. Frenken, T.H. Oosterkamp et al., "The electron conduction of photosynthetic protein complexes embedded in a membrane," FEBS Letters **560**, 109-114 (2004).